

Spectroscopy of Candidate Metal-Deficient Galaxies with the 6-m Telescope

A. Yu. Kniazev*, S. A. Pustilnik, A. V. Ugryumov, and T. F. Kniazeva

Special Astrophysical Observatory, Russian Academy of Sciences, Nizhniĭ Arkhyz, Stavropolskiĭ kraĭ, 357147 Russia

Received April 1, 1999; in final form, August 3, 1999

Abstract—We present the first results of our program of search for the most metal-deficient blue compact galaxies (BCGs) carried out with the 6-m Special Astrophysical Observatory telescope. The results of spectrophotometry are presented and discussed for ten galaxies from the Case and Hamburg/SAO surveys. The selection of candidates, observations, and data reduction are described in detail. For all the galaxies studied, we measured the intensity of the [O III] $\lambda 4363$ Å emission line, which allows us to properly determine the temperatures of H II regions and to deduce elemental abundances. We measured the intensities of all the detected emission lines in H II regions of the galaxies under study and determined the abundances of oxygen and neon in them and in some of these galaxies, of other elements (N, S, He, Ar, and Fe). The oxygen abundance $\log(\text{O}/\text{H}) + 12$ in six galaxies was derived with an error ≤ 0.1 dex. Six of the ten galaxies studied turned out to be metal-poor with an oxygen abundance $\leq 1/10$ of its solar value [i.e., $12 + \log(\text{O}/\text{H}) \leq 7.92$]. HS 0837+4717 with $12 + \log(\text{O}/\text{H}) \leq 7.7$ is one of the most metal-poor galaxies in this sample and one of the candidates for young galaxies. Low-contrast, broad emission components of the nebular [O III] $\lambda 4959$ and 5007 Å lines were detected in its spectrum, suggesting high velocities of gas motions in this galaxy. © 2000 MAIK “Nauka/Interperiodica”.

1. INTRODUCTION

Young galaxies near the boundaries of the observable Universe—the faintest and very compact objects—are presently one of the most popular targets for many large telescopes, including HST and 10-m Keck. Unfortunately, their extremely low fluxes and angular sizes require unprecedented efforts to study the formation of galaxies at that distant epoch in sufficient detail.

Fortunately, the galaxy formation apparently has not yet been finished. Although there appears to be few truly young galaxies forming the first generation of stars from primordial pregalactic gas in the local Universe, their study has great advantages, providing insight into the processes taking place during the formation of galaxies. The goal of our program, whose first results are presented here, is to find new objects similar to I Zw 18 and SBS 0335–052, the most likely candidates for young galaxies, and to analyze their basic properties. An analysis of the properties of a sufficiently large sample of young galaxies is of importance both in understanding the ranges of the various parameters affecting the galaxy formation in the early Universe and in comparing predictions of model calculations with actually observed objects.

One of the lines of search for young galaxies is associated with blue compact galaxies (BCGs)—low-mass objects in which very intense star formation (hereafter SF) reaching a rate of $(0.1\text{--}1)M_{\odot} \text{ yr}^{-1}$ is currently taking

place. At a characteristic neutral-gas mass in these galaxies of $\sim 10^8 M_{\odot}$, such a high SF rate cannot be retained on a scale of the order of the age of the Universe. Either we are observing the first, relatively recent SF in the gas cloud formed long ago in these galaxies or SF also took place in them earlier, but with a highly variable rate, and such SF bursts as those observed at present alternated in them with long periods of low SF activity (see, e.g., [1]). An analysis of the colors of extended BCG envelopes on deep images shows that an overwhelming majority of the BCGs studied contain a high percentage of stars with ages of several Gyr; i.e., the BCGs are generally rather old. However, a considerable deficiency of heavy elements relative to the solar value (a factor of 3 to 10, on the average) suggests that the BCGs are appreciably younger than the massive galaxies in evolutionary terms.

The hypothesis that truly young galaxies undergoing the first burst of star formation can be among the BCGs goes back to the study by Searle and Sargent [2]. The first candidate was I Zw 18 (Mrk 116), a galaxy with a record heavy-element deficiency $Z \sim 1/50Z_{\odot}$. However, fairly convincing evidence for its youth has been obtained only in recent years by combining the results of its study in the range from ultraviolet (HST) to radio (VLA) wavelengths [3–5]. Another BCG with a metallicity $Z \sim 1/46Z_{\odot}$, SBS 0335–052, which is currently considered as the most likely young galaxy, was discovered 18 years later [6, 7]. Its studies over the last four years [8–13], on the one hand, give new evidence for its classification as a truly young galaxy and, on the

* E-mail address for contacts: akn@sao.ru

other hand, are the first step in understanding the properties of such objects.

In the search for primordial galaxies, it is important to decide on the observational criteria that such galaxies must satisfy. In most BCGs with $Z \geq 1/10Z_{\odot}$, the colors of the extended low-surface-brightness component suggest the presence of an old low-mass population [14, 15]. On the other hand, the lack of dependence of the C/O ratio on the O abundance for BCGs with $Z < 1/20Z_{\odot}$ and the appearance of such a dependence for large Z apparently attest that only one SF burst occurred in BCGs with $Z < 1/20Z_{\odot}$ [4]. Thus, the first criterion must be a sufficiently low metallicity of the gas in the regions of the current SF burst. Another criterion must be the absence of fairly red outer parts of galaxies, which are associated with the older low-mass stars born in previous SF bursts.

Since only a small fraction of the gas-cloud mass is processed into stars during the first SF burst, such galaxies must be extremely rich in gas. Finally, the neutral gas of the galaxy in which the first SF burst occurs must have the chemical composition of pregalactic matter, and its metallicity can therefore be several orders of magnitudes lower than the solar one (see, e.g., [9]).

The criterion of a sufficiently low metallicity of the gas in an H II region is the fastest and easiest to test. For this reason, the search for primordial galaxies should apparently be conducted among the most metal-deficient BCGs. Apart from the above BCGs with $Z < 1/20Z_{\odot}$, we know only three more northern-sky galaxies, which were found when analyzing large samples in the SBS and Case survey zones [4], and three southern-sky galaxies from the UM and Tololo surveys [16, 17]. Yet another galaxy with an extremely low metallicity was detected as a companion of the galaxy SBS 0335–052, which is embedded with it in a common H I cloud [11, 13, 18].

We participate in the project of producing the largest sample of BCGs in the northern sky, which includes galaxies from the zones of four objective-prism surveys: the Second Byurakan [19, 20], Case [21–23], Hamburg/SAO [24–26], and KISS [27, 28]. Slit spectroscopy with a low signal-to-noise ratio of candidates for emission-line galaxies from these zones is generally enough to produce a sample, i.e., to classify emission-line galaxies and to determine their radial velocities. Based on the same spectra, we can select candidates for BCGs with metallicity $Z < 1/10Z_{\odot}$. Our objective is to find extremely metal-deficient galaxies by using detailed spectrophotometry ($S/N \sim 20\text{--}30$ in continuum) of the BCGs selected from the new samples in an effort to study their group and individual properties as likely candidates for local young galaxies.

In this paper, we present detailed spectrophotometric observations of ten candidates for metal-poor galaxies. The object-selection criteria, observations, and data reduction are described in Sect. 2. Our results are ana-

lyzed and discussed in Sect. 3. Our main conclusions are summarized in Sect. 4.

2. OBSERVATIONS AND DATA REDUCTION

2.1. Object Selection and the Method of Searching for Metal-Deficient Galaxies

Three galaxies (0939+3601 = CG 274, 0943+3500 = CG 285, and 1050+3714 = CG 793) were taken from [23]. The remaining seven BCGs were selected from the Hamburg/SAO survey of emission-line galaxies [25, 26]. We selected candidates for metal-poor galaxies by using their snapshot spectra with a short integration time obtained with the 6-m telescope.

For the prior selection of candidates using snapshot spectra, we visually compare the optical spectra of several known BCGs with extremely low heavy-element abundances and the spectra of the galaxies of interest. The main criterion is the presence of a detectable [O III] $\lambda 4363$ Å line, implying that the H II region has a fairly high temperature. The second criterion is a sufficiently low ratio of the [O III] $\lambda 4959$, 5007 Å and H β intensities, which, at a high [O III] $\lambda 4363$ Å intensity, suggests an oxygen underabundance rather than a low excitation. Unfortunately, the snapshot spectra obtained during fast spectroscopy when producing BCG samples are of a fairly low quality. For this reason, when candidates for the metal poorest galaxies are selected from the newly found BCGs, there is also an appreciable fraction of higher metallicity galaxies. Because of the deficit of observing time, the search program is carried out in two steps. In the first step, we take spectra with an integration time that is enough to roughly separate the galaxies into objects with O/H abundances lower and higher than $1/15(O/H)_{\odot}$ by recording a weak [O III] $\lambda 4363$ Å line in their spectra, from which we can reliably determine the temperature of the H II region and the oxygen abundance. After detecting the BCGs with $O/H \leq 1/15(O/H)_{\odot}$, we perform observations with a longer integration to subsequently measure weak lines of other elements and to determine their abundances. These galaxies are considered as candidates for young galaxies, and we examine other necessary indications for them, such as the presence of an H I cloud that is much more massive than the galaxy stars and the absence of traces of an old stellar population in an extended halo, in subsequent observations.

Basic parameters of the observed galaxies are given in Table 1.

2.2. Observations

The observations were carried out at the prime focus of the 6-m Special Astrophysical Observatory (SAO) telescope between November 12 and 14, 1996, using the UAGS-based long-slit spectrograph [29] with the ISD015A-based CCD detector (530 by 580 pixels with a rectangular $18 \times 24\text{-}\mu\text{m}$ pixel) produced at the SAO.

Table 1. Basic parameters of the observed galaxies

Galaxy	Coordinates (1950.0)		m_{pg}	V_{hel}	M_{pg}^a	Reference ^b	Alternative names
	α	δ					
0837+4717	08 ^h 37 ^m 00 ^s .6	+47° 17′ 49″	18.2	12830	−17.7	2	PC 0837+472
0910+5011	09 10 33.3	+50 11 52	18.3	10452	−17.2	2	
0939+3601	09 39 51.5	+36 01 18	17.0	4430	−16.6	1	CG 274
0943+3500	09 43 12.4	+35 00 36	18.0	6157	−16.3	1	CG 285
1033+4757	10 33 24.7	+47 57 27	18.5	1456	−12.7	2	
1048+4700	10 48 13.5	+47 00 05	17.5	11776	−18.2	2	
1050+3714	10 50 13.4	+37 14 00	18.0	7648	−16.8	1	CG 793
1645+4137	16 45 07.6	+41 37 28	18.3	9679	−17.0	2	
1717+4955	17 17 30.3	+49 55 51	17.7	1070	−12.8	2	
1720+4412	17 20 07.5	+44 12 29	18.0	8506	−17.0	2	

^a The Hubble constant $H_0 = 75 \text{ km s}^{-1} \text{ Mpc}^{-1}$ was used.

^b 1—[25], 2—[26].

We performed the observations with a long ($2'' \times 180''$) slit in the first order of a $325 \text{ lines mm}^{-1}$ grating (below called L, low resolution) and in the first order of a $650 \text{ lines mm}^{-1}$ grating (below called M, medium resolution). This configuration provides a spatial resolution along the slit of $0''.41 \text{ pixel}^{-1}$. In the L-grating observations, the linear dispersion was $5.8 \text{ \AA pixel}^{-1}$ and the corresponding spectral resolution was $\sim 17 \text{ \AA}$ (the FWHM measured using narrow emission lines of the reference spectrum). The spectral range covered in a single exposure was $3950\text{--}7300 \text{ \AA}$. In the M-grating observations, the spectral range $3700\text{--}7050 \text{ \AA}$ was covered at two grating positions: for the blue ($3700\text{--}5450 \text{ \AA}$) and red ($5400\text{--}7050 \text{ \AA}$) parts of the spectrum. The spectral ranges at these grating positions slightly overlapped ($\sim 50 \text{ \AA}$). In the observations with this grating, the linear dispersion was $3.1 \text{ \AA pixel}^{-1}$, and the spectral resolution was $\sim 8 \text{ \AA}$ (FWHM).

In the L-grating observations, the exposure ranged from 10 to 15 min. The L-grating data were used in the reduction to check that the two ranges taken with the M grating were tied correctly. The total observing time with the M grating varied between 10 and 40 min for each range and was broken up into 1–3 exposures with each no greater than 15 min. The seeing during the observations was $1''.0\text{--}1''.5$ FWHM during the first night, $0''.9\text{--}1''.8$ during the second night, and $1''.3\text{--}2''.0$ during the third night. A log of observations is given in Table 2.

On each night, we observed from two to four spectrophotometric standards from [30, 31]. The spectrum of a He–Ne–Ar lamp was measured to calibrate the wavelength scale before and after each program-object exposure.

The galaxy HS 0837+4717 was also observed on October 7, 1996, with the SP-124 spectrograph at the Nasmyth-1 focus of the 6-m telescope [32] and a Photometrix $1K \times 1K$ CCD detector with a $24 \times 24\text{-}\mu\text{m}$ pixel using the NICE data-acquisition system [33]. The observations were performed with a long ($2'' \times 40''$) slit and grating B1 ($600 \text{ lines mm}^{-1}$) in the first order. Only the blue part of the spectrum ($3600\text{--}6000 \text{ \AA}$) was observed with a linear dispersion of $2.4 \text{ \AA pixel}^{-1}$ and a spectral resolution of $\sim 7.6 \text{ \AA}$ (FWHM).

2.3. Data Reduction

We reduced all our data in the standard MIDAS (Munich Image Data Analysis System) system [34].

2.3.1. Initial data reduction and the reduction of 2D spectra. The initial CCD data reduction included a set of standard steps: bias subtraction, image rotation to the correct orientation (the wavelength increases from left to right), extraction of the useful field containing astronomical information, flat fielding, correction for bad pixels (columns), and removal of cosmic-ray hits. The entire initial reduction was performed with the standard CCDRED package. Dawn-sky spectra were used as a flat field. The flat field was normalized by using the algorithm described by Shergin *et al.* [35]: we considered independently each column/row (in the direction perpendicular to dispersion) of a 2D image and constructed a continuum with a sufficiently large averaging window for it.

Cosmic-ray hits were removed by the FILTER/COSMIC command. Hits that were not removed by this command were eliminated by the MODIFY/PIXEL command.

Table 2. Log of observations

Galaxy	Date, 1996	Number of exposures ^a	Total time, min	Position angle, deg
0837+4717	Oct. 7; Nov. 13	1B, 1B	12B, 15B	257
0910+5011	Nov. 14	3B, 2R	40B, 20R	327
0939+3601	Nov. 12	1F, 2B, 2R	10F, 20R, 27B	8
0943+3500	Nov. 13	2B, 2R	25B, 20R	348
1033+4757	Nov. 14	1B	15B	349
1048+4700	Nov. 12	1B	7B	323
1050+3714	Nov. 12, 14	1F, 3B, 2R	15F, 40B, 20R	349
1645+4137	Nov. 14	1B, 1R	15B, 10R	103
1717+4955	Nov. 13	1B	15B	85
1720+4412	Nov. 14	1B	15B	106

^a F—total range, B—“blue” range, and R—“red” range.

The subsequent reduction of 2D spectra was performed by the LONG package: construction of the 2D dispersion curve, linearization of the 2D spectra, construction of the 2D linearized night-sky spectrum and its subtraction from the object’s spectrum, and construction of the spectral response curve. The accuracy of constructing the 2D dispersion curve was typically 0.3 Å for the M grating.

To determine the spectrum location on the 2D image, we used the DEFINE/ZEBRA command of the ECHELLEC package described in [26] before its extraction. The location of the 2D spectrum was fitted by a first- or second-degree polynomial. The fitting accuracy was no worse than 0.5 pixel and depended on the signal level in continuum. After determining the location of the 2D spectrum, we eliminated its tilt by using the EXTRACT/ORDER code. After applying this procedure, the central row of the 2D image coincided with the centroid of the continuum distribution in the 2D spectrum. This “straightening” procedure allows us, on the one hand, to get rid of the tilt of the linearized 2D spectrum caused by various factors (atmospheric dispersion, peculiar optics of the spectrograph) and, on the other hand, to remove the object’s displacement along the slit, which was done virtually before each repeated exposure to eliminate the effect of bad columns/pixels. If two or more spectra obtained with the same grating angle were available for the object, the “straightened” linearized 2D images were added before extracting a 1D spectrum either by the COMBINE/CCD command of the CCDRED package (if three or more spectra were available) or by the AVERAGE/IMAGE command (if only two spectra were available).

The AVERAGE/COLUMN command was used to determine the extraction boundary of the 1D spectrum for the region with [O III] $\lambda 4363$ Å. Thereafter, the 1D spectrum was extracted by the AVERAGE/ROW

command with the same boundaries for the blue, red, and total spectral ranges.

2.3.2. Determining emission-line intensities and computing elemental abundances. We determined the relative intensities of emission lines, their equivalent widths, and their measurement errors by means of the FIT package and our batch files. The continuum in the spectra was placed automatically by using the code described by Shergin *et al.* [35]; in particularly difficult cases, it was placed manually by the NORMALIZE/SPECTRUM command of the SPEC package. We determined the line centers by fitting the lines with Gaussians (FIT/IMAGE command) and their intensities and equivalent widths by using the INTEGRATE/LINE command. The intensities of close lines ([Ne III] $\lambda 3869$ and H δ + He I $\lambda 3889$, H γ $\lambda 4340$ and [O III] $\lambda 4363$; [O I] $\lambda 6300$ and [S III] $\lambda 6312$; [N II] $\lambda 6548$, $\lambda 6583$, and H α $\lambda 6563$; [S II] $\lambda 6716$ and [S II] $\lambda 6731$) were determined by their Gaussian decomposition using a nonlinear corrected Gauss–Newton method. The He I $\lambda 7065$ and [Ar III] $\lambda 7136$ intensities were taken from the L-grating spectra and recalculated to the relative intensity of the lines measured in the M-grating spectra.

The measured emission-line intensities were corrected for the reddening caused by internal absorption in the galaxy under study and in the interstellar medium of our Galaxy. For the Balmer lines, we also took into account the possible effect of the corresponding stellar absorption features in the underlying continuum. To correct the hydrogen-line intensities, we used an iterative procedure of simultaneously determining the extinction coefficient $C(H\beta)$ and the equivalent widths of absorption lines by the method detailed in [37].

The elemental abundances were computed by means of the scheme described by Izotov *et al.* [37, 38] and Izotov and Thuan [4]. This scheme uses the model of a two-zone H II region from [39]: a high-excitation zone of temperature $T_e(\text{OIII})$ and a low-excitation zone of temperature $T_e(\text{OII})$. The temperature $T_e(\text{OIII})$ is derived from the [O III] $\lambda 4363/(\lambda 4959 + \lambda 5007)$ ratio using a five-level model for O²⁺. This temperature is used to determine the abundances of He⁺, He²⁺, O²⁺, Ne²⁺, and Ar³⁺. The relation between $T_e(\text{OII})$ and $T_e(\text{OIII})$ from [37], which is based on the dependence constructed from Stasinska’s models [39], is used to determine $T_e(\text{O II})$. The O⁺ and N⁺ abundances are derived using $T_e(\text{O II})$. An intermediate temperature between $T_e(\text{OIII})$ and $T_e(\text{OII})$ is used to determine the Ar²⁺ and S²⁺ abundances, following the recommendations of Garnett [40]. The electron density $N_e(\text{SII})$ is derived from the [S II] $\lambda 6717/\lambda 6731$ intensity ratio, as inferred by Aller [41].

The total elemental abundances are deduced after their correction for unobservable ionization stages, as detailed in [37, 38].

The errors in emission-line intensities were determined as a quadratic sum of the error in continuum placement (computed from continuum noise near the

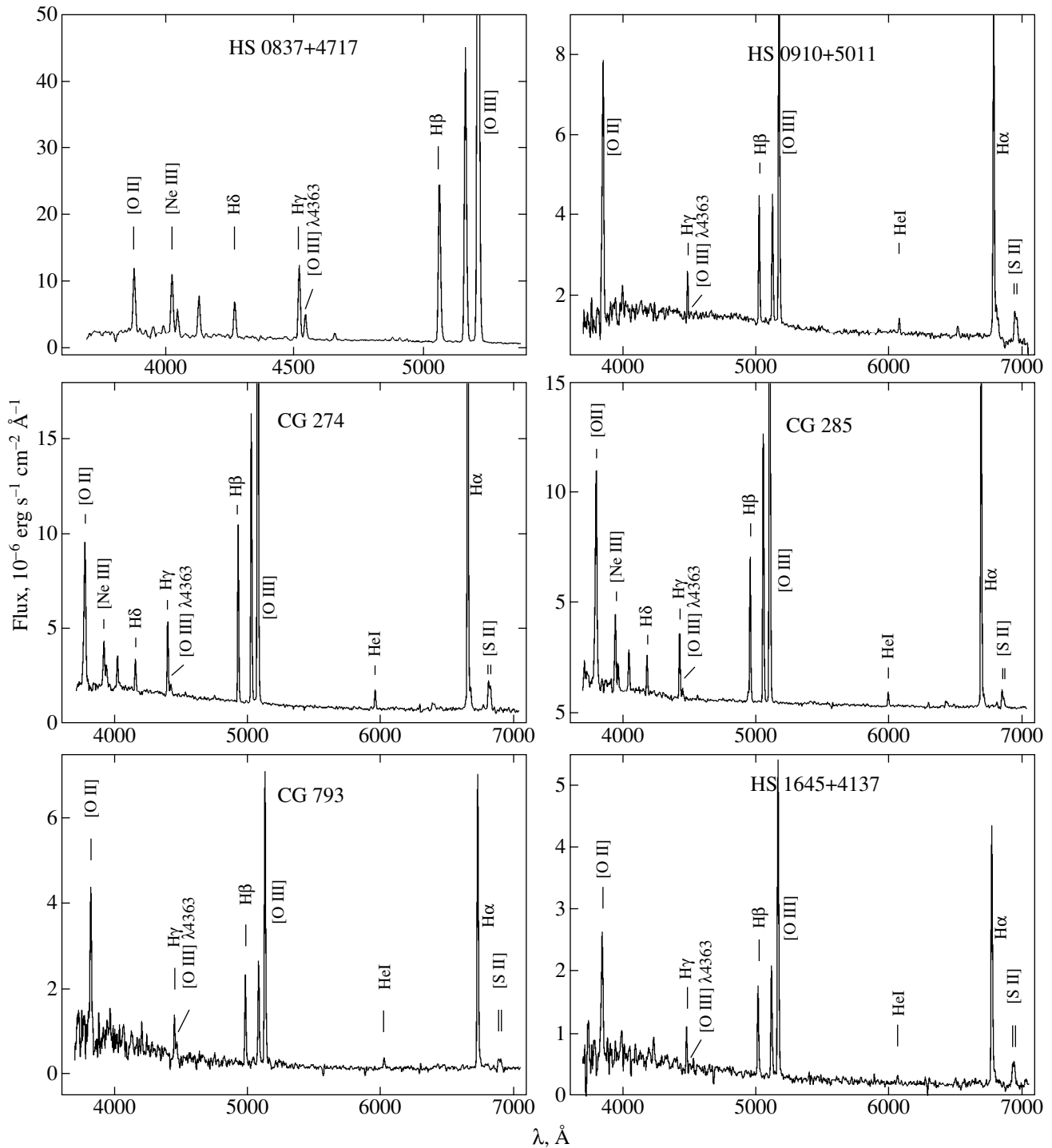


Fig. 1. The spectra of six blue compact galaxies obtained with the 6-m telescope.

measured line) and the Poisson error in the total line flux. When determining the extinction coefficient $C(H\beta)$ and the equivalent widths of absorption lines, we also computed their errors as the fitting errors. When computing the elemental abundances, we took into account all the errors described above.

The spectra of several galaxies under study are shown in Fig. 1. Tables 3–7 give the following data:

observed and corrected emission-line intensities (relative to the $H\beta$ intensity), extinction coefficient $C(H\beta)$, equivalent widths $EW(\text{abs})$ of stellar hydrogen absorption lines, uncorrected $H\beta$ fluxes $F(H\beta)$, $H\beta$ equivalent widths $EW(H\beta)$, and measured redshifts z .

Table 8 gives the electron temperature T_e for the [O III] zone, the electron density N_e calculated from the [S II] doublet line intensity ratio, as well as the ion and

Table 3. Emission-line intensities for the galaxies 0837+4717 and 0910+5011

Species	Galaxy			
	0837+4717		0910+5011	
	$F(\lambda)/F(H\beta)$	$I(\lambda)/I(H\beta)$	$F(\lambda)/F(H\beta)$	$I(\lambda)/I(H\beta)$
3727 [O II]	0.495 ± 0.036	0.632 ± 0.047	2.868 ± 0.108	2.533 ± 0.111
3798 H 10	0.094 ± 0.013	0.118 ± 0.022
3868 [Ne III]	0.424 ± 0.027	0.523 ± 0.034	0.217 ± 0.045	0.192 ± 0.045
3889 H8+He I	0.183 ± 0.023	0.225 ± 0.032
3968 H7+[Ne III]	0.278 ± 0.012	0.336 ± 0.020
4076 [S II]	0.015 ± 0.003	0.018 ± 0.004
4101 H δ	0.237 ± 0.012	0.277 ± 0.019
4340 H γ	0.424 ± 0.013	0.471 ± 0.018	0.324 ± 0.020	0.412 ± 0.035
4363 [O III]	0.153 ± 0.010	0.168 ± 0.011	0.039 ± 0.015	0.035 ± 0.015
4471 He I	0.039 ± 0.003	0.042 ± 0.003
4658 [Fe III]	0.007 ± 0.002	0.007 ± 0.002
4686 He II	0.021 ± 0.002	0.021 ± 0.002
4713 [Ar IV]+He I	0.016 ± 0.002	0.017 ± 0.002
4740 [Ar IV]	0.009 ± 0.002	0.010 ± 0.002
4861 H β	1.000 ± 0.027	1.000 ± 0.028	1.000 ± 0.027	1.000 ± 0.035
4922 He I	0.004 ± 0.002	0.004 ± 0.002	0.025 ± 0.009	0.022 ± 0.009
4959 [O III]	1.859 ± 0.041	1.827 ± 0.040	1.129 ± 0.034	0.997 ± 0.034
5007 [O III]	5.820 ± 0.120	5.670 ± 0.117	3.303 ± 0.083	2.918 ± 0.083
5876 He I	0.116 ± 0.014	0.103 ± 0.014
6300 [O I]	0.112 ± 0.018	0.099 ± 0.018
6312 [S III]	0.018 ± 0.018	0.016 ± 0.018
6548 [N II]	0.101 ± 0.012	0.089 ± 0.012
6563 H α	3.113 ± 0.072	2.833 ± 0.081
6584 [N II]	0.311 ± 0.032	0.274 ± 0.032
6717 [S II]	0.335 ± 0.029	0.296 ± 0.030
6731 [S II]	0.267 ± 0.026	0.236 ± 0.026
C(H β)	0.34 ± 0.03		0.000 ± 0.03	
$F(H\beta)$, 10^{-16} erg s $^{-1}$ cm $^{-2}$ \AA^{-1}		252.8		33.2
EW(H β), \AA		225 ± 4.2		24.6 ± 0.5
EW(abs), \AA		0.00 ± 1.79		3.25 ± 0.41
z		0.04242 ± 0.00015		0.03408 ± 0.00025

elemental abundances. The helium abundance is given only for the objects that exhibited the HeI $\lambda 7065$ \AA line, which is required to obtain a self-consistent solution [37, 38].

3. ANALYSIS AND DISCUSSION OF THE DATA

3.1. Morphology and Peculiarities of the Spectra for Individual Galaxies

All of the galaxies under study are undergoing a strong current SF burst, which has changed considerably their observed characteristics, such as M_B and color.

Below, we give brief morphological descriptions of the galaxies using DSS-2 maps (STScI, Baltimore,

USA; http://archive.stsci.edu/cgi-bin/dss_form). These images are compared with the galaxy pattern seen in the 2D spectrum. Next, in the descriptions of individual objects, by the maximum size we mean the size at the level closest to the background level in the DSS image. For each galaxy, we compare the profile along the slit of the strongest emission line in the spectrum (H α or [O III] $\lambda 5007$ \AA) with the profile along the slit of a star (spectrophotometric standard) or a pair of such stars before and after the object's exposure at the same wavelength. The star profile along the slit (the flux distribution summed over a range $\Delta\lambda$) at wavelength λ is essentially the point spread function (PSF) for this λ of the entire system "atmosphere + telescope + spectrograph". In the case of a statistically significant difference

Table 4. Emission-line intensities for the galaxies 0939+3601 and 0943+3500

Species	Galaxy			
	0939+3601		0943+3500	
	$F(\lambda)/F(\text{H}\beta)$	$I(\lambda)/I(\text{H}\beta)$	$F(\lambda)/F(\text{H}\beta)$	$I(\lambda)/I(\text{H}\beta)$
3727 [O II]	1.330 ± 0.042	1.649 ± 0.054	2.352 ± 0.075	2.412 ± 0.080
3868 [Ne III]	0.403 ± 0.020	0.485 ± 0.024	0.647 ± 0.027	0.661 ± 0.028
3889 H8+He I	0.193 ± 0.017	0.234 ± 0.027	0.226 ± 0.021	0.236 ± 0.032
3968 H7+[Ne III]	0.247 ± 0.019	0.294 ± 0.028	0.348 ± 0.016	0.360 ± 0.028
4026 He I	0.029 ± 0.006	0.034 ± 0.007
4076 [S II]	0.009 ± 0.003	0.011 ± 0.003
4101 Hδ	0.224 ± 0.014	0.259 ± 0.022	0.284 ± 0.019	0.293 ± 0.027
4340 Hγ	0.456 ± 0.011	0.501 ± 0.018	0.457 ± 0.012	0.465 ± 0.020
4363 [O III]	0.096 ± 0.010	0.104 ± 0.011	0.064 ± 0.009	0.065 ± 0.010
4471 He I	0.027 ± 0.005	0.028 ± 0.005	0.025 ± 0.005	0.025 ± 0.005
4658 [Fe III]	0.014 ± 0.004	0.014 ± 0.004
4686 He II	0.024 ± 0.005	0.025 ± 0.005
4713 [Ar IV]+He I	0.007 ± 0.004	0.007 ± 0.004
4740 [Ar IV]	0.013 ± 0.005	0.013 ± 0.005
4861 Hβ	1.000 ± 0.023	1.000 ± 0.025	1.000 ± 0.024	1.000 ± 0.027
4922 He I	0.013 ± 0.005	0.013 ± 0.005
4959 [O III]	1.717 ± 0.046	1.687 ± 0.046	1.842 ± 0.046	1.832 ± 0.046
5007 [O III]	5.188 ± 0.122	5.059 ± 0.120	5.544 ± 0.137	5.510 ± 0.137
5876 He I	0.120 ± 0.006	0.103 ± 0.005	0.104 ± 0.007	0.102 ± 0.007
6300 [O I]	0.044 ± 0.007	0.036 ± 0.006	0.033 ± 0.005	0.032 ± 0.005
6312 [S III]	0.035 ± 0.007	0.028 ± 0.006	0.027 ± 0.005	0.026 ± 0.005
6548 [N II]	0.051 ± 0.004	0.040 ± 0.003	0.027 ± 0.004	0.026 ± 0.004
6563 Hα	3.543 ± 0.069	2.803 ± 0.060	2.933 ± 0.061	2.837 ± 0.065
6584 [N II]	0.157 ± 0.029	0.124 ± 0.023	0.085 ± 0.027	0.082 ± 0.027
6678 He I	0.037 ± 0.005	0.029 ± 0.004	0.038 ± 0.007	0.037 ± 0.007
6717 [S II]	0.217 ± 0.011	0.169 ± 0.008	0.129 ± 0.008	0.125 ± 0.008
6731 [S II]	0.179 ± 0.010	0.139 ± 0.008	0.071 ± 0.007	0.069 ± 0.007
7065 He I	0.010 ± 0.003	0.007 ± 0.002
7136 [Ar III]	0.078 ± 0.011	0.058 ± 0.008
$C(\text{H}\beta)$	0.31 ± 0.03		0.04 ± 0.03	
$F(\text{H}\beta), 10^{-16} \text{ erg s}^{-1} \text{ cm}^{-2} \text{ \AA}^{-1}$	91.8		67.7	
$\text{EW}(\text{H}\beta), \text{ \AA}$	77.6 ± 1.3		127.7 ± 2.2	
$\text{EW}(\text{abs}), \text{ \AA}$	0.10 ± 0.70		0.40 ± 1.54	
z	0.01476 ± 0.00020		0.02007 ± 0.00018	

between the effective width of this emission-line profile FWHM_{obs} and FWHM_{psf} for the PSF, the effective size of a giant H II region (Stroemgren zone) was estimated as $\text{FWHM} = \sqrt{\text{FWHM}_{\text{obs}}^2 - \text{FWHM}_{\text{psf}}^2}$. All profiles were also checked for the presence of a more complex structure by a Gauss analysis with the model profile FWHM_{psf} . If there was a statistically significant structure, we estimated the parameters of each component and their relative positions. These measurements are presented in Table 9 together with measured heliocentric velocities V_{hel} , distances, and scales.

HS 0837+4717. Slightly elongated in the NE–SW direction. Its maximum size in the DSS–2 image is $12'' \times 8''$. The position angle of the major axis is $\text{PA} = 18^\circ$. The underlying galaxy is virtually invisible. The slit was perpendicular to the major axis.

A broad component is clearly seen in the strong [O III] $\lambda 4959$ and 5007 \AA emission lines at low intensities in this galaxy, the only one of all those observed in our program. This component was also previously observed in galaxies of this type [42, 43] and most likely suggests the combined effect of a large number of supernovae and/or young hot stars on the interstellar

Table 5. Emission-line intensities for the galaxies 1033+4757 and 1048+4700

Species	Galaxy			
	1033+4757		1048+4700	
	$F(\lambda)/F(H\beta)$	$I(\lambda)/I(H\beta)$	$F(\lambda)/F(H\beta)$	$I(\lambda)/I(H\beta)$
3727 [O II]	1.747 ± 0.097	1.622 ± 0.109	1.767 ± 0.077	1.984 ± 0.100
3868 [Ne III]	0.524 ± 0.073	0.481 ± 0.078	0.154 ± 0.027	0.169 ± 0.032
3889 H8+He I	0.312 ± 0.066	0.486 ± 0.136
4101 H δ	0.183 ± 0.025	0.260 ± 0.058
4340 H γ	0.350 ± 0.030	0.483 ± 0.062	0.368 ± 0.028	0.462 ± 0.048
4363 [O III]	0.097 ± 0.026	0.087 ± 0.027	0.015 ± 0.004	0.016 ± 0.006
4861 H β	1.000 ± 0.042	1.000 ± 0.057	1.000 ± 0.038	1.000 ± 0.043
4959 [O III]	1.467 ± 0.059	1.261 ± 0.059	1.550 ± 0.050	1.488 ± 0.049
5007 [O III]	4.469 ± 0.148	3.834 ± 0.148	4.619 ± 0.137	4.353 ± 0.131
C(H β)	0.10 ± 0.05		0.25 ± 0.39	
$F(H\beta)$, 10^{-16} erg s $^{-1}$ cm $^{-2}$ \AA^{-1}	31.0		61.6	
EW(H β), \AA	38.3 ± 1.1		64.0 ± 2.2	
EW(abs), \AA	6.00 ± 1.10		3.90 ± 1.63	
z	0.00549 ± 0.00020		0.03925 ± 0.00014	

Table 6. Emission-line intensities for the galaxies 1717+4955 and 1720+4412

Species	Galaxy			
	1717+4955		1720+4412	
	$F(\lambda)/F(H\beta)$	$I(\lambda)/I(H\beta)$	$F(\lambda)/F(H\beta)$	$I(\lambda)/I(H\beta)$
3727 [O II]	1.106 ± 0.072	1.106 ± 0.073	0.909 ± 0.067	1.305 ± 0.112
3868 [Ne III]	0.695 ± 0.041	0.695 ± 0.041	0.327 ± 0.038	0.438 ± 0.059
3889 H8+He I	0.262 ± 0.036	0.262 ± 0.039	0.194 ± 0.036	0.401 ± 0.093
3968 H7+[Ne III]	0.458 ± 0.029	0.458 ± 0.032
4101 H δ	0.297 ± 0.019	0.297 ± 0.023	0.084 ± 0.015	0.257 ± 0.066
4340 H γ	0.503 ± 0.014	0.503 ± 0.019	0.289 ± 0.020	0.468 ± 0.046
4363 [O III]	0.132 ± 0.017	0.132 ± 0.017	0.056 ± 0.016	0.060 ± 0.020
4471 He I	0.027 ± 0.010	0.027 ± 0.010
4686 He II	0.018 ± 0.006	0.018 ± 0.006
4713 [Ar IV]+He I	0.008 ± 0.005	0.008 ± 0.005
4861 H β	1.000 ± 0.013	1.000 ± 0.016	1.000 ± 0.028	1.000 ± 0.037
4922 He I	0.024 ± 0.010	0.020 ± 0.010
4959 [O III]	2.114 ± 0.024	2.114 ± 0.024	1.399 ± 0.040	1.178 ± 0.039
5007 [O III]	6.207 ± 0.070	6.207 ± 0.070	4.316 ± 0.108	3.571 ± 0.104
C(H β)	0.00 ± 0.02		0.70 ± 0.04	
$F(H\beta)$, 10^{-16} erg s $^{-1}$ cm $^{-2}$ \AA^{-1}	92.4		61.6	
EW(H β), \AA	154.8 ± 1.5		34.9 ± 0.7	
EW(abs), \AA	0.00 ± 1.34		5.05 ± 0.64	
z	0.00347 ± 0.00006		0.02775 ± 0.00006	

medium [28]. By decomposing the spectrum near H β and [O III] λ 4949, 5007 \AA (given the weak additional components attributable to the manifestation of inefficient charge transfer when reading out the CCD detector, especially noticeable for bright narrow features) into seven Gaussians, we can clearly identify broad

components in the [O III] lines. Their total contribution to the flux is $\sim 2\%$ of the flux in the narrow components, which is in good agreement with the data of other authors [19, 44], and is confirmed by our further spectroscopic observations of this galaxy [45]. The widths of these broad components (FWHM = 40 \AA) correspond

Table 7. Emission-line intensities for the galaxies 1050+3714 and 1645+4137

Species	Galaxy			
	1050+3714		1645+4137	
	$F(\lambda)/F(H\beta)$	$I(\lambda)/I(H\beta)$	$F(\lambda)/F(H\beta)$	$I(\lambda)/I(H\beta)$
3727 [O II]	2.556 ± 0.188	3.209 ± 0.242	1.893 ± 0.123	1.814 ± 0.129
3868 [Ne III]	0.275 ± 0.040	0.334 ± 0.050	0.358 ± 0.052	0.342 ± 0.053
4101 H δ	0.294 ± 0.063	0.346 ± 0.103	0.296 ± 0.054	0.380 ± 0.092
4340 H γ	0.427 ± 0.044	0.475 ± 0.071	0.354 ± 0.036	0.413 ± 0.061
4363 [O III]	0.103 ± 0.019	0.113 ± 0.020	0.051 ± 0.028	0.049 ± 0.028
4471 He I	0.027 ± 0.008	0.029 ± 0.009
4686 He II	0.062 ± 0.021	0.058 ± 0.021
4861 H β	1.000 ± 0.045	1.000 ± 0.055	1.000 ± 0.050	1.000 ± 0.061
4922 He I	0.069 ± 0.022	0.068 ± 0.022	0.039 ± 0.023	0.037 ± 0.023
4959 [O III]	1.359 ± 0.055	1.332 ± 0.055	1.350 ± 0.064	1.269 ± 0.064
5007 [O III]	4.076 ± 0.140	3.963 ± 0.137	3.858 ± 0.154	3.625 ± 0.153
5876 He I	0.125 ± 0.017	0.106 ± 0.014	0.084 ± 0.025	0.078 ± 0.024
6300 [O I]	0.042 ± 0.015	0.034 ± 0.012	0.081 ± 0.032	0.075 ± 0.032
6312 [S III]	0.038 ± 0.015	0.031 ± 0.012	0.011 ± 0.024	0.010 ± 0.024
6548 [N II]	0.044 ± 0.010	0.034 ± 0.008	0.051 ± 0.022	0.047 ± 0.021
6563 H α	3.563 ± 0.118	2.772 ± 0.101	3.022 ± 0.116	2.828 ± 0.127
6584 [N II]	0.135 ± 0.025	0.105 ± 0.020	0.161 ± 0.039	0.149 ± 0.038
6678 He I	0.032 ± 0.047	0.024 ± 0.037	0.022 ± 0.016	0.021 ± 0.016
6717 [S II]	0.142 ± 0.020	0.109 ± 0.016	0.259 ± 0.042	0.239 ± 0.042
6731 [S II]	0.129 ± 0.020	0.098 ± 0.016	0.276 ± 0.044	0.255 ± 0.043
7065 He I	0.032 ± 0.001	0.024 ± 0.001
C(H β)	0.33 ± 0.04		0.03 ± 0.05	
$F(H\beta)$, 10^{-16} erg s $^{-1}$ cm $^{-2}$ \AA^{-1}	23.1		17.1	
EW(H β), \AA	88.7 ± 2.8		50.5 ± 1.8	
EW(abs), \AA	0.25 ± 2.68		3.15 ± 1.54	
z	0.02558 ± 0.00020		0.03234 ± 0.00007	

to characteristic gas velocities of ~ 2500 km s $^{-1}$. At present, this appears to be the most metal-deficient galaxy in which low-contrast broad components of the strong [O III] ($\lambda 4959$, 5007 \AA) emission lines were detected.

HS 0910+5011. An ellipsoidal galaxy. Its body is elongated in the NW–SE direction. Its maximum size in the DSS–2 image is $13'' \times 8''$. There is a central bright region with the effective size $\text{FWHM} = 5''.5 \times 3''.5$ with its major axis oriented at $\text{PA} = 26^\circ$. There is probably a weak “tail” elongated southward. The slit was perpendicular to the galaxy’s major axis.

0939+3601=CG 274. A star-like galaxy with a very weak underlying emission and a small tail from the SW edge. Its maximum size in the DSS image is $19'' \times 13''$. The central bright part is virtually indistinguishable from the star, its effective size is $\text{FWHM} = 3''.2 \times 2''.8$, and the position angle of its major axis is $\text{PA} = 115^\circ$. The slit was directed NS.

0943+3500=CG 285. The effective size of the galaxy’s central bright zone in DSS–2 is $\text{FWHM} = 5''.5 \times 3''.7$ with its major axis oriented at $\text{PA} = 125^\circ$. The galaxy’s maximum size is $25'' \times 14''$, with possibly irregular outer isophotes.

The slit passed through the central bright region close to the direction of the major axis. The 2D spectrum reveals a peripheral H II region at $\approx 7''$ from the center approximately northward, which is not seen in the DSS image. As we see from the 2D spectrum, this region shows up only in the strongest emission lines, consistent with its absence in DSS.

Decomposition of the intensity profile in the 5007 \AA and H α lines into Gaussians shows that the main (in energy) component ($\approx 80\%$ of the total flux 1.2×10^{-14} erg cm $^{-2}$ s $^{-1}$) of H α is observed from a region of size $\text{FWHM}_{\text{obs}} = 4.8$ pixels. Given the PSF, we can estimate the effective size of the bright emission in these lines, $\text{FWHM} = 3.35 \pm 0.3$ pixels, or $1''.34 \pm 0''.13$, or 0.53 kpc. The peripheral H II region $7''$ northward has

Table 8. Ion and elemental abundances in the observed galaxies

Species	Galaxy				
	0837+4717	0910+5011	0939+3601	0943+3500	1050+3714
$T_e(\text{O III}), \text{K}$	18.667	12.273	15.440	12.267	18.131
$N_e(\text{S II}), \text{cm}^{-3}$	≤ 100	170	235	≤ 10	409
$\text{O}/\text{H}, 10^{-4}$	0.42 ± 0.03	0.97 ± 0.32	0.71 ± 0.07	1.42 ± 0.18	0.56 ± 0.01
$12 + \log(\text{O}/\text{H})$	7.63 ± 0.04	7.99 ± 0.14	7.85 ± 0.04	8.15 ± 0.06	7.75 ± 0.08
He/H	0.083 ± 0.004	...	0.081 ± 0.010
Y	0.249 ± 0.012	...	0.244 ± 0.031
$\text{N}/\text{H}, 10^{-6}$...	6.96 ± 5.39	4.15 ± 1.08	3.24 ± 1.20	1.53 ± 0.69
$12 + \log(\text{N}/\text{H})$...	6.84 ± 0.34	6.62 ± 0.11	6.51 ± 0.16	6.18 ± 0.20
$\text{Ne}/\text{H}, 10^{-5}$	0.81 ± 0.11	1.56 ± 0.98	1.51 ± 0.25	4.21 ± 0.90	0.99 ± 0.33
$12 + \log(\text{Ne}/\text{H})$	6.91 ± 0.06	7.19 ± 0.27	7.18 ± 0.07	7.62 ± 0.09	7.00 ± 0.15
$\text{S}/\text{H}, 10^{-6}$...	2.90 ± 2.14	2.80 ± 0.45	3.95 ± 0.71	1.61 ± 0.57
$12 + \log(\text{S}/\text{H})$...	6.46 ± 0.32	6.45 ± 0.07	6.60 ± 0.08	6.21 ± 0.15
$\text{Ar}/\text{H}, 10^{-6}$	0.16 ± 0.03	...	0.38 ± 0.04	1.09 ± 0.31	...
$12 + \log(\text{Ar}/\text{H})$	5.21 ± 0.07	...	5.58 ± 0.05	6.04 ± 0.09	...
$\text{Fe}/\text{H}, 10^{-6}$	1.27 ± 0.12	1.95 ± 0.31	...
$12 + \log(\text{Fe}/\text{H})$	6.10 ± 0.04	6.29 ± 0.07	...
$\log(\text{N}/\text{O})$...	-1.14 ± 0.37	-1.24 ± 0.12	-1.64 ± 0.17	-1.57 ± 0.21
$\log(\text{Ne}/\text{O})$	-0.72 ± 0.07	-0.79 ± 0.31	-0.67 ± 0.08	-0.53 ± 0.11	-0.76 ± 0.17
$\log(\text{S}/\text{O})$...	-1.52 ± 0.35	-1.41 ± 0.08	-1.56 ± 0.10	-1.54 ± 0.17
$\log(\text{Ar}/\text{O})$	-2.42 ± 0.08	...	-2.28 ± 0.07	-2.12 ± 0.11	...
$[\text{O}/\text{Fe}]$	0.10 ± 0.05	0.44 ± 0.09	...
	1033+4757	1048+4700	1645+4137	1717+4955	1720+4412
$T_e(\text{O III}), \text{K}$	16.371	8.433	12.820	15.627	14.119
$N_e(\text{S II}), \text{cm}^{-3}$	≤ 100	≤ 100	780	≤ 100	≤ 100
$\text{O}/\text{H}, 10^{-4}$	0.49 ± 0.14	3.82 ± 0.90	0.98 ± 0.43	0.73 ± 0.10	0.62 ± 0.19
$12 + \log(\text{O}/\text{H})$	7.69 ± 0.12	8.58 ± 0.11	7.99 ± 0.19	7.86 ± 0.06	7.79 ± 0.13
$\text{N}/\text{H}, 10^{-6}$	5.18 ± 5.54
$12 + \log(\text{N}/\text{H})$	6.71 ± 0.47
$\text{Ne}/\text{H}, 10^{-5}$	1.37 ± 0.70	4.50 ± 2.07	2.20 ± 2.48	1.79 ± 0.38	1.74 ± 0.90
$12 + \log(\text{Ne}/\text{H})$	7.14 ± 0.22	7.65 ± 0.20	7.34 ± 0.35	7.25 ± 0.09	7.24 ± 0.22
$\text{S}/\text{H}, 10^{-6}$	2.13 ± 2.48
$12 + \log(\text{S}/\text{H})$	6.33 ± 0.51
$\log(\text{N}/\text{O})$	-1.28 ± 0.50
$\log(\text{Ne}/\text{O})$	-0.55 ± 0.25	-0.93 ± 0.23	-0.65 ± 0.40	-0.61 ± 0.11	-0.55 ± 0.26
$\log(\text{S}/\text{O})$	-1.66 ± 0.54

approximately the same size (0.6 kpc), and its $\text{H}\alpha$ flux accounts for $\approx 5\%$ of the total flux. In addition, the extended component centered on the brightest component with FWHM = 10.7 pixels, or 1.6 kpc, gives $\approx 10\%$ of the total $\text{H}\alpha$ flux. There is another extended component with FWHM = 9.5 pixels, or 1.3 kpc, in the $\text{H}\alpha$ intensity profile. It is shifted from the brightest component southward by approximately 10 pixels (or 1.4 kpc) and accounts for $\approx 4\%$ of the total $\text{H}\alpha$ flux. In the 2D spectrum, this component corresponds to the region below the central bright emission, in which the

continuum is also clearly seen. Given the cometary morphology in the DSS image, we can assume that we observe a wave of star formation in this galaxy similar to that described by Izotov *et al.* [46] for the galaxy CG 389.

HS 1033+4757. The central bright region elongated in the NW–SE direction has FWHM = $5''.1 \times 5''.0$ in DSS–2 with its major axis oriented at PA = 64° . The galaxy’s maximum size is $18'' \times 12''$.

The slit passed in the SN direction through the central bright region. Emission is observed from a star-like region, whose FWHM_{obs} matches FWHM_{psf} . Based on

Table 9. The sizes of star-forming regions and H II regions in the galaxies under study

Galaxy	V_{hel} , km s ⁻¹	Distance, Mpc	Scale, pc arcsec ⁻¹	Size	
				arcsec	kpc
0837+4717	12751 ± 45	170	829	0.9	0.70
0910+5011	10248 ± 75	137	675	0.6	0.40
0939+3601	4456 ± 60	59	286	2.0	0.60
0943+3500	6049 ± 54	81	398	1.3	0.50
1033+4757	1674 ± 60	22	94	<0.5	<0.05
1048+4700	11799 ± 42	157	761	1.4	1.00
1050+3714	7701 ± 60	103	494	1.6	0.80
1645+4137	9700 ± 21	129	626	1.7	1.10
1717+4955	1039 ± 18	14	69	1.3	0.09
1720+4412	8321 ± 18	110	550	1.0	0.60

a comparison with the relationship between FWHM_{psf} and FWHM for HS 0910+5011 (this galaxy was observed immediately before HS 1033+4757), we can place an upper limit on the effective size of an H II region in this galaxy, ≈ 0.3 of FWHM_{psf} or $\approx 0''.5$ or 0.05 kpc. The size of the underlying galaxy can be estimated by analyzing the continuum profile along the slit. The galaxy is considerably larger than the emission-line region, as can be seen from a comparison of the normalized intensity profiles for [O III] 5007 Å and the continuum near this line. After comparison with FWHM_{psf} , the estimated effective size of the galaxy along the slit is $\text{FWHM} = 4''.2$, or 0.4 kpc.

This is one of the closest galaxies among those studied here and one of the BCGs with the lowest luminosity ($M_B > -12.7$).

HS 1048+4700. A comet-shaped galaxy with a bright head in the north and a tail elongated southward. The bright part of the head has the effective size $\text{FWHM} = 6''.0 \times 4''.1$, and its major axis is oriented at $\text{PA} = 14^\circ$. The galaxy's maximum size is $16'' \times 8''$. The slit passed in the NS direction through the nucleus.

1050+3714=CG 793. This consists of two compact galaxies in contact, whose centers are $13''$ apart, with CG 793 in SW and CG 794 in NE. The bright central part of the galaxy is essentially star-like, $\text{FWHM} = 2''.4 \times 2''.2$. The galaxy's maximum size is $13'' \times 13''$.

The slit passed in the NS direction through the CG 793 center. The profiles of all lines along the slit show the presence of two star-forming regions $\approx 3''$ apart, which corresponds to a linear distance of 1.5 kpc. The main (in energy) southern component ($\approx 70\%$ of the total flux 0.92×10^{-14} erg cm⁻² s⁻¹) of H α is observed from a region of $\text{FWHM}_{\text{obs}} = 6.5$ pixels in size. Given the PSF determined at a wavelength of 6700 Å ($\text{FWHM}_{\text{psf}} = 5.1$ pixels), we can estimate the effective size of the H α emission, $\text{FWHM} = 4$ pixels, which corresponds to $1''.6$, or 0.8 kpc. The second component is

0.5 kpc in size, and its H α flux accounts for $\approx 30\%$ of the total flux. It is in the brighter southern component that we observed [O III] $\lambda 4363$ Å and, consequently, it is for this component that we determined the elemental abundances given below.

All lines in the galaxy's 2D spectrum are noticeably tilted across the direction of dispersion, suggesting systematic motions through the galaxy body. These motions may also be produced by the interaction with CG 794. To test the hypothesis that there are systematic motions, we extracted five 1D spectra from the 2D linearized spectrum of CG 793 by the summation of five pixels in height in each of them. The averaging length was chosen from a comparison with $\text{FWHM}_{\text{psf}} \approx 5$ pixels = $2''$ for the spectrophotometric standard observed before the object. We subtracted the velocity of the central point, and the resulting difference is shown in Fig. 2.

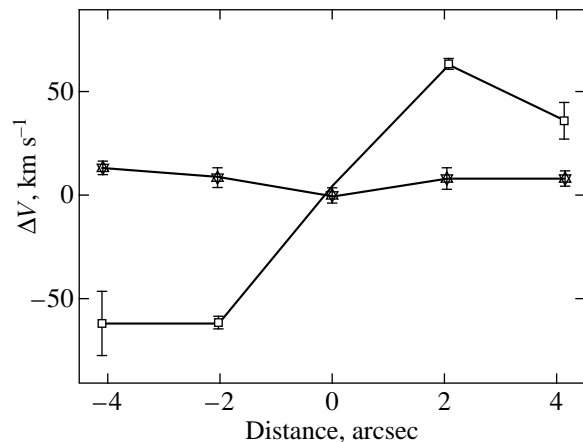


Fig. 2. The rotation curve for CG 793 constructed by using H α . Variations in the wavelength (on the scale of relative velocities) of the $\lambda 6717.05$ Å line in the reference spectrum are indicated by stars, and variations in the velocity of line-emitting gas of the galaxy along the slit for H α are indicated by squares. The vertical bars indicate errors for each point. For the slit directed NS, the south corresponds to a positive velocity in the figure.

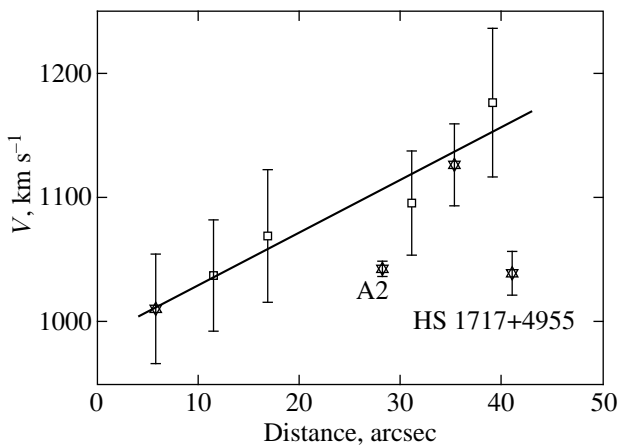


Fig. 3. The rotation curve for UGC 10806. The stars and squares represent velocities for the regions from the receding and approaching arms of this galaxy, respectively. The vertical bars indicate errors for each point. The solid line represents a linear fit to the observed points. The positions of HS 1717+4955 and region A2 which were not used in constructing the rotation curve are marked.

It can be seen from the figure that there is apparently rotation in this galaxy with an amplitude of $\approx 60 \text{ km s}^{-1}$. The errors of the velocities in the figure correspond to the errors in the centers of H α when fitting a Gaussian to its profile. To check whether the possible instrumental trends attributable to the reduction procedure (2D linearization) affect the result, we carried out the same procedure for the close (in wavelength) $\lambda 6717.05 \text{ \AA}$ line from the 2D linearized reference spectrum. The result for this line is also shown in Fig. 2. It follows from the figure that the amplitude of systematic motions in the galaxy exceeds the possible systematic effects by a factor of 5 or 6.

HS 1645+4137. An irregular galaxy elongated in the NS direction with a bright $\approx 10''$ region in the northern part of the galaxy and a broad curved southward tail. The galaxy's maximum size is $28'' \times 20''$.

The slit passed in the EW direction through the brightest part of the galaxy. A comparison of the H α profile with FWHM_{psf} shows that the emission has a complex morphology and consists of a narrow component (60% of the H α flux) with $\text{FWHM} = 4.1$ pixels, or $1''.7$ (1.1 kpc), and a broad component, which apparently corresponds to the tail in the direct image. The size of the broad component is $\text{FWHM} = 7.4$ pixels (or $3''$), corresponding to 1.9 kpc.

HS 1717+4955. Its direct image suggests that this is either a giant H II region at the W edge ($\approx 50''$, or 3.5 kpc, from the center) of the dwarf spiral UGC 10806 [$\text{SB}(s)\text{dm}$, $\approx 120''$, or 8.5 kpc in diameter, $M_B = -16.8$] seen at an angle of the order of or more than 60° to the line of sight, or a very low-mass companion of the same galaxy. In the latter case, HS 1717+4955 is the closest galaxy of all the BCGs considered here. The size of this

very compact object is $\text{FWHM } 4''.9 \times 3''.7$ with the position angle of its major axis $\text{PA} = 63^\circ$ for the characteristic star size in the image $\text{FWHM} = 3''.0 \times 3''.0$. This yields an estimate of the true effective size for the object $3''.9 \times 2''.2$, or 0.27×0.15 kpc. The maximum size of this region in DSS-2 is about $7'' \times 7''$ (≈ 0.5 kpc). The profiles of all lines along the slit show a complex structure of star-forming regions; apart from the main component whose parameters are given in Table 9, there is an extended component accounting for $\approx 45\%$ of the total flux with $\text{FWHM} = 0.24$ kpc, in good agreement with the estimate obtained from the direct image.

It is hoped that the nature of HS 1717+4955 will be elucidated by comparing the rotation curve of the disk galaxy UGC 10806 at its western edge and the radial velocity of this object. For this purpose, we obtained two 2D spectra. One spectrum was taken for the slit crossing almost the entire galaxy UGC 10806 at an angle of $\approx 20^\circ$ to the major axis and passing close to the center of this galaxy. The second spectrum was taken for the slit at the same position angle but centered on HS 1717+4955. Both spectra were reduced and calibrated in wavelength by using the same dispersion curve, which eliminates the systematic shift in measured velocities.

The rotation curve for UGC 10806 was constructed from radial-velocity measurements of six emission-line regions falling within the slit in the first spectrum. The total extent of the region used to construct the rotation curve is $\approx 70''$, or ≈ 5 kpc. The derived rotation curve, together with the errors in individual velocities, is shown in Fig. 3. To increase the accuracy of its construction, the points from the approaching and receding parts of the rotation curve were combined and are indicated by different symbols. Also shown in this figure are the position and velocity of HS 1717+4955. It is clear from the above rotation curve extrapolated to the distance from the center corresponding to the position of HS 1717+4955 that the radial velocity of this object is approximately 120 km s^{-1} lower than it would be if the object belonged to the kinematic system of matter in the disk galaxy. This most likely suggests that the object is a dwarf companion galaxy. Interestingly, there is yet another compact emission-line region marked by A2 in Fig. 3 whose velocity is close to that of HS 1717+4955 and differs significantly from the calculated rotation velocity of UGC 10806 by -60 km s^{-1} . This object may also be a dwarf companion of the disk galaxy.

HS 1720+4412. A galaxy elongated in the EW direction. Its maximum size in DSS-2 is $20'' \times 12''$. The prominent bright central region has $\text{FWHM} = 5''.8 \times 4''.0$ with the position angle of its major axis $\text{PA} = 75^\circ$. The slit passed in the EW direction through the central bright region.

3.2. Elemental Abundances

As was already noted above, this study had the following goals: (1) to test the validity of the procedure for selecting candidates for the most metal-deficient galaxies based on snapshot spectra obtained with short integration times (a few minutes); and (2) to test the techniques for data reduction and estimating the accuracy of derived elemental abundances based on spectra with integration times of several tens of minutes.

A comparison of heavy-element abundances in the BCGs from our sample (see Table 8) with other abundance analyses of heavy elements in similar galaxies [4, 37] shows that, when using the same method of calculations, our results are quite comparable. The derived O, N, Ne, S, Ar, and Fe abundances fall nicely on the $\log(\text{O}/\text{H})$ dependences of $\log(X/\text{O})$ from [4], and the considerably larger measurement errors are attributable solely to the integration time of the spectra under study. Here, X is the abundance of one of the heavy elements.

As expected, the heavy-element abundances in H II regions for six of the ten galaxies studied here turned out to be very low, less than 1/10 of their solar values (corresponding to $12 + \log(\text{O}/\text{H}) \leq 7.92$; [46]). In particular, HS 0837+4717 with an oxygen abundance $12 + \log(\text{O}/\text{H}) \leq 7.7$ is one of the most metal-deficient galaxies among those presented here and one of the likely candidates for young galaxies, according to the recently proposed criterion of a sufficiently low $[\leq 1/20(\text{O}/\text{H})_{\odot}]$ oxygen abundance [4]. The fact that the derived heavy-element abundances are correct is confirmed by subsequent spectroscopic observations with a higher signal-to-noise ratio of the two most interesting objects, HS 0837+4717 [45] and HS 1033+4757 [48].

3.3. On the Relationships between Observed BCG Parameters

Although our sample of blue compact objects is rather small, it is of interest to trace possible relationships between the parameters of the host galaxy and its star-forming regions. We compared the linear sizes of the giant H II complexes [49] from Table 9 and the absolute magnitudes of the host galaxies from Table 1. There is a clear relationship between these parameters: as the galaxy's luminosity increases by two orders of magnitude, the sizes of its giant H II complexes increase by approximately an order of magnitude. This type of relationship has recently been found by Elmegreen *et al.* [50] using a sample of 16 BCGs. Our independent data for ten BCGs based on size measurements for giant H II complexes using emission in strong H α or [O III] $\lambda 5007$ Å lines confirm the results of Elmegreen *et al.* [50]. As was pointed out by these authors, such a dependence apparently stems from the fact that the maximum size of the region of gravitational instability in galactic disks is several-fold smaller than the galaxy size.

Another dependence for low-mass galaxies with active star formation, which has long been discussed in the literature, is a statistical correlation between the total luminosity or mass of a galaxy and the metallicity (or oxygen abundance) in its H II regions [51, 52]. According to these authors, the lower the luminosity of a galaxy, the lower its oxygen abundance. Despite the luminosity range of more than two orders of magnitude, our data provide no evidence for this correlation. A similar conclusion has recently been reached by Hidalgo-Gamez and Olofsson [53].

4. CONCLUSION

We have presented the first results of our program of search for blue compact galaxies with the largest deficiency of elements heavier than helium. In currently available models of galactic evolution, these are the youngest galaxies that have undergone only one or more episodes of active star formation in their history. We tested the criteria for selecting such candidates from snapshot spectroscopy for subsequent spectroscopy with a high signal-to-noise ratio. The methodical problems of separating spectra of the brightest emission-line region to determine elemental abundances were also tested on this first group of galaxies. Our results have led us to the following conclusions:

(1) We discovered six new galaxies with a metallicity of the gas in the H II regions around the region of on-going star formation $Z < 1/10Z_{\odot}$. The abundances of other heavy elements (N, Ne, S, Ar) in all the galaxies studied relative to oxygen (within the moderately high accuracy achieved here) are in good agreement with the means deduced by Izotov and Thuan [4] and Thuan *et al.* [54] for a subsample of BCGs with $12 + \log(\text{O}/\text{H}) < 8.0$.

(2) Two of the BCGs studied with $12 + \log(\text{O}/\text{H}) < 7.7$, HS 0837+4717 and HS 1033+4757, have a metallicity that is low enough to consider them as candidates for galaxies with the first burst of star formation. They require both higher quality spectra, for a more accurate determination of their heavy-element abundances, and color data for the extended envelopes around the central region of on-going star formation. The galaxy CG 793 is also an object of very low metallicity and is of great interest in studying the early chemical evolution.

(3) We detected broad, low-contrast components in strong [O III] emission lines, which correspond to emitting-gas velocities of ~ 2500 km s $^{-1}$, in HS 0837+4717. It appears to be one of the most metal-deficient galaxies in which high-velocity gas motions show up in this way. This galaxy should be studied in more detail, in particular, because of possible peculiarities of its chemical evolution as, for example, for Mrk 996 in [55].

(4) Apart from strong emission around the star-forming region at the center, we detected a distant peripheral region with strong emission lines in CG 285, which is virtually unseen in continuum, and has a very low brightness in the direct image.

(5) The object of very low luminosity HS 1717+4955 was found to be a likely companion of the dwarf spiral UGC 10806, whose luminosity is approximately a factor of 40 higher. This pair is an interesting example of interacting galaxies in a fairly close vicinity of our galaxy. The mutual gravitational influence appears to trigger intense star formation both in the lowest mass, compact companion, and in the disk galaxy.

ACKNOWLEDGMENTS

We wish to thank A.N. Burenkov for help with the observations and Yu.I. Izotov for the code of abundance computations from emission-line spectra of H II regions and for helpful discussions. The search and study of young galaxies at SAO were supported by the Russian Foundation for Basic Research (project no. 97-2-16755) and the Cosmion Science and Education Center. The international collaboration on this project was supported in part by the INTAS grant (no. 96-0500). The observations with the 6-m telescope became possible owing to a special support from the Ministry of Education and Technology of the Russian Federation for the 6-m SAO telescope (BTA, registration no. 01-43).

REFERENCES

1. T. X. Thuan, *Massive Stars in Starbursts*, Ed. by C. Leitherer *et al.* (Cambridge Univ. Press, Cambridge, 1991), p. 183.
2. L. Searle and W. L. W. Sargent, *Astrophys. J.* **173**, 25 (1972).
3. D. Kunth, J. Lequeux, W. L. W. Sargent, *et al.*, *Astron. Astrophys.* **282**, 709 (1994).
4. Yu. I. Izotov and T. X. Thuan, *Astrophys. J.* **511**, 639 (1999).
5. L. van Zee, D. Westpfahl, M. Haynes, *et al.*, *Astron. J.* **115**, 1000 (1998).
6. Yu. I. Izotov, N. G. Guseva, V. A. Lipovetsky, *et al.*, *Nature* **343**, 238 (1990).
7. Yu. I. Izotov, N. G. Guseva, V. A. Lipovetsky, *et al.*, *Astron. Astrophys.* **247**, 303 (1991).
8. T. X. Thuan, Yu. I. Izotov, and V. A. Lipovetsky, *Astrophys. J.* **477**, 661 (1997).
9. T. X. Thuan and Yu. I. Izotov, *Astrophys. J.* **489**, 623 (1997).
10. Yu. I. Izotov, V. A. Lipovetsky, F. H. Chaffee, *et al.*, *Astrophys. J.* **476**, 698 (1997).
11. V. A. Lipovetsky, F. H. Chaffee, Yu. I. Izotov, *et al.*, *Astrophys. J.* **519**, 177 (1999).
12. P. Papaderos, Yu. I. Izotov, K. J. Fricke, *et al.*, *Astron. Astrophys.* **338**, 43 (1998).
13. S. A. Pustilnik, E. Brinks, T. X. Thuan, *et al.*, *Astron. J.*, 1999 (in press).
14. T. X. Thuan, *Astrophys. J.* **268**, 667 (1983).
15. H.-H. Loose and T. X. Thuan, *Astrophys. J.* **309**, 59 (1986).
16. R. Terlevich, J. Melnik, J. Masegosa, *et al.*, *Astron. Astrophys.*, Suppl. Ser. **91**, 285 (1991).
17. J. Masegosa, M. Moles, and A. Campos-Aguilar, *Astrophys. J.* **420**, 576 (1994).
18. S. A. Pustilnik, V. A. Lipovetsky, Yu. I. Izotov, *et al.*, *Pis'ma Astron. Zh.* **23**, 350 (1997) [*Astron. Lett.* **23**, 308 (1997)].
19. Yu. I. Izotov, V. A. Lipovetsky, N. G. Guseva, *et al.*, *The Feedback of Chemical Evolution on the Stellar Content of Galaxies*, Ed. by D. Alloin and G. Stasinska (Observatoire Paris-Meudon, Meudon, 1992), p. 127.
20. Yu. I. Izotov, N. G. Guseva, V. A. Lipovetsky, *et al.*, *Astron. Astrophys. Trans.* **3**, 179 (1993).
21. J. J. Salzer, J. W. Moody, J. L. Rosenberg, *et al.*, *Astron. J.* **109**, 2376 (1995).
22. A. V. Ugryumov, Candidate's Dissertation (Nizhniĭ Arkhyz, Spets. Astrofiz. Obs., 1997) (http://precise.sao.ru/Laboratory/aref_and).
23. A. V. Ugryumov, S. A. Pustilnik, V. A. Lipovetsky, *et al.*, *Astron. Astrophys.*, Suppl. Ser. **131**, 295 (1998).
24. V. A. Lipovetsky, D. Engels, A. Ugryumov, *et al.*, *New Horizons from Multi-Wavelength Sky Surveys*, *IAU Symp. No. 179, Baltimore*, Ed. by B. J. McLean *et al.* (Kluwer Academic Publishers, Dordrecht, 1998), p. 299.
25. A. V. Ugryumov, D. Engels, V. A. Lipovetsky, *et al.*, *Astron. Astrophys.*, Suppl. Ser. **135**, 511 (1999).
26. S. A. Pustilnik, D. Engels, A. V. Ugryumov, *et al.*, *Astron. Astrophys.*, Suppl. Ser. **137**, 299 (1999).
27. J. Salzer, V. A. Lipovetsky, T. Boroson, *et al.*, *Bull. Am. Astron. Soc.* **26**, 916 (1994).
28. A. Yu. Kniazev, Candidate's Dissertation (Nizhniĭ Arkhyz, Spets. Astrofiz. Obs., 1997) (http://precise.sao.ru/Laboratory/Dis_akn).
29. V. L. Afanas'ev, A. N. Burenkov, V. V. Vlasyuk, *et al.*, *Otchet Spets. Astrofiz. Obs.*, No. 234, 1 (1995).
30. P. Massey, K. Srtobel, J. V. Barnes, *et al.*, *Astrophys. J.* **328**, 315 (1988).
31. A. Yu. Kniazev and T. F. Kniazeva, *Otchet Spets. Astrofiz. Obs.*, No. 249, 1 (1995).
32. V. V. Zin'kovskii, A. Yu. Kniazev, V. I. Levitan, *et al.*, *Otchet Spets. Astrofiz. Obs.*, No. 221, 1 (1994).
33. A. Yu. Kniazev, and V. S. Shergin, *Otchet Spets. Astrofiz. Obs.*, No. 239, 1 (1995).
34. P. Grosbøl, *Reviews in Modern Astronomy*, Ed. by G. Klark (Springer-Verlag, Heidelberg, Berlin, 1989), Vol. 2, p. 242.
35. V. S. Shergin, A. Yu. Kniazev, and V. A. Lipovetsky, *Astron. Nachr.* **317**, 95 (1996).
36. A. Yu. Kniazev, V. S. Shergin, V. A. Lipovetsky, *4th ESO/ST-ECF Data Analysis Workshop* (1992), p. 169.
37. Yu. I. Izotov, T. X. Thuan, and V. A. Lipovetsky, *Astrophys. J.* **435**, 647 (1994).
38. Yu. I. Izotov, T. X. Thuan, and V. A. Lipovetsky, *Astrophys. J.*, Suppl. Ser. **108**, 1 (1997).
39. G. Stasin'ska, *Astron. Astrophys.*, Suppl. Ser. **83**, 501 (1990).
40. D. R. Garnett, *Astron. J.* **103**, 1330 (1992).
41. L. H. Aller, *Physics of Thermal Gaseous Nebulae* (Reidel, Dordrecht, 1984).

42. E. Skillman and R. C. Kennicutt, *Astrophys. J.* **411**, 655 (1993).
43. Yu. I. Izotov, A. B. Dyak, F. H. Chaffee, *et al.*, *Astrophys. J.* **458**, 524 (1996).
44. H. O. Castañeda, J. M. Vilchez, and M. V. F. Copetti, *Astrophys. J.* **365**, 164 (1990).
45. S. A. Pustilnik, A. Yu. Kniazev, C. Foltz, *et al.*, 1999 (in press).
46. Yu. I. Izotov, T. X. Thuan, and C. B. Foltz, *Astrophys. J.*, 1999 (in press).
47. E. Anders and N. Grevesse, *Geochim. Cosmochim. Acta* **53**, 197 (1989).
48. A. Yu. Kniazev, S. A. Pustilnik, A. V. Ugryumov, *et al.*, 1999 (in press).
49. Yu. N. Efremov, *Sites of Star Formation* (Nauka, Moscow, 1989).
50. B. G. Elmegreen, D. M. Elmegreen, J. J. Salzer, *et al.*, *Astrophys. J.* **467**, 579 (1996).
51. J. Lequeux, M. Peimbert, J. F. Rayo, *et al.*, *Astron. Astrophys.* **80**, 155 (1979).
52. E. Skillman, R. C. Kennicutt, and P. W. Hodge, *Astrophys. J.* **347**, 875 (1989).
53. A. M. Hidalgo-Gómez and K. Olofsson, *Astron. Astrophys.* **334**, 45 (1998).
54. T. X. Thuan, Yu. I. Izotov, and V. A. Lipovetsky, *Astrophys. J.* **445**, 108 (1995).
55. T. X. Thuan, Yu. I. Izotov, and V. A. Lipovetsky, *Astrophys. J.* **463**, 120 (1996).

Translated by V. Astakhov

A Model for the Molecular Accretion Disk and H₂O Maser in the Nucleus of the Galaxy NGC 4258

N. S. Babkovskaya* and D. A. Varshalovich

Ioffe Physicotechnical Institute, Russian Academy of Sciences, ul. Politekhnikeskaya 26, St. Petersburg, 194021 Russia

Received September 24, 1999

Abstract—A model is developed for the H₂O maser source observed in the circumnuclear region of the galaxy NGC 4258. The maser emission originates at distances of 0.15–0.29 pc from the center in a thin, cold accretion disk (gas–dust torus) rotating around a supermassive black hole of mass $4 \times 10^7 M_{\odot}$. The conditions for the emergence of an inverse population of the signal 6₁₆–5₂₃ levels in ortho-H₂O working molecules are simulated numerically. The complex line profile, which includes both central and high-velocity components, is calculated. A comparison of the calculations with radiointerferometric and spectrophotometric observations allowed the physical conditions in the emitting region to be determined. © 2000 MAIK “Nauka/Interperiodica”.

Key words: active galactic nuclei, quasars, radio galaxies

INTRODUCTION

Considerable progress in elucidating the nature of active galactic nuclei has become evident in connection with a radiointerferometric study of the H₂O maser emission from the nuclear region of the giant spiral SABbc galaxy NGC 4258 (M 106) located at distance $D = 7.3 \pm 0.3$ Mpc [1]; Miyoshi *et al.* [2] obtained a different estimate, $D = 6.4 \pm 0.9$ Mpc. The galaxy has a complex structure with inner and outer spiral arms [3], a dust lane, and jets, which are observed both in the optical (H α) and radio ranges. By the characteristic appearance of its optical spectrum, NGC 4258 was initially classified as a Seyfert 2 galaxy or, more precisely, as Sy 1.9. Subsequently, it was classified as belonging to the subgroup of the so-called LINERs (Low Ionization Nuclear Emission Region). The total luminosity L of the nucleus of this galaxy is 10^{42} – $10^{44} L_{\odot}$ erg s^{–1} [4]. Since the galaxy nucleus itself is completely obscured by a gas–dust disk, $A_V > 100$, it can be observed optically only in scattered, linearly polarized light [4]. Accordingly, the emission as viewed by the observer is mainly concentrated in the near infrared. However, X-ray emission with a luminosity of $(4.4 \pm 1.1) \times 10^{40} (D/7.3 \text{ Mpc})^2$ erg s^{–1} was detected in the 3–10-keV band [1].

NGC 4258 is unique in that the line of sight lies virtually in the plane of the molecular gas–dust accretion disk. That is why we can observe the maser emission from the disk. In this study, an attempt is made to restore the structure of the accretion disk by comparing observational data with calculations of the intensity of the maser emission. We were able to do this, because both the intensity and the spectral line profile are highly

sensitive, first, to the number density and temperature of the H₂O working molecules and H₂ buffer gas and, second, to the geometry of the system and the gas velocity field, whose gradient determines the amplification path length before the emergence from resonance, 10^{14} – 10^{15} cm.

The H₂O maser emission from the nucleus of NGC 4258 was first detected by Claussen *et al.* [5]; however, the first spectra were obtained in a narrow range of frequencies (velocities) corresponding to the central, most intense components of the maser line. Only a decade later did Nakai *et al.* [6] measure the spectrum in a wider frequency range and detected high-velocity components to the right and to the left of the central line (Fig. 1). Three hypotheses about the nature of the high-velocity components of maser emission were proposed: (a) a bipolar jet, (b) nonlinear scattering in a dense plasma, and (c) a molecular disk [6]. The nature of these components was finally elucidated only after VLBI measurements, which yielded a high-angular-resolution map of the spatial distribution of maser subsources [2].

An analysis of the interferogram revealed that the high-velocity components of the maser line arise in the right and left wings of a thin molecular disk (gas–dust torus) seen edge-on. The inclination i_0 of the disk spin axis to the line of sight is $97^\circ \pm 4^\circ$. Moreover, the maser features turned out to fall nicely on the Keplerian radial-velocity (V_s) curve

$$V_s - V_0 = \sqrt{\frac{GM}{R}} \sin i_0 \sin \theta, \quad (1)$$

where θ is the angle between the direction of observation and the velocity vector of the maser region: $\theta = 0^\circ \pm 3^\circ$ for the central component of the maser line and $\theta = 90^\circ \pm 4^\circ$ for the high-velocity components, R is the

* E-mail address for contacts: bns@astro.ioffe.rssi.ru

radius of the Keplerian orbit, and V_0 is the apparent recession velocity of the disk [7].

The maximum and minimum rotation velocities of the maser features are $V_{\max} = 1080 \pm 2 \text{ km s}^{-1}$ and $V_{\min} = 770 \pm 2 \text{ km s}^{-1}$, the radius R_{in} of the inner maser subsource corresponding to V_{\max} is 0.15 pc ($D/7.3 \text{ Mpc}$), whereas the radius R_{out} of the outer subsource corresponding to V_{\min} is 0.29 pc ($D/7.3 \text{ Mpc}$) [2] (Fig. 1). Owing to these measurements, the central mass inside the disk was determined for the first time with a high accuracy: $M = (4.0 \pm 0.25) \times 10^7 M_{\odot}$ ($D/7.3 \text{ Mpc}$) [1]. The only explanation for the existence of such a large mass in such a small region is the presence of a super-massive black hole.

According to radio observations, the velocity V_0 of the maser disk with respect to the Local Standard of Rest (LSR) is $476 \pm 2 \text{ km s}^{-1}$ [8]. It includes the galaxy's cosmological recession velocity of 470 km s^{-1} , a gravitational redshift $GM/(Rc) \sim 4 \text{ km s}^{-1}$, and a shift $GM/(2Rc) \sim 2 \text{ km s}^{-1}$ associated with the transverse Doppler effect. The velocity V_0 measured in the heliocentric coordinate system is lower by 8.2 km s^{-1} [7].

An upper limit on the maser-disk mass, $M < 4 \times 10^6 M_{\odot}$, was derived from the deviation of $V_s(R)$ from the Keplerian curve; the accretion rate is $\dot{M} = 1.5 \times 10^{-4} M_{\odot} \text{ yr}^{-1}$ [1]; the radial velocity of the disk gas, as inferred from observational data, does not exceed 10 km s^{-1} [2].

THE MASER PUMPING MECHANISM

To calculate the populations n_k of energy levels ϵ_k in the ortho- H_2O molecule, we used the set of population balance equations, which includes all possible collisional and radiative transitions between the first thirty rotational levels of ortho- H_2O ,

$$\sum_k n_k W_{ki} = n_i \sum_k W_{ik} \quad (2)$$

with the normalization condition

$$\sum_k n_k = n_{\text{H}_2\text{O}}, \quad (3)$$

where $i = 1, 2, \dots, n_{\text{H}_2\text{O}}$ is the number density of water molecules, $W_{ik} = C_{ik} + R_{ik}$ is the total rate of the $i \rightarrow k$ transition,

$$C_{ik}^{\uparrow} = n_{\text{H}_2} k_{ik}(T_{\text{kin}}), \quad C_{ki}^{\downarrow} = C_{ik}^{\uparrow} \frac{g_i}{g_k} \exp\left(\frac{\epsilon_k - \epsilon_i}{kT_{\text{kin}}}\right) \quad (4)$$

are the rates of collisional excitation $i \rightarrow k$ and deexcitation $k \rightarrow i$ ($\epsilon_k > \epsilon_i$), g_i is the statistical weight, n_{H_2} and T_{kin} are the number density and temperature of the H_2 buffer gas,

$$R_{ik}^{\uparrow} = \int A_{ik} \rho_{ik} \frac{d\Omega}{4\pi}, \quad R_{ki}^{\downarrow} = \int A_{ki} (1 + \rho_{ki}) \frac{d\Omega}{4\pi}, \quad (5)$$

are the rates of radiative excitation $i \rightarrow k$ and deexcitation $k \rightarrow i$, $A_{ik} = g_k/g_i A_{ki}$ are the Einstein coefficients determining the probability of a spontaneous transition, $\rho(\nu, \mathbf{n}) = I(\nu, \mathbf{n})c^2/2h\nu^3$ is a dimensionless intensity of the emission (the number of photons in a cell of phase space), and \mathbf{n} is the direction of propagation of the emission. Collisional excitation and radiative deexcitation were taken into account by using data from [9] and [10], respectively.

Since the disk is thin and since the fraction of the solid angle in which the medium is optically thick is extremely small, $\Omega/4\pi \ll 1$, the maser amplification takes place only in a very narrow solid angle. We restrict ourselves to the case of an unsaturated maser, where the inverse effect of maser emission on signal level populations can be disregarded. This is confirmed, in particular, by the observed narrowness of the high-velocity line components. The above assumption allows us to ‘‘uncouple’’ the population-balance and radiative-transfer equations, i.e., to calculate the populations of ortho- H_2O levels locally at each point and to integrate the equations of radiative transfer by using the already known populations.

For a sufficiently homogeneous medium, the solution of the transfer equation is

$$I_{\nu}(\tau) = I_{\nu}(0) \exp(-\tau) + S_{\nu}^{\text{ex}} (1 - \exp(-\tau)), \quad (6)$$

where τ_{ν} is the optical depth at frequency ν :

$$\tau(R, \theta) = \int_{-\infty}^{\infty} \Phi_{\nu}(s) \frac{\lambda^2}{8\pi} g_2 A_{21} \left(\frac{n_1}{g_1} - \frac{n_2}{g_2} \right) ds, \quad (7)$$

$$\Phi_{\nu}(s) = \frac{1}{\sqrt{\pi} \Delta v_D} \exp\left(-\left(\frac{\nu - \nu_0(1 - V_s/c)}{\Delta v_D}\right)^2\right), \quad (8)$$

$$\Delta v_D = \frac{v_0 V_T}{c},$$

where V_s is the line-of-sight velocity component. The emission intensity I_{ν} and the source function S_{ν}^{ex} in equation (6) can be expressed in terms of radiation temperature T_R and excitation temperature T_{ex} : $I_{\nu} = 2kT_R/\lambda^2$ and $S_{\nu}^{\text{ex}} = 2kT_{\text{ex}}/\lambda^2$.

Thus, in the case of normal absorption ($T_{\text{ex}} > 0$, $\tau > 0$), i.e., in the lines providing the radiative pumping of the maser, the radiation temperature averaged over the solid angle can be represented for a large optical depth as

$$\langle T_R \rangle = \frac{1}{4\pi} \int T_{\text{ex}} [1 - \exp(-\tau)] d\Omega \approx T_{\text{kin}} \frac{\Omega}{4\pi}. \quad (9)$$

In the case of negative absorption ($T_{\text{ex}} < 0$, $\tau < 0$), the maser radiation temperature is given by

$$T_R(\tau) = T_R(0) \exp|\tau| + |T_{\text{ex}}| (\exp|\tau| - 1), \quad (10)$$

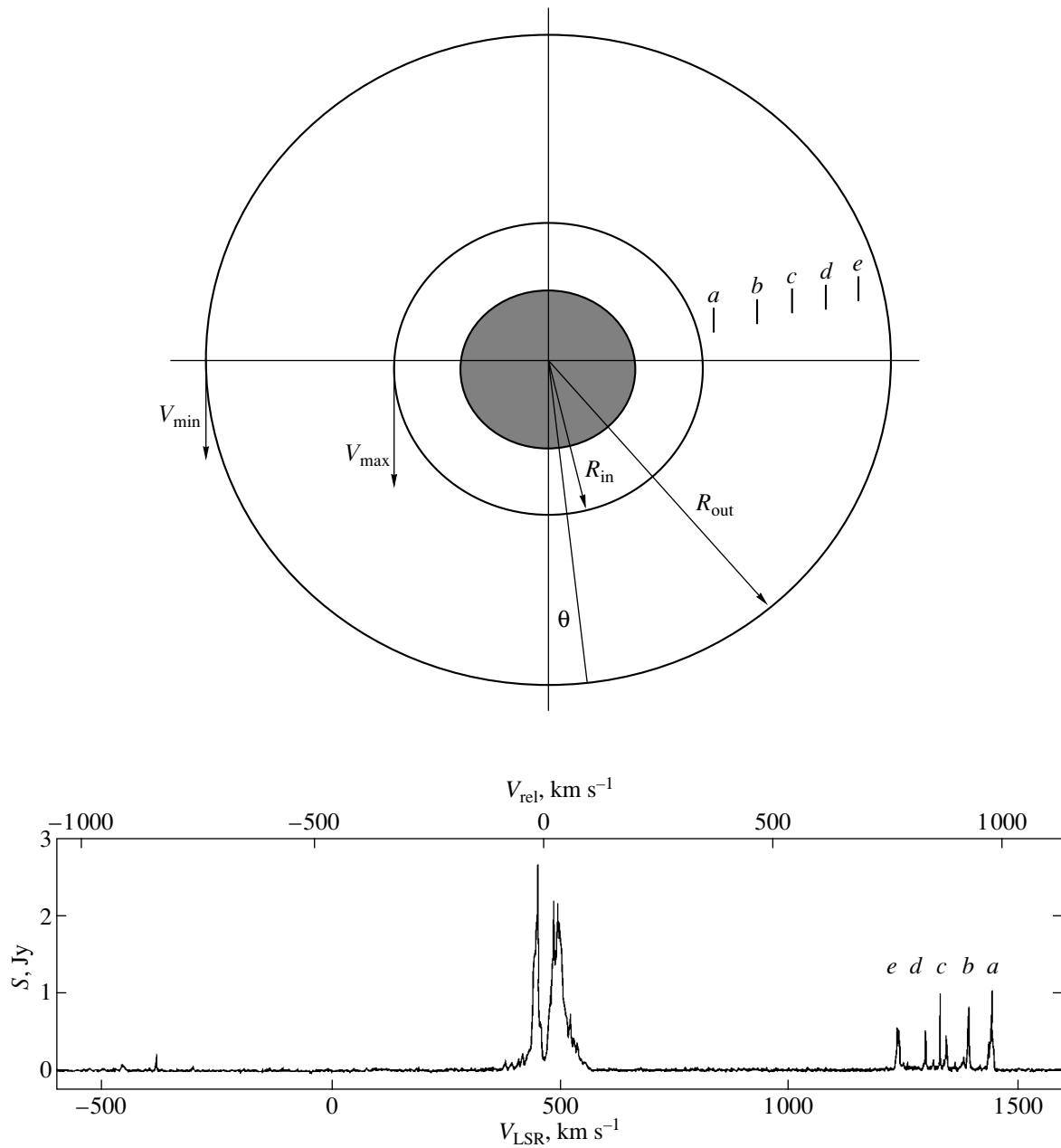


Fig. 1. A scheme of the molecular disk and the spectrum of maser emission in NGC 4258 [6] (published with permission of the authors).

where $T_R(0)$ is the brightness temperature of the ~ 22 -GHz emission arising from the inner region and illuminating the maser.

A QUALITATIVE DESCRIPTION OF THE PUMPING MECHANISM

Figure 2 presents the results of an exact numerical calculation of the dependence of signal-level inversion

$$U = (n_u/g_u - n_l/g_l)/n_{H_2O} \tag{11}$$

for the ortho- H_2O molecule on hydrogen number density n_{H_2} and temperature T_{kin} .

Our numerical analysis has shown that, in the case under consideration, the RR radiative pumping mechanism is dominant. The main contribution to the emergence and magnitude of the inversion comes from the pumping cycle $4_{14} \rightarrow 5_{05} \rightarrow 6_{16} \rightarrow 5_{23} \rightarrow 4_{14}$. This cycle is schematically shown in Fig. 3.

The populations of the 6_{16} , 4_{14} and 5_{23} , 4_{14} levels are related by

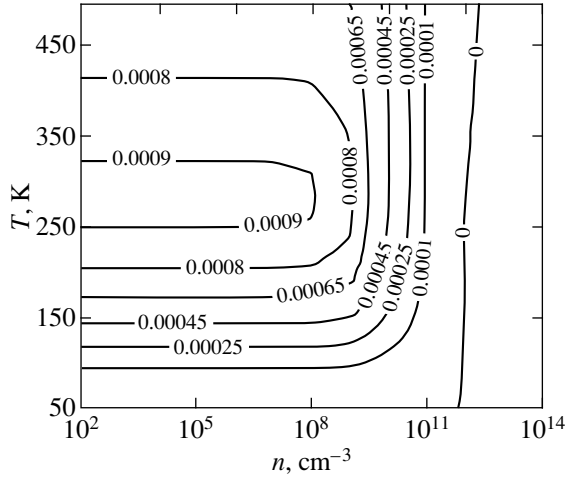


Fig. 2. Inversion U (11) of the populations of the $6_{16}\text{--}5_{23}$ signal levels in the ortho- H_2O molecule versus number density and temperature of molecular hydrogen.

$$\frac{n(6_{16})}{n(4_{14})} = \frac{n(6_{16})n(5_{05})}{n(5_{05})n(4_{14})}$$

$$= \frac{g(6_{16})}{g(4_{14})} \exp\left(-\frac{\epsilon(6_{16}) - \epsilon(5_{05})}{kT_R^{6_{16} \rightarrow 5_{05}}}\right) \exp\left(\frac{\epsilon(5_{05}) - \epsilon(4_{14})}{kT_R^{5_{05} \rightarrow 4_{14}}}\right), \quad (12)$$

$$\frac{n(5_{23})}{n(4_{14})} = \frac{g(5_{23})}{g(4_{14})} \exp\left(-\frac{\epsilon(5_{23}) - \epsilon(4_{14})}{kT_R^{5_{23} \rightarrow 4_{14}}}\right),$$

the radiation temperatures T_R^{ik} in these $i \rightarrow k$ lines of the cycle satisfy the inequality $T_R^{4_{14} \rightarrow 5_{05}} \approx T_R^{5_{05} \rightarrow 6_{16}} \gg T_R^{5_{23} \rightarrow 4_{14}}$, because the oscillator strengths $\mu_{ik} \sim A_{ik}\lambda^3$ of the $4_{14} \rightarrow 5_{05}$ and $5_{05} \rightarrow 6_{16}$ transitions are a factor of 10 larger than that of the $5_{23} \rightarrow 4_{14}$ transition. The optical depths in these transitions, determined by the corresponding values of μ_{ik} , are therefore related by $\tau_{4_{14} \rightarrow 5_{05}} \approx \tau_{5_{05} \rightarrow 6_{16}} \approx 10\tau_{5_{23} \rightarrow 4_{14}}$.

Consequently, the fractions of the solid angles in which the medium is optically thick in the above lines are related by $\Omega^{4_{14} \rightarrow 5_{05}} \approx \Omega^{5_{05} \rightarrow 6_{16}} \gg \Omega^{5_{23} \rightarrow 4_{14}}$.

Thus, the radiation tends to excite molecules from the 4_{14} level (via the 5_{05} level) to the 6_{16} level and to deexcite the 5_{23} level through the transition to the 4_{14} level, forming a closed cycle of maser pumping and producing the signal-level inversion required for the maser amplification to emerge.

A detailed numerical calculation with allowance for all possible collisional and radiative transitions confirms that the main contribution to the pumping of

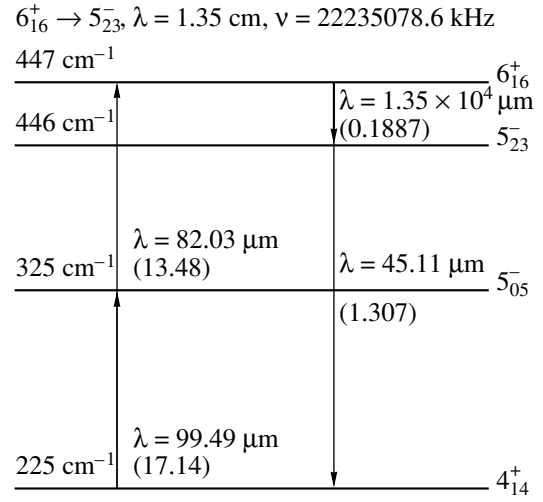


Fig. 3. A portion of the diagram of the ortho- H_2O rotational levels involved in the maser radiative pumping. The line oscillator strengths determining the optical depths and fluxes at the corresponding frequencies are given in parentheses.

maser levels comes from the mechanism considered in this section.

STRUCTURE OF THE MOLECULAR ACCRETION DISK

The critical distance at which ice particles in the Solar system are known to be completely destroyed by solar radiation is $\sim 1.5 \times 10^{13}$ cm. By analogy, we can estimate the critical distance of grain survival near the nucleus of the galaxy NGC 4258: $R_{\text{BH}}/R_{\odot})^2 = (L_{\text{BH}}/L_{\odot})$; for $L_{\text{BH}} = 10^{43}$ erg s^{-1} , $R_{\text{BH}} = 2 \times 10^{17}$ cm. At the distance corresponding to the inner disk radius, ice particles therefore survive even without obscuration by dust (which is very large, $A_V > 100$). The source of working H_2O molecules in the maser disk can thus be assumed to be ice dust.

According to observational data, the peak in the distribution of infrared radiation from the galaxy nucleus corresponds to a temperature of ~ 130 K. Since the most likely source of radiation in this wavelength range is dust, we conclude that the dust temperature is also ~ 130 K.

As the surface layers of the disk contain no dust responsible for gas cooling, the temperature in them is higher than the gas temperature in the central plane filled with dust; in addition, the hydrogen molecule is a factor of 9 less massive than the water molecule. We can therefore assert that the hydrogen atmosphere is much thicker than the layer containing H_2O molecules. The assumption that the diffusion flux of water molecules is low and that there is dynamical equilibrium on the dust surface is then valid, and we can use the satu-

rated-vapor equation for H₂O. In terms of the density of gas-phase H₂O molecules, this equation is

$$\begin{aligned} & \log(n_{\text{H}_2\text{O}}(T_d) \text{ (cm}^{-3}\text{)}) \\ & = a_1 - a_2/T_d + a_3 \log T_d - a_4 T_d - a_5 T_d^2, \end{aligned} \quad (13)$$

where $a_1 = 10.834292$, $a_2 = 2481.604$, $a_3 = 2.5721988$, $a_4 = 3.097203 \times 10^{-3}$, $a_5 = 1.7649 \times 10^{-7}$.

The maser emission intensity is extremely sensitive to the number density $n_{\text{H}_2\text{O}}$ of working molecules. Since, according to observational data, the intensities of the high-velocity maser peaks originating at different distances from the center are approximately the same, $n_{\text{H}_2\text{O}}(R) \approx \text{const}$ in the maser disk. Because of the strong dependence of $n_{\text{H}_2\text{O}}$ on T_d , we then conclude that $T_d(R) \approx \text{const} = 130 \text{ K}$ for $R_{\text{in}} \leq R \leq R_{\text{out}}$.

CONSTRUCTING A MODEL FOR THE MOLECULAR DISK

When constructing a model for the molecular accretion disk, we follow Shakura and Sunyaev [11] but use a different equation of energy balance, because the mechanism of heating and heat removal in the molecular disk is markedly different.

Let us write the continuity equation integrated over the disk thickness $2H$ as

$$\dot{M} = 2\pi \Sigma R V_r, \quad (14)$$

where V_r is the mean radial velocity of the matter in the disk, and $\Sigma = 2H\rho$ is the surface density ($\rho = m_{\text{H}_2} n_{\text{H}_2}$).

We assume that the disk is in hydrostatic equilibrium: the pressure gradient is balanced by the z component of the gravity of the central body (the self-gravitation of the disk may be disregarded, because the disk mass is much smaller than the central mass):

$$\frac{1}{\rho} \frac{dP}{dz} = -\frac{GM}{R^3} z = -\omega^2 z, \quad (15)$$

where $\omega = \sqrt{GM/R^3}$ is the Keplerian angular velocity.

We integrate equation (15) and average it over z by using the equation of state $P = nkT$ (k is the Boltzmann constant). As a result, we obtain the following relation for the mean pressure in the disk

$$P = \frac{\Sigma \omega^2 H}{4}. \quad (16)$$

Without going into the details of the vertical disk structure, we rewrite equation (15) by assuming $\Delta P = \rho C_s^2$ (C_s is the speed of sound) and $\Delta z = H$ (disk half-thickness). We then have

$$C_s = \omega H. \quad (17)$$

Since, according to observational data, the radial component of the gas velocity is much smaller than its tan-

gential component [2], we assume that the motion in the disk occurs in Keplerian circular orbits:

$$V_\phi = \sqrt{\frac{GM}{R}} = \omega R. \quad (18)$$

Then, from formulas (17) and (18) it follows that

$$\frac{C_s}{V_\phi} \approx \frac{H}{R}. \quad (19)$$

The radial motion in the disk is attributable to the friction of adjacent layers and to the exchange of angular momentum between them. The transfer of angular momentum in the disk is related to the moment of viscous forces by

$$\dot{M} \frac{d\omega R^2}{dR} = 2\pi \frac{d}{dR} W_{r\phi} R^2, \quad (20)$$

where $W_{r\phi}$ is the component of the viscous stresses in the disk

$$W_{r\phi} = -2\eta HR \frac{d\omega}{dR}, \quad (21)$$

η is the dynamic viscosity coefficient averaged over the z coordinate. In the case of isotropic turbulence, the viscosity coefficient is [12]

$$\eta = \frac{1}{3} \rho v_t l_t, \quad (22)$$

where v_t and l_t are the characteristic velocity and scale of turbulent pulsations. The values of v_t and l_t in the accretion disk are not known in advance. This uncertainty can be obviated by assuming that $v_t l_t = \alpha C_s H$, where α is a dimensionless parameter, called the turbulence parameter. Clearly, $l_t \leq H$ for isotropic turbulence. Since supersonic turbulence rapidly decays, $v_t \leq C_s$. We therefore assume that $\alpha \leq 1$.

Equation (20) for the change in angular momentum is easily integrated:

$$W_{r\phi} = -\frac{\dot{M}}{2\pi} \omega \left(1 - \left(\frac{R_0}{R} \right)^{1/2} \right) + W_{r\phi}(R_0), \quad (23)$$

where $W_{r\phi}(R_0)$ is the component of the viscous stress tensor in an orbit of radius R_0 .

When accretion onto a black hole is considered, the distance R_0 is assumed to correspond to the last stable orbit, $R_0 \sim R_g$ ($R_g \approx 10^{13} \text{ cm}$ is the gravitational radius of the black hole). The subsequent radial motion of the matter to the black hole takes place through general-relativity effects, so that $W_{r\phi}(R_0) = 0$. Then, from (23) for $R \gg R_0$, we have

$$W_{r\phi} \approx -\frac{\dot{M}}{2\pi} \omega, \quad (24)$$

and, by the definition of $W_{r\phi}$ (21),

$$W_{r\phi} \approx 3\eta H \omega = \alpha PH. \quad (25)$$

Let us write the equation of energy balance. For the dust-filled layers near the central plane of the disk, we obtain

$$\frac{d}{dz}\lambda\frac{dT}{dz} - \eta R^2\left(\frac{d\omega}{dR}\right)^2 - \frac{L_x}{4\pi R^2}\zeta_\nu n_H + 4\pi l^2 n_d \sigma T_d^4 = 0, \quad (26)$$

where λ is the coefficient of heat conductivity for hydrogen, n_d is the dust number density, l is the grain radius, L_x is the luminosity of X-ray emission incident on the inner boundary of the maser disk, and ζ_ν is the frequency-dependent cross section of photoionization by X-ray emission [13].

The low-frequency part of the X-ray spectrum is absorbed most effectively by hydrogen at distances smaller than R down to the frequency determined from the condition $\tau_\nu = n_{H_2} \zeta_\nu R \sim 1$. Then, we rewrite equation (26) as

$$\frac{d}{dz}\lambda\frac{dT}{dz} - \frac{9}{4}\eta\omega^2 - \frac{L_x}{4\pi R^3} + 4\pi l^2 n_d \sigma T_d^4 = 0. \quad (27)$$

For the disk upper layers, the equation of energy balance takes the form

$$\frac{d}{dz}\lambda\frac{dT}{dz} - \frac{9}{4}\eta\omega^2 - \frac{L_x}{4\pi R^3} = 0. \quad (28)$$

Let us average equation (27) using relation (21):

$$\frac{d}{dz}\lambda\frac{dT}{dz} - \frac{3W_{r\phi}\omega}{4H} - \frac{L_x}{4\pi R^3} + 4\pi l^2 n_d \sigma T_d^4 = 0. \quad (29)$$

Given that $\lambda = 5/2\eta C_v = 5/6C_v\rho\alpha C_s H$ and that the speed of sound $C_s = \sqrt{\gamma kT/m_{H_2}}$ (m_{H_2} is the mass of the hydrogen molecule), we integrate equation (29) over the vertical z coordinate:

$$\frac{5}{18}C_v\alpha\Sigma\sqrt{\frac{\gamma k}{m_{H_2}}}\Delta T^{3/2} - \frac{3}{4}W_{r\phi}\omega\frac{z^2}{H} - \frac{L_x z^2}{4\pi R^3} + 4\pi\bar{n}_d l^2 \sigma T_d^4 z^2 = 0. \quad (30)$$

Assuming the dust surface density to be $2\bar{n}_d H = 0.01\Sigma/m_d$ (m_d is the mass of a single dust grain), we have the following relation for energy balance:

$$\frac{5}{18}C_v\alpha\Sigma\sqrt{\frac{\gamma k}{m_{H_2}}}\Delta T^{3/2} - \frac{3}{4}W_{r\phi}\omega\frac{z^2}{H} - \frac{L_x z^2}{4\pi R^3} + 0.02\pi l^2 \frac{\Sigma}{m_d H} \sigma T_d^4 z^2 = 0. \quad (31)$$

Similarly, for the dust-free layers of gas, we obtain

$$\frac{5}{18}C_v\alpha\Sigma\sqrt{\frac{\gamma k}{m_{H_2}}}\Delta T^{3/2} - \frac{3}{4}W_{r\phi}\omega\frac{z^2}{H} - \frac{L_x z^2}{4\pi R^3} = 0. \quad (32)$$

Let us introduce the following dimensionless parameters

$$r = \frac{R}{R_{\text{out}}}, \quad \xi = \frac{z}{H(r)}, \quad (33)$$

$$m = \frac{M}{4 \times 10^7 M_\odot}, \quad \dot{m} = \frac{\dot{M}}{10^{-4} M_\odot \text{ yr}^{-1}}.$$

Numerical simulations show that the dependence of gas temperature $T(r, \xi)$ at height H can be fitted by a second-degree polynomial,

$$T(r, 1) = T(1, 1)(1 + a(1-r) + b(1-r)^2), \quad (34)$$

where a and b are the polynomial coefficients. As a result, we obtain the following set of relations for the main disk parameters in the range $R_{\text{in}} \leq R \leq R_{\text{out}}$:

$$H = 1.1 \times 10^{15} (1 + a(1-r) + b(1-r)^2)^{1/2} m^{-1/2} r^{3/2} \text{ cm},$$

$$\Sigma = 3.7 \times 10 \alpha^{-1} (1 + a(1-r) + b(1-r)^2)^{-1} \dot{m} m^{1/2} r^{-3/2} \text{ g cm}^{-2},$$

$$V_\phi = 7.8 \times 10^7 m^{1/2} r^{-1/2} \text{ cm s}^{-1},$$

$$V_r = 1.2 \times 10^2 \alpha (1 + a(1-r) + b(1-r)^2) m^{-1/2} r^{1/2} \text{ cm s}^{-1}, \quad (35)$$

$$\rho = 1.7 \times 10^{-14} \alpha^{-1} (1 + a(1-r) + b(1-r)^2)^{-3/2} \dot{m} m r^{-3} \text{ g cm}^{-3},$$

$$P = 8.2 \times 10^{-5} \alpha^{-1} (1 + a(1-r) + b(1-r)^2)^{-1/2} \dot{m} m r^{-3} \text{ dyne cm}^{-2}.$$

The temperature profile $T(r, \xi)$ can be represented as

$$T = T(r, 0) \left(1 + \frac{\xi^2}{r^\delta} \left(0.63(1 + a(1-r) + b(1-r)^2)^{3/2} + \frac{(1 + a(1-r) + b(1-r)^2)^2}{100 \dot{m} m^{3/2} r^{-3/2}} \right) \right)^{2/3} \text{ K}, \quad (36)$$

where $T(r, 0) = T_d(r) = T_d^{\text{out}} r^{-\delta}$ (T_d^{out} is the dust temperature at the outer radius of the maser disk).

The best agreement between the observed profile of the maser emission and the calculations was achieved for the following model parameters: $M = 3.8 \times 10^7 M_\odot$; $\dot{M} = 10^{-4} M_\odot \text{ yr}^{-1}$; $\alpha = 0.2$; the radiation energy of the central source absorbed by the maser disk, $L_x = 10^{39} \text{ erg s}^{-1}$, for a total X-ray luminosity of the central source $4.1 \times 10^{40} \text{ erg s}^{-1}$ in the 3–10-keV band; the brightness temperature of the central source at $\sim 22 \text{ GHz}$ $T_R = 2 \times 10^6 \text{ K}$ [14]; the dust temperature $T_d(r) = T_d^{\text{out}} r^{-\delta} = 130 r^{-0.0625} \text{ K}$; and

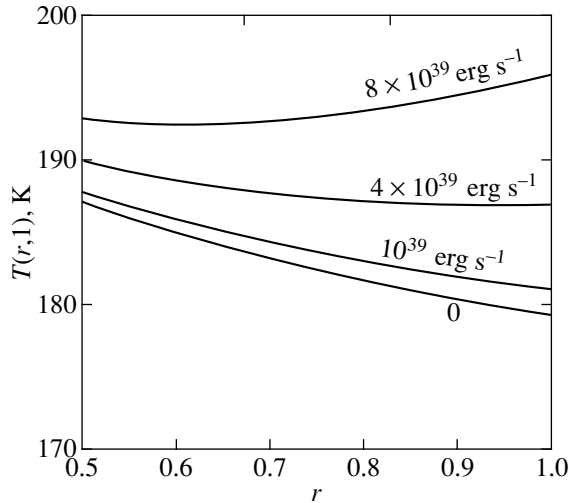


Fig. 4. Gas temperature at height $z = H$ versus distance $r = R/R_{\text{out}}$ for various X-ray luminosities L_x heating the maser disk.

the disk recession velocity 474 km s^{-1} . For these parameters, the coefficients in (34) are $a = 0.040$ and $b = 0.067$ (Fig. 4).

The dependence of maser-layer height H_{mas} on disk radius is shown in Fig. 5. Since the thickness of the maser layer is $\approx 10^{12} \text{ cm}$ and its height is $H_{\text{mas}} \sim H$, the layer temperature is $T_{\text{mas}} \approx T(r, 1)$.

Our model allows both the spectral line profile and the fluxes F_ν in various components to be obtained, which are in excellent agreement with observational data (Fig. 6), $F_\nu = I_\nu \pi \Theta^2$ ($\Theta = 4 \times 10^{-11} \text{ rad}$ is the effective size of the maser feature [2]).

PECULIARITIES OF THE STRUCTURE OF THE MASER LINE PROFILE

Since the radial component of the gas velocity in the disk is much smaller than its tangential component, the velocity field can be assumed to obey Kepler's law (1). According to Grinin and Grigor'ev [15], at each point R , there are two directions, s^+ and s^- , making angles θ_+ and θ_- with the extension of the radius vector \mathbf{R} , along which the velocity gradient is zero. In the case of a purely Keplerian velocity field in the disk plane, $\theta_+ = 0$ and $\theta_- = 90^\circ$.

Since relation (7) for the optical depth $\tau(R, \theta)$ contains an exponential velocity profile $\Phi_\nu(s)$, the exponent in (8) strongly affects the emission intensity and, consequently, the structure of the spectrum.

Let us expand the expression in (8) in a power series of s :

$$\frac{v - v_0(1 - V_s/c)}{\Delta v_D} = \frac{s}{V_t} \frac{dV_s}{ds} + \frac{s^2}{2V_t} \frac{d^2V_s}{ds^2} + \dots \quad (37)$$

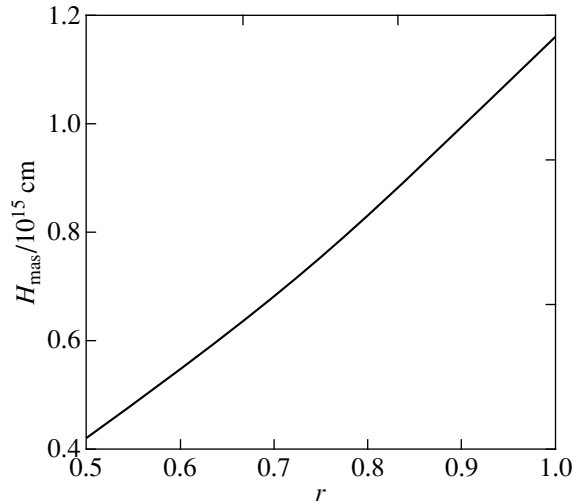


Fig. 5. Maser-layer height H_{mas} versus dimensionless radius $r = R/R_{\text{out}}$.

We then see from relation (37) that the coherent length s_0 is at a maximum in directions close to s^+ and s^- (s_0 is the distance at which the emission emerges from resonance, shifting by Δv_D). Since $\tau(R, \theta) \propto s_0(R, \theta)$,

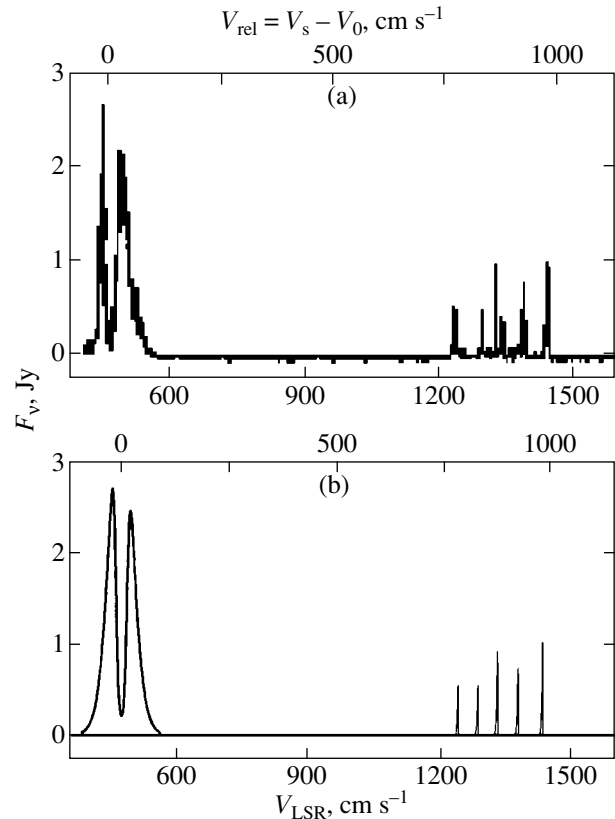


Fig. 6. The spectrum of H_2O maser emission from the nucleus of the galaxy NGC 4258: (a) results of the observations [6] (published with permission of the authors); (b) results of the numerical simulations (this study).

the maser emission intensity in the maser amplification mode peaks in these directions.

The coherent length at angles θ close to θ_+ is limited by the sizes of the maser disk; at other values of θ , s_0 is given by [15]

$$s_0(R, \theta) = s_{1/2}(R, \theta) + s_{1/2}(R, \theta + \pi), \quad (38)$$

where $s_{1/2}$ is the distance from the point \mathbf{R} at which the resonance-frequency shift is $\Delta v_D/2$. This distance can be determined from the equation

$$\left| \frac{s}{V_t} \frac{dV_s}{ds} + \frac{s^2}{2V_t} \frac{d^2V_s}{ds^2} + \dots \right| = \frac{1}{2}. \quad (39)$$

Figure 7 shows a plot of dimensionless coherent length $s_0/(R_{\text{out}} - R_{\text{in}})$ against angle θ with allowance for the first three terms of the V_s expansion in (37) for an absolutely flat disk and a line of sight parallel to the disk plane. This figure accounts for the observational fact that there are central and high-velocity components in the maser spectrum and no visible emission at intermediate velocities.

However, the disk plane may be curved by flexural waves. The hypothesis about the existence of such waves is based on the discrete regular structure of the high-velocity components in the maser spectrum, because flexural waves produce a continuous change in the inclination of the disk plane to the observer. Thus, it would be natural to assume that the line of sight lies in the disk plane for the high-velocity components in some directions; in this case, the coherent length of the ray path, $s_0 \approx 2 \times 10^{15}$ cm, is much smaller than the radius of curvature of the disk ($s_0 \ll R$).

It follows from observational data that the width of the high-velocity components is ~ 5 km s $^{-1}$. Numerical simulations show that such a broadening arises at $\theta \approx \theta_- + 3^\circ$ (or $\theta \approx \theta_- - 3^\circ$). This result also suggests that there are spiral flexural waves in the maser disk. Furthermore, the spiral pattern of flexural waves explains the asymmetry of the high-velocity components in the right and left parts of the spectrum.

According to observational data, the width of the central spectral component is $\delta\theta \approx 14^\circ$. If we assume the existence of flexural waves with ~ 3 crests in the segment between the inner and outer disk radii (which corresponds to five high-velocity maser peaks) and amplitude $A \geq (R_{\text{out}} - R_{\text{in}})/(10 \tan i_0)$, where i_0 is the inclination of the disk spin axis to the observer, $i_0 = 97^\circ \pm 4^\circ$, [7], then there will always be such a location of the ray for which the inclination of the disk plane to the observer is nearly zero. In this case, the coherent length of the ray path is $s_0 \ll (R_{\text{out}} - R_{\text{in}})/10$. Numerical simulations show that, for the above ray location and for the maser-layer thickness $h = 10^{12}$ cm, the inclination of the disk plane to the observer is $\approx 0.022^\circ$ ($s_0 \approx 2.6 \times 10^{15}$ cm).

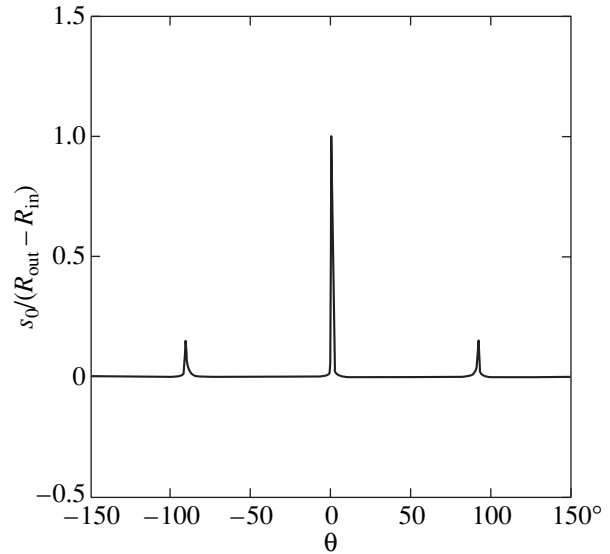


Fig. 7. Coherent length $s_0/(R_{\text{out}} - R_{\text{in}})$ versus angle θ .

The splitting of the central spectral component can be explained by the presence of an absorbing region containing H $_2$ O molecules on the line of sight. According our calculations, the optical depth τ of this region in the H $_2$ O line is 3, the turbulent velocity is 11 km s $^{-1}$, and the recession velocity is 476 km s $^{-1}$.

CONCLUSION

Based on our numerical calculations of the population kinetics of ortho-H $_2$ O molecular rotational levels with allowance for detailed data on the probabilities of radiative and collisional transitions between 30 lower rotational levels of ortho-H $_2$ O, we have elucidated the optimal conditions for the emergence of an inverse population of the signal $6_{16}-5_{23}$ levels and effective maser amplification of the $\lambda = 1.35$ cm line emission. The strong dependence of maser intensity on the number density and temperature of the H $_2$ buffer gas and H $_2$ O working molecules allowed us to determine, with a sufficiently high accuracy, the density and temperature profiles of the gas in the gas-dust accretion disk and the parameters of the medium in which the amplification takes place. Under the derived conditions, we elucidated the most probable mechanism of maser pumping in a molecular accretion disk differentially rotating around a black hole of mass $M = (4.0 \pm 0.25) \times 10^7 M_\odot$ ($D/7.3$ Mpc) at the accretion rate $\dot{M} = 10^{-4} M_\odot \text{ yr}^{-1}$ ($D/7.3$ Mpc) 2 .

By analyzing observational data, we determined the key model parameters: the radiation energy of the central source absorbed by the maser disk, $L_x = 10^{39}$ erg s $^{-1}$, turbulence parameter $\alpha \approx 0.2$, brightness temperature of the central source at ~ 22 GHz $T_R = 2 \times 10^6$ K, disk

recession velocity 474 km s^{-1} , and dust temperature $T_d = T_d^{\text{out}} r^{-\delta} = 130 r^{-0.0625} \text{ K}$.

Taking into account the spiral flexural waves in the disk, we calculated the multicomponent spectral-line profile; the derived absolute fluxes of individual line components are in good agreement with observational data.

ACKNOWLEDGMENTS

This study was supported by the Russian Foundation for Basic Research (project code 99-02-18232), the Russian Ministry of Education (project MO 021-00-2-02) and ESO CSEE (grant no. B-04-062).

REFERENCES

1. C. F. Gammie, R. Narayan, and R. Blandford, *Astrophys. J.* **516**, 177 (1999).
2. M. Miyoshi, J. Moran, J. Herrnstein, *et al.*, *Nature* **373**, 127 (1995).
3. G. Courtes, H. Petit, C. T. Hua, *et al.*, *Astron. Astrophys.* **268**, 419 (1993).
4. B. J. Wilkes, G. D. Schmidt, P. S. Smith, *et al.*, *Astrophys. J. Lett.* **455**, L13 (1995).
5. M. J. Claussen, G. M. Heiligman, and K. Y. Lo, *Nature* **310**, 298 (1984).
6. N. Nakai, M. Inoue, and M. Miyoshi, *Nature* **361**, 45 (1993).
7. J. Moran, L. Greenhill, P. Diamond, *et al.*, *Proc. Natl. Acad. Sci. USA* **92**, 1147 (1995).
8. G. Cecil, A. S. Wilson, and R. B. Tully, *Astrophys. J.* **390**, 365 (1992).
9. G. Piehler, D. A. Varshalovich, V. K. Khersonskii, *et al.*, *Astron. Astrophys., Suppl. Ser.* **76**, 195 (1988).
10. S. Chandra, D. A. Varshalovich, and W. H. Kegel, *Astron. Astrophys., Suppl. Ser.* **55**, 51 (1984).
11. N. I. Shakura and R. A. Sunyaev, *Astron. Astrophys.* **24**, 337 (1973).
12. L. D. Landau and E. M. Lifshitz, *Mechanics of Continuous Media* (Gostekhizdat, Moscow, 1953).
13. V. B. Berestetskii, E. M. Lifshitz, and L. P. Pitaevskii, *Quantum Electrodynamics* (Nauka, Moscow, 1980).
14. J. R. Herrnstein, L. J. Greenhill, J. M. Moran, *et al.*, *Astrophys. J. Lett.* **497**, L69 (1998).
15. V. P. Grinin and S. A. Grigor'ev, *Astron. Zh.* **60**, 512 (1983).

Translated by G. Rudnitskii

A Giant Bipolar Shell around the WO Star in the Galaxy IC 1613: Structure and Kinematics

V. L. Afanas'ev¹, T. A. Lozinskaya^{2*}, A. V. Moiseev¹, and E. Blanton³

¹ *Special Astrophysical Observatory, Russian Academy of Sciences, Nizhniĭ Arkhyz, Stavropolskiĭ kraĭ, 357147 Russia*

² *Sternberg Astronomical Institute, Universitetskiĭ pr. 13, Moscow, 119899 Russia*

³ *Columbia University, New York, USA*

Received May 10, 1999

Abstract—Observations of the nebula associated with the WO star in the galaxy IC 1613 are presented. The observations were carried out with a scanning Fabry–Perot interferometer in H α using the 6-m Special Astrophysical Observatory telescope; narrow-band H α and [O III] images were obtained with the 4-m KPNO telescope (USA). The monochromatic H α image clearly reveals a giant bipolar shell structure outside the bright nebula S3. The sizes of the southeastern and northwestern shells are 112×77 and $(186\text{--}192) \times (214\text{--}224)$ pc, respectively. We have studied the object's kinematics for the first time and found evidence for expansion of both shells. The expansion velocities of the southeastern and northwestern shells exceed 50 and 70 km s⁻¹, respectively. We revealed a filamentary structure of the shells and several compact features in the S3 core. A scenario is proposed for the formation of the giant bipolar structure by the stellar wind from the central WO star located at the boundary of a “supercavity” in the galaxy's H I distribution. © 2000 MAIK “Nauka/Interperiodica”.

Key words: *interstellar medium, stellar wind, WR stars*

1. INTRODUCTION

Among more than five hundred WR stars in the Local-Group galaxies, only six objects belong to a rare group of “oxygen” Wolf–Rayet (WO) stars. According to Barlow and Hummer [1], they can be considered as a separate sequence in the WN–WC–WO chain, which represents a very short final evolutionary stage of massive stars close to a bare CO core. The WO stars are characterized by a “superwind” (with a velocity up to 5000–6000 km s⁻¹; see [1–4]) preceded by the wind at the MS and WR stages. The WO effective temperature reaches 10⁵ K [3, 5–7].

Of the six WO stars in the Local-Group galaxies, three were identified in our Galaxy, one in the LMC, one in the SMC, and one in the irregular dwarf galaxy IC 1613; only two of them are associated with bright nebulae, including WO in IC 1613.

Our interest in the latter object also stems from the fact that WO is the only WR star identified in IC 1613, although the number of WO stars cannot exceed $\approx 1\%$ of the WR population because of their short lifetime.

D'Odorico and Rosa [8] and Davidson and Kinman [9] identified the WO star in IC 1613 by broad lines typical of this class of stars in the spectrum of the core of the bright emission nebula S3 [10]. The star's coordinates, RA(1950) = 1^h02^m27^s.3 and D(1950) = +01°48'17", are known with a 1" accuracy [11].

The central part of S3 is characterized by intense He II 4686 emission [8, 12, 13]. A detailed spectral analysis and

a discussion of the chemical composition of the bright nebula are presented in [13, 14]. Narrow-band H α images revealed regions of weaker emission predominantly southeast of the previously known bright, elongated nebula S3 [15, 16].

Thermal radio emission was detected from S3; the sizes of the radio source at half maximum intensity are 19" \times 14", and the radio image faithfully reproduces the shape of the bright optical nebula [17].

In this paper, we present our H α observations of the nebula with a Fabry–Perot interferometer on the 6-m Special Astrophysical Observatory (SAO) telescope, as well as narrow-band H α and [O III] images of the region obtained with the 4-m KPNO telescope.

For the first time, we have clearly revealed a weak outer bipolar shell structure far outside the bright nebula S3 and studied the kinematics of the object.

In Sect. 2, we provide basic parameters of the instruments and describe the observing and reduction techniques; the interferometric observations with the 6-m SAO telescope and the observations with the 4-m KPNO telescope are presented in Sect. 3. The origin of the unique bipolar shell structure of the nebula around the WO star is discussed in Sect. 4.

2. OBSERVATIONS AND DATA REDUCTION

2.1. Interferometric Observations

The interferometric H α observations were carried out with a scanning Fabry–Perot interferometer at the prime focus of the 6-m SAO telescope with a focal

* E-mail address for contacts: lozinsk@sai.msu.su

reducer (the equivalent focus is $F/2.4$). The interferometer is described in [18]. The pre-monochromatization was performed by using an interference filter with FWHM $\Delta\lambda = 15 \text{ \AA}$ centered on $H\alpha$ and tilted at an angle of $6^\circ 5'$.

We used a Fabry–Perot etalon operating in the 235th order at the $H\alpha$ wavelength; the separation between adjacent orders $\Delta\lambda = 27.9 \text{ \AA}$ corresponded to the 1274 km s^{-1} range free from order overlapping. The detector was a TK1024 1024×1024 -pixel CCD array. The observations were carried out with a 2×2 -pixel instrumental binning to reduce the readout time. We obtained 522×522 -pixel images in each spectral channel, with the pixel size corresponding to $0''.68$.

The size of the spectral channel was $\delta\lambda = 1.16 \text{ \AA}$ or 53 km s^{-1} in $H\alpha$. The actual instrumental profile of the interferometer was determined from night-sky lines (6568.8 , $6577.2/6577.4$, 6562.8 \AA , and $H\alpha$); the profile width was $\approx 3 \text{ \AA}$ or $\approx 140 \text{ km s}^{-1}$.

We performed the observations on August 31, 1998, at a 2.5 – $3''$ seeing at the zenith distance $z = 51^\circ$ – 54° . A total of 24 interferograms were obtained for various interferometer plate spacings. The time of a single exposure was 240 s.

The He I (6678.15 \AA) line of a calibration lamp was used for the phase shift measurement. After the observations, we made several accumulations of the images of the caps of the 6-m primary mirror uniformly illuminated by a lamp of continuous light. This allowed us to make a correction for nonuniform detector sensitivity (flat fielding) and simultaneously to adjust the filter passband.

The observational data were represented as $522 \times 522 \times 24$ -pixel “data cubes”; i.e., a 24-channel spectrum corresponded to each image element.

The data reduction (correction for the phase shift, subtraction of the night-sky spectrum, construction of the velocity field and the emission-line and continuum images) was carried out by using the ADHOC software package developed by Boulesteix [19].

Using star images from the Digital Palomar Sky Survey Atlas (DSS), we rotated the original images to coincide with the correct orientation ($\alpha - \delta$) and then averaged a 2×2 element, so that the resulting pixel size was $1''.34$.

To increase the signal-to-noise ratio, we performed an optimal filtration of the cube of observational data: spectral smoothing by Gaussians with FWHMs of 1.5 channels and spatial smoothing by Gaussians with FWHMs of the order of the seeing. After the smoothing, the resulting spatial resolution was $4''$.

Although the actual spectral resolution for the etalon in the 235th order of interference was 130 – 150 km s^{-1} in $H\alpha$, the accuracy of measuring the velocity from the line centroid (or from the Gaussian fit) in the case of a symmetric profile is considerably higher and is deter-

mined by the accuracy of phase calibration. The actual accuracy of a single measurement was checked by using a comparison spectrum and was 8 – 10 km s^{-1} .

The tie-in to the absolute velocity was checked by using night-sky lines. The possible systematic shift did not exceed 15 – 20 km s^{-1} .

2.2. Narrow-Band Images

The narrow-band $H\alpha$ and [O III] images of the nebula were obtained with the 4-m Kitt Peak National Observatory (KPNO) telescope. Interference filters centered on the $H\alpha$ ($\lambda = 6562 \text{ \AA}$, FWHM $\Delta\lambda = 29 \text{ \AA}$) and [O III] ($\lambda = 5009 \text{ \AA}$, $\Delta\lambda = 45 \text{ \AA}$) lines were used. The detector was a 2048×2048 -pixel CCD array with the pixel size corresponding to $0''.47$.

The observations were carried out on December 29 and 30, 1995; the angular resolution determined from star images was $1''.2$ in $H\alpha$ and $1''.4$ in [O III].

3. RESULTS OF THE OBSERVATIONS

3.1. Monochromatic $H\alpha$ Image

Figure 1 shows the monochromatic $H\alpha$ image of the region obtained by integrating the emission over all spectral channels of the line. For comparison, the image of the same region in continuum in the immediate vicinity of $H\alpha$ is indicated by isophotes; here, foreground stars in the field of view are clearly seen.

The absolute brightnesses were determined by comparison with the brightness from [15] for several nebular regions. Sources 37b, c, e, and g in the list of these authors were used for the flux calibration, i.e., the brightest and faintest regions were excluded.

Constructing the monochromatic image allowed us to clearly distinguish regions of weak $H\alpha$ emission from the background far outside the bright nebular core. As a result, we have been able for the first time to clearly show that these outer weak regions form a giant bipolar shell structure around the WO star and the bright S3 core. The two shells forming this bipolar structure are indicated by the dashed line in Fig. 1.

According to our measurements, the sizes of the three components (the bright core and the two outer shells) are the following: angular sizes of $26'' \times 20''$ or linear sizes of $83 \times 66 \text{ pc}$ for the bright nebula S3; $35'' \times 24''$ or $112 \times 77 \text{ pc}$ for the outer southeastern shell; and $(58$ – $60)'' \times (67$ – $70)''$ or $(186$ – $192) \times (214$ – $224) \text{ pc}$ for the outer northwestern shell.

We give the sizes along the major and minor axes of each structure for a distance of 660 kpc , as inferred by Saha *et al.* [20].

3.2. Narrow-Band $H\alpha$ and [O III] Images

Figure 2 shows the $H\alpha$ (Figs. 2a, 2b) and [O III] (Figs 2c, 2d) images of the nebula obtained with the

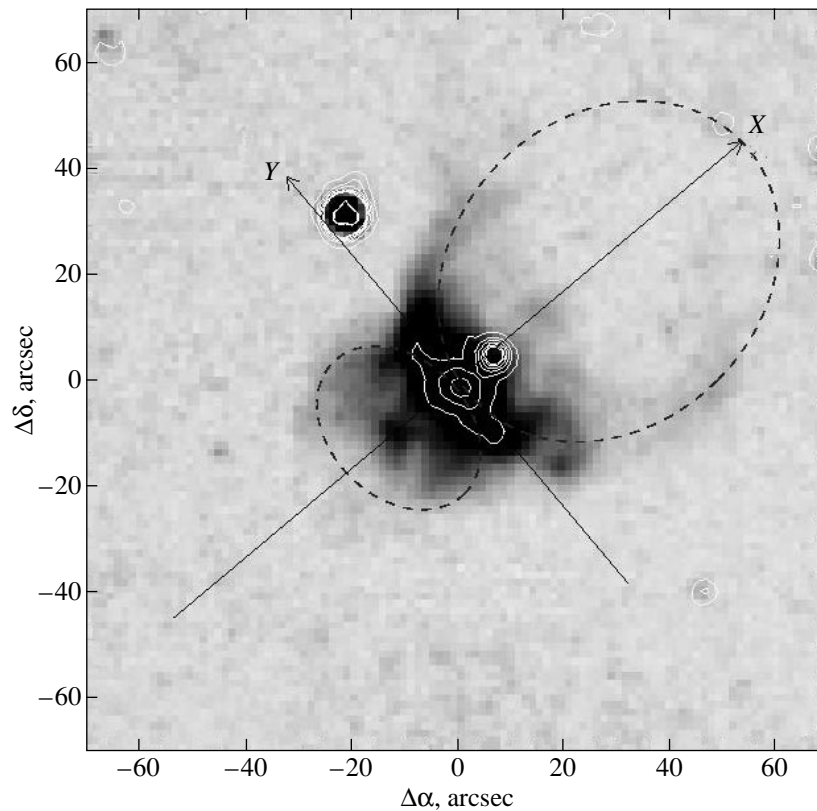


Fig. 1. The monochromatic $H\alpha$ image of the region obtained by integrating the emission over all spectral channels of the line. The image of the same region in continuum near $H\alpha$ is indicated by isophotes. The dashed line represents the giant bipolar shell.

4-m KPNO telescope. The southeastern outer shell and part of the northwestern shell at the very “base” near the bright nebular are seen in these figures. Both shells exhibit a distinct filamentary structure; in general, the filaments in the two lines are morphologically identical.

Three compact features unresolvable in the 6-m telescope monochromatic image because of the poor seeing on the observing night are clearly seen in the region of the bright S3 core. In all probability, the brightest of them (N1 in Fig. 2) is the WO star. The remaining features are most likely compact knots of gas, because, as follows from a comparison of Figs. 2b and 2d, their relative brightnesses in the two lines are different (N2 is brighter than N3 in $H\alpha$ and weaker than the latter in [O III]). To elucidate the nature of these compact sources requires spectroscopic observations at a sufficiently good seeing.

3.3. Kinematics

Figure 3 shows the measured velocities at the line peak and the line FWHMs as inferred from our Fabry–Perot interferometric observations. In the data reduction, the line was fitted by a Gaussian; the line width was corrected for the instrumental profile width by assuming that the latter was also Gaussian. In order to

find evidence for expansion of the outer bipolar shell, we constructed the distributions of line velocity and FWHM along two cuts designated, respectively, X and Y in Fig. 1. The band along the X axis is 60'' wide, so the entire bipolar structure falls within it; the (15'' wide) band along the Y axis covers predominantly the bright central S3 core and, in part, the weaker emission at the bases of the two outer shells.

A comparison of the line velocities and FWHMs along the two cuts leads us to the following conclusions:

(1) The scatter of velocities of the line peak is systematically larger in both outer shells than that in the central bright S3 core. Indeed, the velocities in the central region ($-10'' \dots +10''$) along the X axis in Fig. 1 vary in the range from -190 to -255 km s^{-1} ; the velocities in the southeastern shell vary in the range from -165 to -295 km s^{-1} ; and the range of velocities in the extended northwestern shell is largest: from -150 to -300 km s^{-1} .

As we see from the cut along the Y axis in Fig. 3b, the scatter of velocities in the bright S3 core is even smaller: velocities from -200 to -230 km s^{-1} are observed in a band within $\pm 13''$ of the center (in accordance with the core size; see Fig. 1). At larger distances from the center, the scatter increases because of the

contribution of emission from the bases of both outer shells.

(2) The line width in both shells also exceeds appreciably the line width in the central core. As we see from Fig. 3c, the line width in the same central region ($\pm 10''$) is no larger than 240 km s^{-1} ; in the southeastern shell, it reaches 330 km s^{-1} ; and the broadest line up to 390 km s^{-1} is observed in the northwestern shell.

The two observed patterns of behavior suggest the presence of systematic high-velocity motions in the outer bipolar shell structure. Based on these data, we may take an expansion velocity $\geq 50 \text{ km s}^{-1}$ for the southeastern shell and $\geq 70 \text{ km s}^{-1}$ for the northwestern shell as a rough estimate. The two values are a lower limit; the underestimate can be more significant for the northwestern shell, because here we observe mainly the emission from the periphery, where the effect of geometrical projection reduces the observed radial velocities.

Evidently, observations with a higher spectral and angular resolution are desirable to accurately estimate the expansion velocity. It should be borne in mind, however, that such an “erratic” velocity distribution—from slow bright knots to the most rapid weak features—is observed in most expanding supernova remnants and nebulae around the sources of strong stellar wind, which were studied with a high angular and spectral resolution [21, 22]. Indeed, the nebulae are irregular in shape and clumpy in structure; accordingly, the effect of geometrical projection changes erratically the observed radial velocity. During the passage of a shock wave, the gas of dense bright knots accelerates weakly, while the gas of lower density accelerates more strongly. For these reasons, the entire set of radial velocities, ranging from the gas at rest to the shock velocity, is commonly observed in real expanding shells. Higher resolution observations of the nebula around the WO star in IC 1613 could therefore reveal the same erratic distribution of line velocities and FWHMs.

According to our measurements, the mean velocity of the bright part of the nebula, where the expansion effect is marginal, is $V(\text{HeI}) = -216 \pm 1 \text{ km s}^{-1}$. Given a possible systematic tie-in error of the absolute velocity measurements within $15\text{--}20 \text{ km s}^{-1}$ (see Sect. 2), this value is in agreement with the measurements by Tomita [23] $V(\text{HeI}) = -235 \dots -230 \text{ km s}^{-1}$, as inferred from one spectrogram of S3, and with the measurements by Lake and Skillman [24] in the 21-cm radio line: the mean velocity $V(\text{HeI}) = -232 \text{ km s}^{-1}$ in the near galactic region.

4. DISCUSSION

The existence of an outer bipolar structure outside the bright core of the nebula S3 in IC 1613 was first suspected by one of us (T.A.L.) back in 1988 on the basis of trial narrow-band [O III] images obtained by

M.A. Dopita at her request with the 2.6-m MSSS ANU telescope, which have not been published. This suspicion was completely confirmed in this study.

Lozinskaya [25] suggested the break of a strong stellar wind in two directions out of the dense gas layer forming the “main body” of the nebula, as a possible explanation for the bipolar structure of the outer shells. Not only the morphology of the nebula, but also its orientation relative to the extended region of H I deficiency, which is clearly seen in the distribution of the 21-cm H I line emission obtained by Lake and Skillman [24], argue for this model. The center of this “supercavity” in the H I distribution has the following coordinates: $\text{RA} = 1^{\text{h}}2^{\text{m}}20^{\text{s}}$ and $\text{D} = 10^{\circ}51'$; its size is $2'\text{--}3'$ ($40\text{--}600 \text{ pc}$). The formation of such a supercavity may be associated with the preceding activity of stars in the region. If the H I deficiency is assumed to be caused by the sweeping up of gas, then the orientation of the nebula’s main body along the boundary of the hypothetical swept-up H I “supershell”, the southeastern shell in the region of a denser medium, and the extended weak northwestern shell in the medium of lower density inside the supercavity, can be explained naturally.

The bipolar shell structure associated with the WO star in IC 1613 and its location relative to the H I supercavity are schematically shown in Fig. 4.

The analogy with an extensively studied galactic object also argues for the break out of a strong stellar wind into the region of reduced gas density: the bright shell swept up by the wind in a dense cloud and the “blister” produced by the wind burst through the cloud into a tenuous medium are also observed in the nebula G2.4+1.4 associated with the star of the same type, WR 102 [3, 26].

An analysis of the parameters of the two shells associated with the WO star in IC 1613 yields the rough estimates that are in best agreement with the standard model of wind effect on the interstellar medium. The size of both shells ($R_1 \approx 56 \text{ pc}$ and $R_2 \approx 110 \text{ pc}$) is actually the only parameter that was reliably determined from observations. However, the fact that the ages of the two shells must be the same in the proposed model constrains significantly the range of possible values for the parameters.

The wind mechanical luminosity for the WO star in IC 1613 is $L_w \approx 10^{38} \text{ erg s}^{-1}$ [14]. This estimate is rather crude, because only the wind velocity ($V_w = 2850 \text{ km s}^{-1}$) was determined from observations, while the mass-loss rate ($2.9 \times 10^{-5} M_{\odot} \text{ yr}^{-1}$) was estimated indirectly from the relation between the He II-line luminosity and the outflow rate for two WO stars.

The typical density of the interstellar medium in the vicinity of the star can be estimated with the same uncertainty.

First, based on the $\text{H}\beta$ emission from the brightest central part of S3 $6''$ in size, Davidson and Kinman [9] found the core density to be $N_e = 8.5 \text{ cm}^{-3}$. Second,

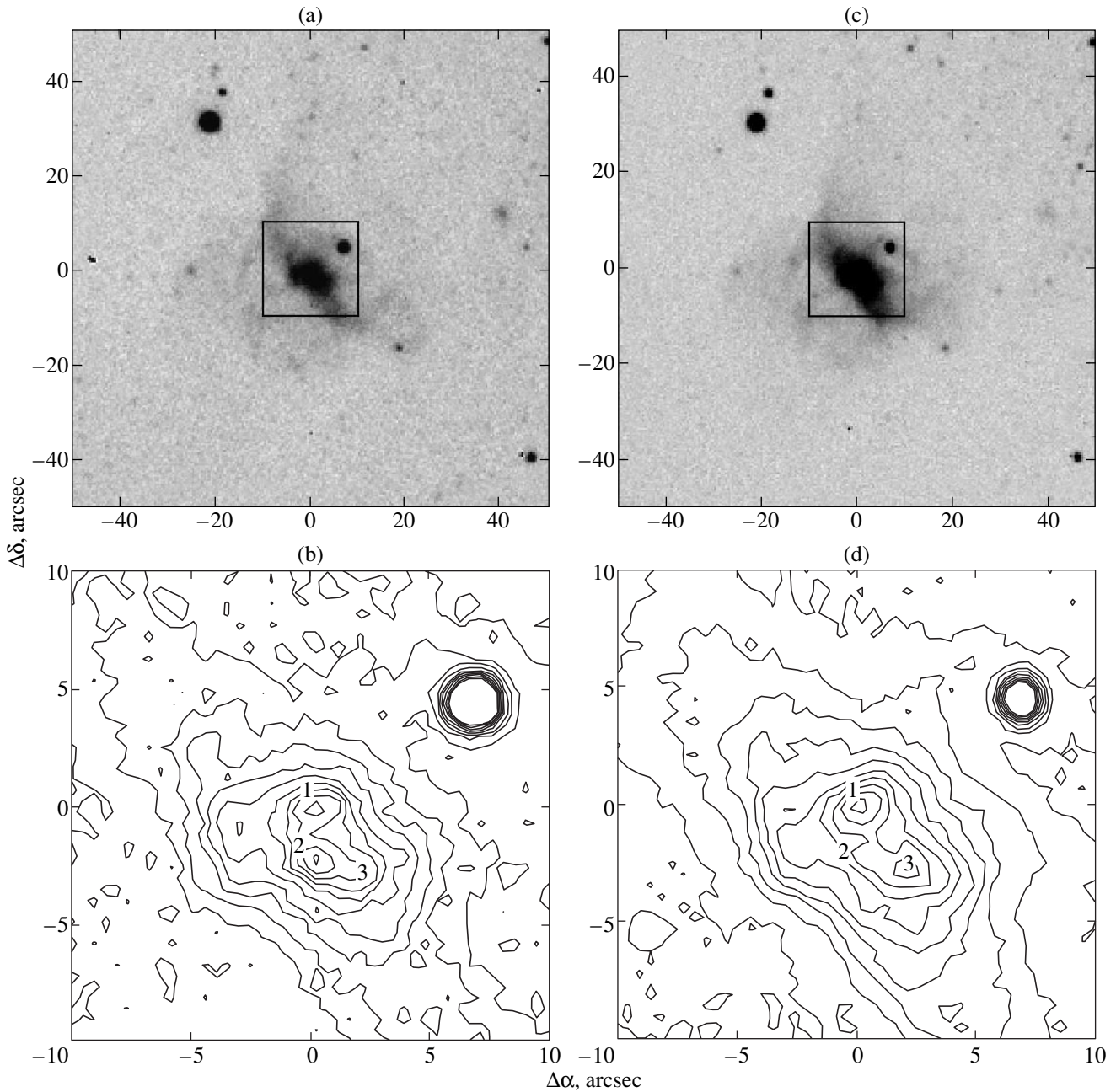


Fig. 2. The narrow-band H α (a, b) and [O III] (c, d) images of the nebula obtained with the 4-m KPNO telescope. The numbers denote three compact sources; source 1 is most likely the WO star. The square encloses the region whose isophotes are shown below.

using the total H α emission from the entire bright nebula, Kennicutt [27] obtained a mean $N_e \approx 1 \text{ cm}^{-3}$. Third, Goss and Lozinskaya [17] estimated the mean density in the bright nebula S3 from the flux density of thermal radio emission to be $N_e = 3.5 \text{ cm}^{-3}$.

Given the dense knots that we detected in the central core, all three estimates give a lower limit on the density in the bright nebula. These estimates refer to the densest region of the central nebula, where, judging by the radial-velocity field presented above, the gas was

not accelerated by the stellar wind because of the high density.

The mean ambient gas density in a large region around the WO star can be obtained from the 21-cm observations by Lake and Skillman [24]. Their map of the H I column-density distribution gives $N(\text{HI}) \approx (2-4) \times 10^{20} \text{ cm}^{-2}$ for the region of interest. For a thickness of the galactic gas disk of 500–800 pc, this value corresponds to a mean density of $\approx 0.1 \text{ cm}^{-3}$. We estimated the gas-disk thickness from the following considerations. According to the optical B surface-brightness

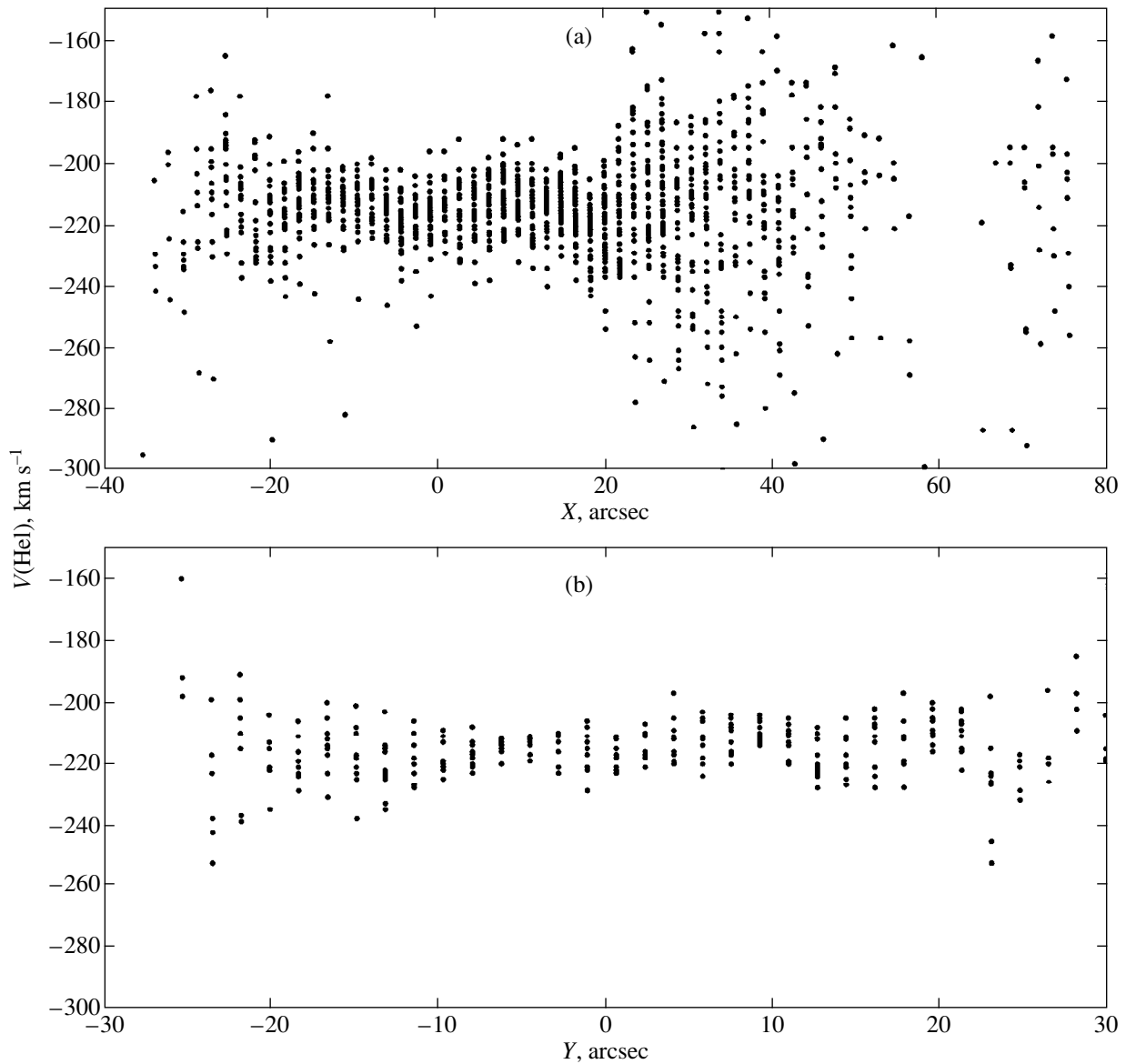


Fig. 3. The measured velocity at line peak and the line FWHMs as inferred from our Fabry–Perot interferometric observations: (a) $V(\text{Hel})$ in a $60''$ wide band along the X axis (see Fig. 1); (b) $V(\text{Hel})$ in a $15''$ wide band along the Y axis; (c) and (d) the line FWHMs in the same bands along the X and Y axes, respectively.

profile given in the above paper, the stellar surface density at a distance $R \approx 6'$ from the center is $\sigma_* \approx 2.5\text{--}3 M_\odot \text{ pc}^{-2}$, while the total surface density of stars and gas is $\sigma_T \approx 3.5\text{--}4 M_\odot \text{ pc}^{-2}$. The thickness of the gas disk can be roughly assumed to be $h_0 \sim 1/\sqrt{\sigma_T}$ (see, e.g., [28]). Since $\sigma_T \approx 50\text{--}70 M_\odot \text{ pc}^{-2}$ at a gas-disk thickness of $\approx 200 \text{ pc}$ in the solar neighborhood, we obtain $h_0 \approx 500\text{--}800 \text{ pc}$ in the WO region for IC 1613.

All these estimates are rather crude, but they show that the initial density in the vicinity of the WO star is unlikely to fall outside the range from 0.01 to 5 cm^{-3} .

The expected ages (in units of 10^6 years) and expansion velocities for the two outer shells in the standard

model of a wind-blown bubble [29, 30] are given in the table for various initial densities n_0 at $L_w = 10^{38} \text{ erg s}^{-1}$ and $R_1 \approx 56 \text{ pc}$ and $R_2 \approx 110 \text{ pc}$ derived above.

As we see from the table, similar age estimates for the two shells, depending on the radius, provided that the expected expansion velocity is close to the observed values $v_1 \geq 50 \text{ km s}^{-1}$ and $v_2 \geq 70 \text{ km s}^{-1}$, are obtained at an initial gas density $n_0 \approx 1\text{--}0.1 \text{ cm}^{-3}$ for the brighter southeastern shell and $n_0 \approx 0.1\text{--}0.01 \text{ cm}^{-3}$ for the weaker extended northwestern shell. These ranges of ambient gas densities seem quite reasonable. The ratio of ambient gas densities in the two shells swept up by the wind is determined from the ratio of their sizes

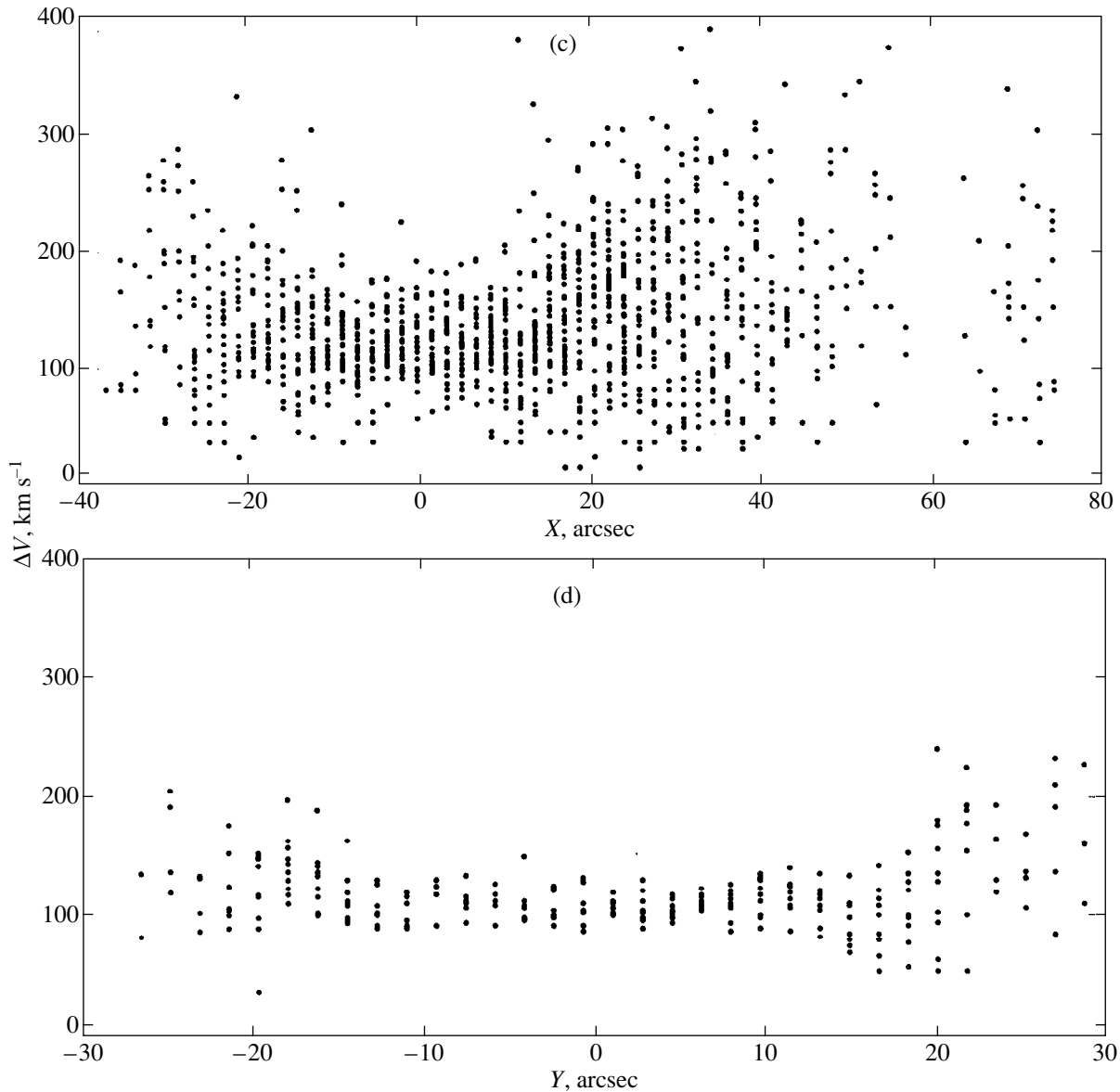


Fig. 3. (Contd.)

more accurately than the density itself: $n_{0,1}/n_{0,2} = (R_2/R_1)^5 \approx 20$.

The inferred age of the bipolar shell structure, $t_1 \approx (0.3-1) \times 10^6$ years, is close to the lifetime of a massive WR star and exceeds appreciably the duration of the final WO stage. Note that the age was estimated for the WO wind intensity. The wind intensity at the preceding WR stage was most likely lower, which increases still further the age estimate for the shell. Thus, we conclude that the unique bipolar structure was most likely produced by the wind from the central star at the stage preceding WO. The WO superwind, which switches on inside the previously formed structure, is an additional source of energy. Since the shock wave triggered by the strong WO wind propagates in a medium of very low density inside the existing bipolar shells, the “second-

ary” shells swept up by them rapidly reach the denser regions at the boundary. The additional compression of gas by the shock wave triggered by the superwind gives rise to a filamentary structure, which is clearly seen in Figs. 3a and 3b in the southeastern shell and at the base of the northwestern shell.

The expected ages and expansion velocities of the two outer shells in a medium of various densities

n_0, cm^{-3}	5	1	0.1	0.01	0.001
$t(R_1), 10^6 \text{ years}$	1.2	0.7	0.3	0.15	0.07
$v_1, \text{km s}^{-1}$	28	46	100	218	460
$t(R_2), 10^6 \text{ years}$	3.6	2.1	1.0	0.45	0.2
$v_2, \text{km s}^{-1}$	18	30	63	140	300

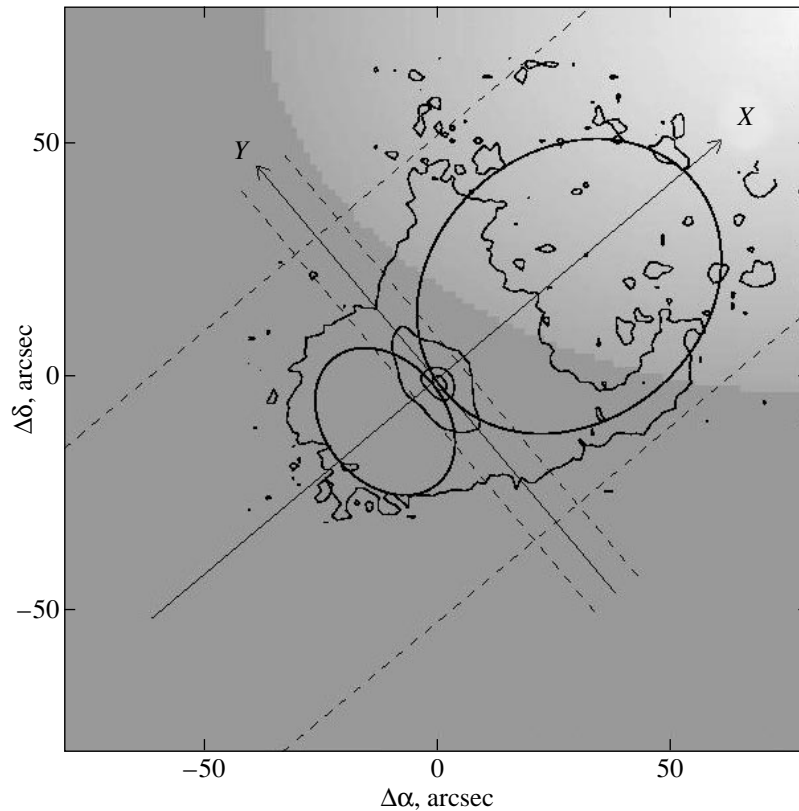


Fig. 4. A scheme for the bipolar shell structure associated with the WO star and its location relative to the H I supercavity. The bipolar shell is represented by two ellipses. The dashed lines indicate the boundaries of the cuts along the X and Y axes (see Fig. 3). The H α isophotes as constructed from the 6-m telescope observations correspond to 0.025 , 0.4 , and 1.0×10^{-15} erg cm $^{-2}$ s $^{-1}$ arcsec $^{-2}$. The shades of gray indicate the distribution of H I column density (the fit to the data from [24]). The transition from white to gray corresponds to column densities from 0.4 to 2×10^{20} cm $^{-2}$.

5. CONCLUSION

Our H α observations of the nebula associated with the WO star in the galaxy IC 1613 using a scanning Fabry–Perot interferometer on the 6-m SAO telescope clearly revealed a giant bipolar shell structure outside the bright nebula S3. The sizes of the shell southeast of the bright nebula are 112×77 pc; the northwestern shell is twice as large: $(186\text{--}192) \times (214\text{--}224)$ pc. The object’s kinematics has been studied for the first time. We found evidence for expansion of both shells; the possible expansion velocities of the southeastern and northwestern shells are no less than 50 and 70 km s $^{-1}$, respectively. Using the 4-m KPNO telescope (narrow-band H α and [O III] images), we detected a filamentary structure of both shells and several compact features in the S3 core.

We propose a self-consistent model for the formation of the giant bipolar structure by the wind from the central WO star located at the boundary of a supercavity in the galactic H I distribution.

ACKNOWLEDGMENTS

This study was supported by the Russian Foundation for Basic Research (project no. 98-02-16032) and

the Program “Astronomy” (project no. 1.3.1.2). We wish to thank M. Dopita, who provided unpublished [O III] images of the region, J. Boulesteix for the opportunity to use interference filters, and the 6-m SAO telescope committee for allocating observing time.

REFERENCES

1. M. J. Barlow and D. C. Hummer, *Wolf–Rayet Stars: Observations, Physics, and Evolution*, IAU Symp. 99, Ed. by C. W. H. de Loore and A. J. Willis (Reidel, Dordrecht, 1982), p. 387.
2. A. V. Torres, P. S. Conti, and P. Massey, *Astrophys. J.* **300**, 379 (1986).
3. M. A. Dopita, P. J. McGregor, T. A. Lozinskaya, *et al.*, *Astrophys. J.* **351**, 563 (1990).
4. V. F. Polcaro, R. Viotti, C. Rossi, *et al.*, *Astron. Astrophys.* **265**, 563 (1992).
5. A. Maeder and G. Meynet, *Astron. Astrophys.* **210**, 155 (1989).
6. J. Melnik and M. Heydari-Malayeri, *WR Stars and Interrelations with Other Massive Stars in Galaxies*, IAU Symp. 143, Ed. by K. A. Van der Hucht and B. Hidayat (Kluwer, Dordrecht, 1991), p. 409.
7. V. F. Polcaro, F. Giovanelli, R. K. Manchanda, *et al.*, *Astron. Astrophys.* **252**, 590 (1991).

8. S. D'Odorico and M. Rosa, *Astron. Astrophys.* **105**, 410 (1982).
9. K. Davidson and T. D. Kinman, *Publ. Astron. Soc. Pacif.* **94**, 634 (1982).
10. A. R. Sandage, *Astrophys. J.* **166**, 13 (1971).
11. T. E. Armandroff and P. Massey, *Astrophys. J.* **291**, 685 (1985).
12. H. E. Smith, *Astrophys. J.* **199**, 591 (1975).
13. D. R. Garnett, R. C. Kennicutt, Y.- H. Chu, *et al.*, *Astrophys. J.* **373**, 458 (1991).
14. R. L. Kinsburgh and M. J. Barlow, *Astron. Astrophys.* **295**, 171 (1995).
15. P. Hodge, M. G. Lee, and M. Gurwell, *Publ. Astron. Soc. Pacif.* **102**, 1245 (1990).
16. D. A. Hunter, W. N. Hawley, and J. S. Gallagher, *Astron. J.* **106**, 1797 (1993).
17. W. M. Goss and T. A. Lozinskaya, *Astrophys. J.* **439**, 637 (1995).
18. S. N. Dodonov, V. V. Vlasyuk, and S. V. Drabek, *Fabry-Perot Interferometer. User's Guide* (Special Astrofiz. Obs., Nizhniĭ Arkhyz, 1995).
19. J. Boulesteix, *ADHOC Reference Manual* (Observatoire de Marseille, Marseille, 1993).
20. A. Saha, W. L. Freedman, J. G. Hoessel, *et al.*, *Astron. J.* **104**, 1072 (1992).
21. T. A. Lozinskaya, *Supernovae and Stellar Wind: Interaction with Galactic Gas* (Nauka, Moscow, 1986).
22. T. A. Lozinskaya, *Supernovae and Stellar Wind in the Interstellar Medium* (AIP, New York, 1992).
23. A. Tomita, K. Ohta, and M. Saita, *Publ. Astron. Soc. Jpn.* **45**, 693 (1993).
24. G. Lake and E. D. Skillman, *Astron. J.* **98**, 1274 (1989).
25. T. A. Lozinskaya, *Astrophys. Space Sci.* **252**, 199 (1997).
26. M. A. Dopita and T. A. Lozinskaya, *Astrophys. J.* **359**, 419 (1990).
27. R. C. Kennicutt, *Astrophys. J.* **287**, 116 (1984).
28. A. V. Zasov, *Physics of Galaxies* (MGU, Moscow, 1993).
29. J. Castor, R. McCray, and R. Weaver, *Astrophys. J. Lett.* **200**, L107 (1975).
30. R. Weaver, R. McCray, J. Castor, *et al.*, *Astrophys. J.* **218**, 377 (1977).

Translated by V. Astakhov

Evolution of the Symbiotic Star AS 338 after Its Strong Outburst in 1983

V. F. Esipov^{1*}, E. A. Kolotilov¹, J. Mikolajewska², U. Munari³, A. A. Tatarnikova¹,
A. M. Tatarnikov¹, T. Tomov⁴, and B. F. Yudin¹

¹ Sternberg Astronomical Institute, Universitetskii pr. 13, Moscow, 119899 Russia

² N. Copernicus Astronomical Center, Warsaw, Poland

³ Padoa Astronomical Observatory, Asiago, Italy

⁴ National Astronomical Observatory, Smolyan, Bulgaria

Received April 15, 1999

Abstract—The photometric *UBV* observations of AS 338 that we began after its outburst in 1983 are presented. They were accompanied by yearly spectroscopic observations and by occasional estimations of the star's infrared *JHKL* magnitudes. In June 1993, the star's optical spectrum was extended to the ultraviolet via IUE observations of AS 338. Collectively, the above observations make it possible to trace the evolution of stellar activity over a period of 15 years in various spectral ranges. In particular, a short-time return of the hot component of AS 338 to the state when He II lines reappeared in the star's spectrum was noted in 1993. At this time, a blend of the C IV $\lambda\lambda$ 5802 and 5812 lines, which is typical of Wolf-Rayet spectra, was detected in it. In June 1993, the temperature of the hot component was $T_h \approx 8.8 \times 10^4$ K, and the ratio of its bolometric flux to that of the red giant was $F_{h, \text{bol}}/F_{g, \text{bol}} \approx 1.0$. In August, its temperature increased to $\sim 1.0 \times 10^5$ K, while the bolometric flux dropped by a factor of ~ 1.5 ($F_{h, \text{bol}}/F_{g, \text{bol}} \approx 0.7$). In the *B–V*, *U* diagram, the points referring to this so-called quiescent state form a separate group shifted in *B–V* from all the remaining ones located in a horizontal strip with $\Delta U \approx 3^m.5$ and $\Delta(B–V) \approx 0^m.4$. This allows us to diagnose the state of the hot component without spectroscopic observations of the star. In October 1993, the hot component flared up again. The main brightness rise took no more than 19 days. The outburst occurred shortly before eclipse egress of the hot component, whose duration was $\sim 0.01 P_{\text{orb}}$. In December 1993, $F_{h, \text{bol}}/F_{g, \text{bol}} \leq 1.5$ at maximum light. During the recurrent, even stronger outburst in April 1995, $F_{h, \text{bol}}/F_{g, \text{bol}} \leq 3.4$. The H α line during outbursts has a P Cyg profile and broad wings stretching to velocities of ± 1500 km s^{–1}. The color temperature of the active hot component at short optical wavelengths and in the ultraviolet lies in the range of effective temperatures for hot supergiants. Nevertheless, it always produces an H II region in the circumstellar envelope that is larger in size than this binary system. © 2000 MAIK “Nauka/Interperiodica”.

Key words: *symbiotic stars*

INTRODUCTION

AS 338 (\equiv MH α 305–6) was discovered by Merrill and Burwell [1] as a star with a strong H α emission line. It was included in the catalog of symbiotic stars by Allen [2]. Having obtained the spectrum of AS 338 in 1978, he detected a large set of emission lines along with strong TiO molecular absorption bands. In other words, the spectrum was clearly a combination one, and, by definition, AS 338 had every reason to be included in the group of symbiotic stars. It should be noted that, apart from H I and He I lines, the spectrum exhibited a strong He II λ 4686 line, suggesting a high temperature ($\sim 10^5$ K) of the hot component in this symbiotic binary system.

The spectroscopic and photometric observations of AS 338 by Schulte-Ladbeck [3] in 1983–1984 showed

that the star became considerably brighter than before, and that both He II λ 4686 and TiO absorption bands vanished from its spectrum. Thus, the next close look at AS 338 coincided with its strong outburst. Photometric and spectroscopic observations of AS 338 (see [4] and references therein) showed that, until 1992, the star had never returned to the state in which it was caught by Allen in 1978. Munari [4] noticed several deep minima repeating with period $P = 434^d$ in the overall *V* light curve of AS 338. He associated them with an eclipse of the hot component by the red giant of this binary system.

In June 1993, the AS 338 spectrum again exhibited He II λ 4686, which disappeared in November of the same year [5]. Its disappearance was accompanied by a brightening of the star. The next brightening episode of AS 338 was reported in 1995 [6, 7].

In this paper, we present the photometric *UBV* observations of AS 338 that we started in 1983. They were accompanied by yearly spectroscopic observa-

* E-mail address for contacts: esipov@sai.msu.ru

tions and by occasional estimations of the star's infrared *JHKL* magnitudes. Collectively, they make it possible to trace the evolution of stellar activity over a period of 15 years in various spectral ranges, in particular, its short-time return to the state when He II lines reappeared in the star's spectrum and its two succeeding outbursts. Note that only a few multicolor magnitude estimates for the star have been published to date. In addition, our observations cover several eclipsing episodes of the hot component. In general, however, they allow us to estimate the physical parameters of the above phenomena and to get a general idea of the symbiotic star AS 338 as a representative of a rather heterogeneous class of objects, each of which requires a separate study.

OBSERVATIONS

The photometric *UBV* observations of AS 338 were carried out with the 0.6-m telescope at the Crimean Station of the Sternberg Astronomical Institute (SAI). The standard star was HD 179588: $U = 6.44$, $B = 6.72$, and $V = 6.73$. The observational errors did not exceed $0^m.03$. Their results are given in Table 1. Photographic *B* magnitude estimates for AS 338 were obtained from SAI library plates [8]. Their accuracy is no lower than $0^m.1$. They are given in Table 2.

Figure 1 shows *U*, *B* light curves and *U-B*, *B-V* color curves of the star. Figure 2 shows the *B* light curve folded by using the ephemeris

$$\text{Min}(V) = 2447087 + 434^d.1E,$$

from [4]. Phase $\phi = 0$ corresponds to minimum light of the hot component. The dates of minima are also marked by vertical bars above the *B* light curve of the star (Fig. 1). Note that Fig. 2 also plots those magnitude estimates for AS 338 which were obtained before 1983 and which, accordingly, are not shown in Fig. 1. The photographic minimum light of the star can be judged by these estimates. Figure 3 shows color-magnitude diagrams: (*U-B*), *U* and (*B-V*), *U*.

The photometric *JHKL* observations of AS 338 were performed with the 1.25-m telescope at the Crimean station of the SAI. The standard star was BS 7176: $J = 2.33$, $H = 1.82$, $K = 1.69$, and $L = 1.55$. The observational errors did not exceed $0^m.03$ in *JHK* and $0^m.1$ in *L*. The observations are summarized in Table 3.

Starting in 1984, yearly spectroscopic observations of AS 338 have also been carried out with this telescope in the wavelength range 4000–7000 Å with ~ 5 Å resolution. The detector in the spectrograph has been a SBIG SN-61 CCD array since 1995. The observations before 1988 were published by Esipov *et al.* [9].

In addition, low- and high-resolution spectroscopic observations of AS 338 are being performed with the 1.82-m telescope at the Padoa Astronomical Observatory located at the summit of Mount Ecar in Asiago

(Italy). The Boller&Chivens low-resolution spectrograph uses a TH7882 580×388 CCD array as the detector. It takes spectra in the wavelength range 3300–11000 Å with ~ 8 Å resolution. The echelle spectrograph with crossed gratings takes spectra in the wavelength range 4000–7000 Å with ~ 0.3 Å resolution. The detector is a THX31156 1024×1024 CCD array. The low-resolution spectroscopic observations before 1992 were published by Munari [4]. In Fig. 1, the vertical bars above the *U* light curve of the star mark the dates of all our low-resolution spectroscopic observations. Figure 4 shows the spectra of AS 338 obtained in 1993 before (August 25, $\phi \approx 0.93$), during (September 20, $\phi \approx 0.99$), and after (December 16, $\phi \approx 0.19$) eclipse of the hot component. The first two spectra refer to the star's state when the hot component excited the He II $\lambda 4686$ line in the circumstellar envelope, and the last one refers to the maximum of 1993 outburst when this line disappeared because of an appreciable decrease in the hot-component temperature.

Below, the first and second states are called quiescent (the star's visual brightness at this time is close to its minimum) and active, respectively. In order not to repeat once more in which state the star was at a given time, we note that the transition from quiescent state to active one occurred late in September 1993 shortly before eclipse egress of the hot component of AS 338. The Asiago low-resolution spectra, which cover the transition of AS 338 from active state to quiescent one and back (October 1992–February 1994), were calibrated, and spectral-line fluxes are given in Table 4. The errors in their estimates for the weakest lines do not exceed 20% and are mainly attributable to complex continuum variations in their formation region. In those cases where a line was seen but its flux was difficult to measure, it is marked by "Y" in Table 4; otherwise (if it was unseen), it is marked by "N".

Figure 5 shows H α profiles in the high-resolution spectra before and after eclipse. In quiescent state of the hot component, the AS 338 spectrum exhibited an intense [O III] $\lambda 5007$ line, which is shown in Fig. 5 (lower panel) together with H α . In this case, however, the exposure was too short to reach the continuum level, and the recorded signal is essentially laid off along the *y* axis. The meaning of the lower panel in Fig. 5 is to clearly show how the H α line is deformed relative to the fairly symmetric and appreciably narrower [O III] line, which originates in outer layers of the circumstellar envelope around AS 338 and undergoes no self-absorption.

In active state of the hot component, the continuum near H α is clearly distinguished, and the line intensity normalized to the continuum is laid off along the *y* axis. Our high-resolution spectra for active state exhibit neither [O III] $\lambda 5007$ nor He I $\lambda 5016$, apparently because of insufficient exposure in this spectral range. This is confirmed by the presence of an emission feature near a wavelength of 5010 Å in the low-resolution spectra (Fig. 4). In our case, it is a blend of [O III] $\lambda 5007$ and He I $\lambda 5016$.

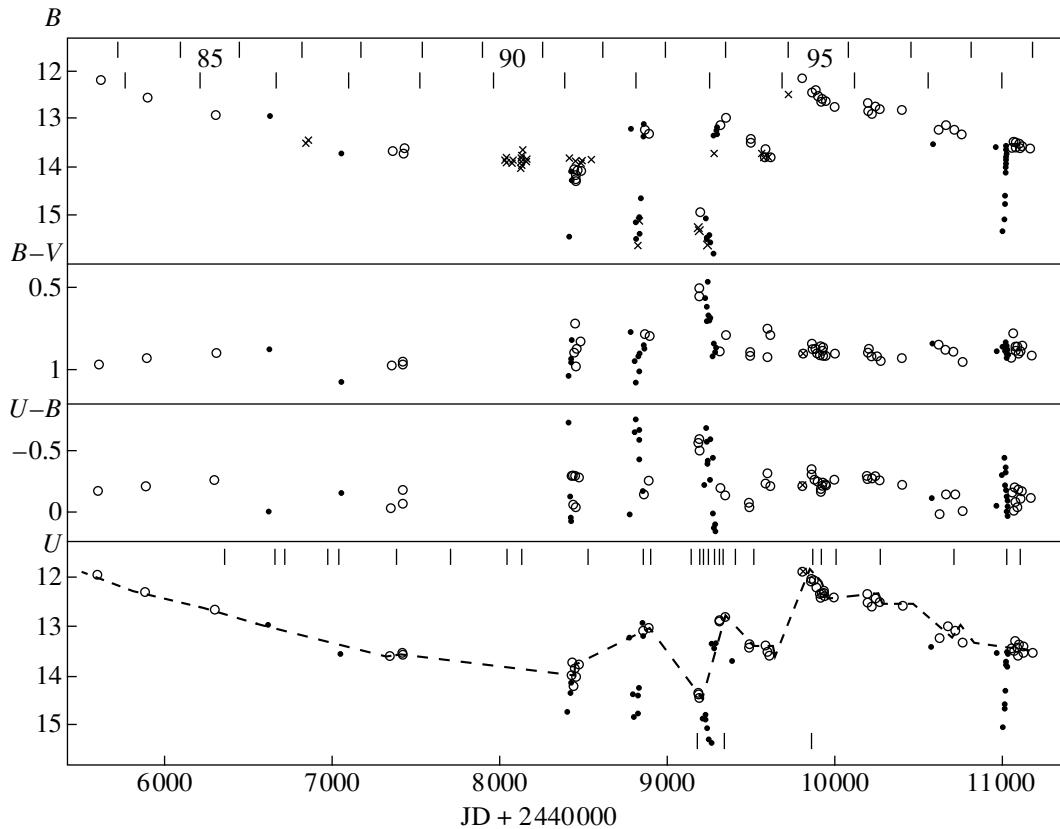


Fig. 1. U , B light curves and $B-V$, $U-B$ color curves of AS 338. The filled and open circles correspond to phase $\phi < 0.1$ and to the remaining phases, respectively. The crosses represent photographic B magnitude estimates. The crossed circle is the magnitude estimate for the star in early 1995 obtained by Elizalde *et al.* [7]. The vertical bars near the upper x axis mark the dates of minimum light for the star ($\phi = 0$) computed from the ephemeris of Munari [4]; the bars above and below the U light curve of the star mark, respectively, the dates of its spectroscopic observations and the dates for which the energy distributions are shown in Fig. 6.

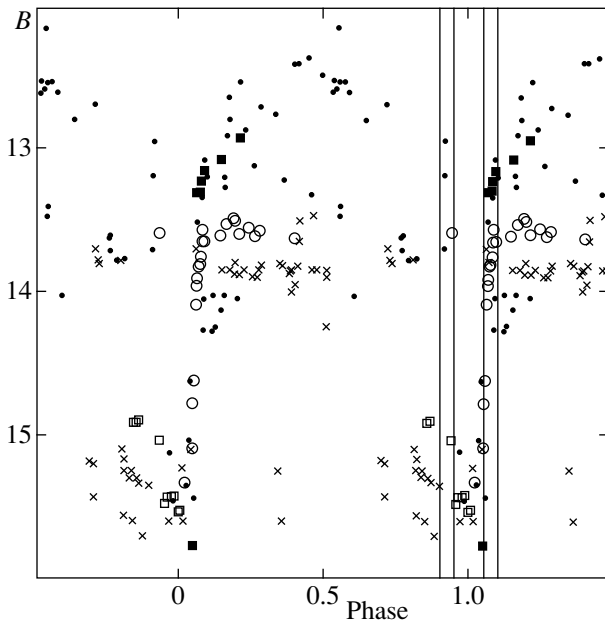


Fig. 2. The B light curve of AS 338 folded by using the ephemeris from [4]. The crosses represent photographic magnitude estimates. The open and filled squares indicate the star's brightness in 1993; the circles indicate its brightness in 1998 (see the text for details).

Accordingly, the flux estimates in Table 4 refer to it. In quiescent state, the blend is dominated by [O III] $\lambda 5007$. At the same time, the line marked in Table 4 as $H\gamma$ is the $H\gamma + [\text{O III}]$ blend in quiescent state.

On June 10, 1993, spectroscopic observations of AS 338 were carried out at short ultraviolet wavelengths aboard the IUE Space Observatory, and its optical spectrum was obtained in Asiago on June 14, 1993. Judging by the star's photometric observations in July 1993, we may assume that it could not undergo appreciable changes in four days between its optical and ultraviolet observations. We therefore consider the composite spectrum of AS 338 (see Fig. 6) as a single spectrum that characterizes the quiescent state of the hot component in June 1993. Fluxes in the most intense ultraviolet lines are given in Table 5. Note the presence of He II $\lambda 1640$ among them.

Figure 6 also shows spectral energy distributions for the hot component of AS 338 during the two subsequent outbursts of its hot component in 1993 and 1995. They are marked in Fig. 1 by vertical bars under the U light curve of the star and correspond to the photometric observations of AS 338 on December 25, 1993,

Table 1. Photoelectric *UBV* observations of AS 338

JB 2400000+	<i>U</i>	<i>B</i>	<i>V</i>	JD 2400000+	<i>U</i>	<i>B</i>	<i>V</i>
45588	11.97	12.15	11.19	49589	13.36	13.61	12.87
45876	12.31	12.53	11.60	49598	13.45	13.78	12.87
46290	12.65	12.91	12.01	49610	13.54	13.77	12.99
46615	12.95	12.95	12.07	49862	12.04	12.40	11.56
47046	13.55	13.70	12.63	49867	12.09	12.40	11.53
47347	13.60	13.63	12.66	49884	12.08	12.36	11.49
47417	13.55	13.62	12.66	49902	12.23	12.48	11.58
47418	13.53	13.71	12.76	49920	12.40	12.60	11.69
48410	14.70	15.44	14.41	49921	12.34	12.52	11.66
48423	14.32	14.27	13.34	49924	12.33	12.58	11.69
48424	14.15	14.27	13.32	49929	12.31	12.53	11.66
48425	14.12	14.05	13.23	49936	12.30	12.53	11.62
48438	13.97	14.28	13.39	49944	12.37	12.60	11.69
48439	13.73	14.03	13.32	49999	12.41	12.69	11.79
48442	14.19	14.25	13.36	50199	12.34	12.64	11.75
48451	13.83	14.13	13.16	50200	12.52	12.80	11.93
48456	13.99	14.03	13.16	50224	12.59	12.87	11.96
48476	13.76	14.05	13.22	50245	12.41	12.71	11.80
48783	13.21	13.19	12.42	50268	12.49	12.76	11.82
48807	14.35	15.12	14.17	50403	12.57	12.80	11.88
48813	14.80	15.46	14.39	50584	13.41	13.52	12.68
48832	14.75	15.35	14.43	50625	13.22	13.20	12.35
48835	14.36	15.04	14.04	50669	12.97	13.12	12.24
48839	14.19	14.63	13.73	50714	13.07	13.22	12.33
48856	13.16	13.34	12.49	50755	13.31	13.32	12.37
48859	12.90	13.08	12.21	50963	13.54	13.59	12.70
48864	13.05	13.20	12.42	50998	15.03	15.33	14.46
48891	13.01	13.27	12.48	51010	14.65	15.09	14.25
49190	14.35	14.92	14.43	51011	14.57	14.78	13.92
49192	14.33	14.92	14.37	51013	14.30	14.62	13.73
49196	14.40	14.91	14.36	51016	13.73	14.09	13.24
49227	14.81	15.04	14.48	51017	13.78	13.96	13.06
49235	14.78	15.48	14.87	51018	13.79	13.91	13.04
49239	14.86	15.44	14.98	51020	13.82	13.82	12.93
49245	15.03	15.44	14.75	51021		13.81	12.92
49248	15.01	15.43	14.77	51023	13.80	13.76	12.83
49254		15.54	14.85	51025	13.53	13.57	12.71
49256	15.26	15.53	14.85	51026	13.56	13.65	12.75
49275	15.32	15.77	14.86	51029		13.65	12.73
49281	13.32	13.31	12.47	51052	13.46	13.61	12.68
49287	13.42	13.30	12.41	51063	13.52	13.53	12.75
49289	13.33	13.23	12.34	51072	13.29	13.49	12.63
49294	13.31	13.16	12.29	51074	13.44	13.51	12.62
49319	12.87	13.08	12.19	51081	13.57	13.60	12.74
49320	12.86	13.08	12.19	51095	13.38	13.56	12.66
49347	12.78	12.93	12.15	51104	13.51	13.61	12.72
49495	13.40	13.47	12.56	51111	13.41	13.58	12.72
49496	13.35	13.40	12.51	51164	13.52	13.63	12.71

Table 2. Photographic *B* observations of AS 338

JD 2400000+	mg	JD 2400000+	mg
33129	15.60	48121	13.85
33144	15.70	48122	14.00
33150	16.20	48123	13.85
33153	15.35	48127	13.95
33352	15.60	48130	13.82
36456	13.85	48132	13.65
36456	13.90	48152	13.85
36456	14.25	48158	13.85
36456	13.90	48414	13.80
37020	15.10	48452	13.85
37023	15.25	48478	13.88
37023	15.56	48484	13.85
37024	15.17	48503	13.90
37030	15.30	48509	13.82
37044	15.33	48538	13.80
37840	15.18	48542	13.82
37844	15.20	48827	15.60
37845	15.43	48839	15.10
41448	15.23	49185	15.25
44196	15.25	49193	15.30
46832	13.50	49241	15.60
46852	13.47	49273	16.18
48029	13.85	49280	13.70
48036	13.88	49567	13.70
48037	13.80	49570	13.78
48063	13.90	49572	13.80
48073	13.85	49604	13.78
48119	13.88		

Table 3. Photometric *JHKL* observations of AS 338

JD 2400000+	<i>J</i>	<i>H</i>	<i>K</i>	<i>L</i>
45588	8.70			
45876	8.68	8.04	7.48	
46184	9.04	8.22	7.75	7.26
46193				7.20
46194	8.87	8.15	7.68	7.37
46330	8.70	8.09	7.56	7.07
46691	8.82	8.03	7.58	7.15
47048	8.84	8.11	7.63	
47417	8.83		7.60	
48063	9.12		7.88	
48118	9.00		7.89	
48852	8.93		7.70	
49289	9.02		7.65	
49292	9.06		7.74	
49884	8.70		7.53	
49936	8.71	7.96	7.51	7.13
50211	8.81	7.96	7.51	7.08
50268	8.79		7.52	
51034	9.10	6.28	7.71	7.16

Table 4. Optical emission-line fluxes from AS 338 (in units of 10^{-14} erg cm^{-2} s^{-1})

λ , Å	Line	Date						
		Oct. 8, 1992	June 10, 1993	July 26, 1993	Aug. 25, 1993	Nov. 22, 1993	Dec. 16, 1993	Feb. 24, 1994
3869	[Ne III]	Y	54	52	54	N	N	N
3968	He I + [Ne III]	21	25	22	19	Y	N	N
4026	He I + He II	10	4.4	Y	4.8	N	N	Y
4101	H δ	45	35	30	32	31	25	20
4340	H γ	81	56*	97*	94*	46	43	41
4471	He I	30	7.6	7	9	14	Y	7.7
4641	N III	N	13	18	15	N	Y	Y
4686	He II	N	21	26	28	N	N	N
4861	H β	170	100	103	86	117	124	90
4922	He I	16	13	6	11	9.5	7.8	5.4
5007	[O III]	63**	85	110	104	25**	37**	23**
5755	[N II]	Y	1.2	3	Y	N	Y	Y
5806	CIV	N	15	20	19	N	N	N
5876	He I	60	30	35	35	29	26	17
6314	[S III]	Y	2	1.8	6	N	N	2.7
6563	H α	934	380	463	373	736	926	618
6677	He I	29	14	16	14	12	24	10
7065	He I	56	19	34	37	Y	N	Y

Notes: Blend Y—line is present; N—line is absent.

* H γ + [O III] blend;

** [O III] + He I blend.

and May 24, 1995 (Table 1). The December 16, 1993 spectrum of AS 338 is shown in Fig. 4.

For comparison with the spectra of other classical symbiotic stars, the spectrum of AS 338 is shown in

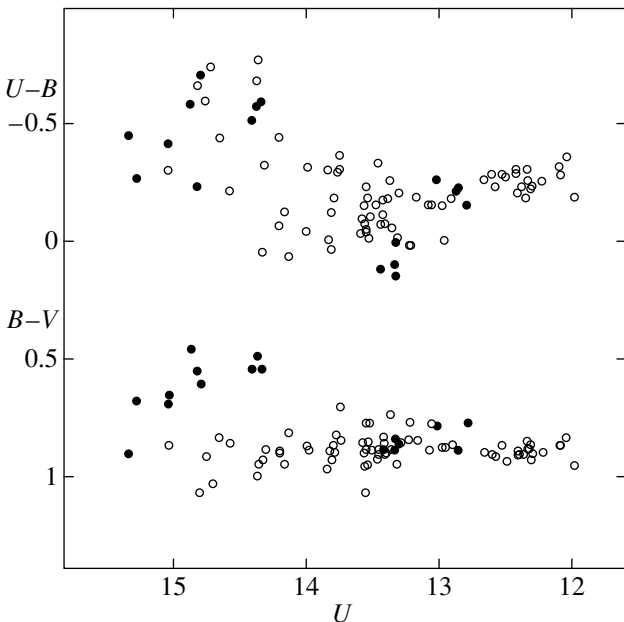


Fig. 3. $U-B$, U and $B-V$, U diagrams. The filled circles mark the star's positions in 1993.

Fig. 7 together with that of YY Her, which was also obtained with the 1.82-m Asiago Astronomical Observatory telescope. The YY Her spectrum exhibits intense TiO bands, which are of appreciably lower contrast in the AS 338 spectrum. At the same time, there are no forbidden [Ne III], [O III], and [N II] lines in the YY Her spectrum, which are intense in the AS 338 spectrum during quiescent state of its hot component.

VARIABILITY

To trace the optical light variations in the hot component of AS 338 associated with the evolution of its activity alone, the points in the light curve that do not fall at the times of its eclipses by the red giant are indicated by large circles in Fig. 1 and are connected by dashes. These include points with phases outside the range $\phi = 0 \pm 0.1$. As we see from Fig. 2, they definitely lie outside the eclipses. These points suggest that the hot component, which flared up in 1983 [3, 4], gradually faded from 1983 until 1991, and in 1991 it was $\sim 2^m.5$ fainter in U and B . In 1992, it again brightened by $\sim 1^m$, but faded to the 1991 level in 1993. At that time, He II lines, which were not seen in 1983–1992 [4, 9], appeared in the AS 338 spectrum (Figs. 4, 6, 7).

Thus, the temperature of the hot component of AS 338 abruptly increased in 1993. In this state, its eclipse

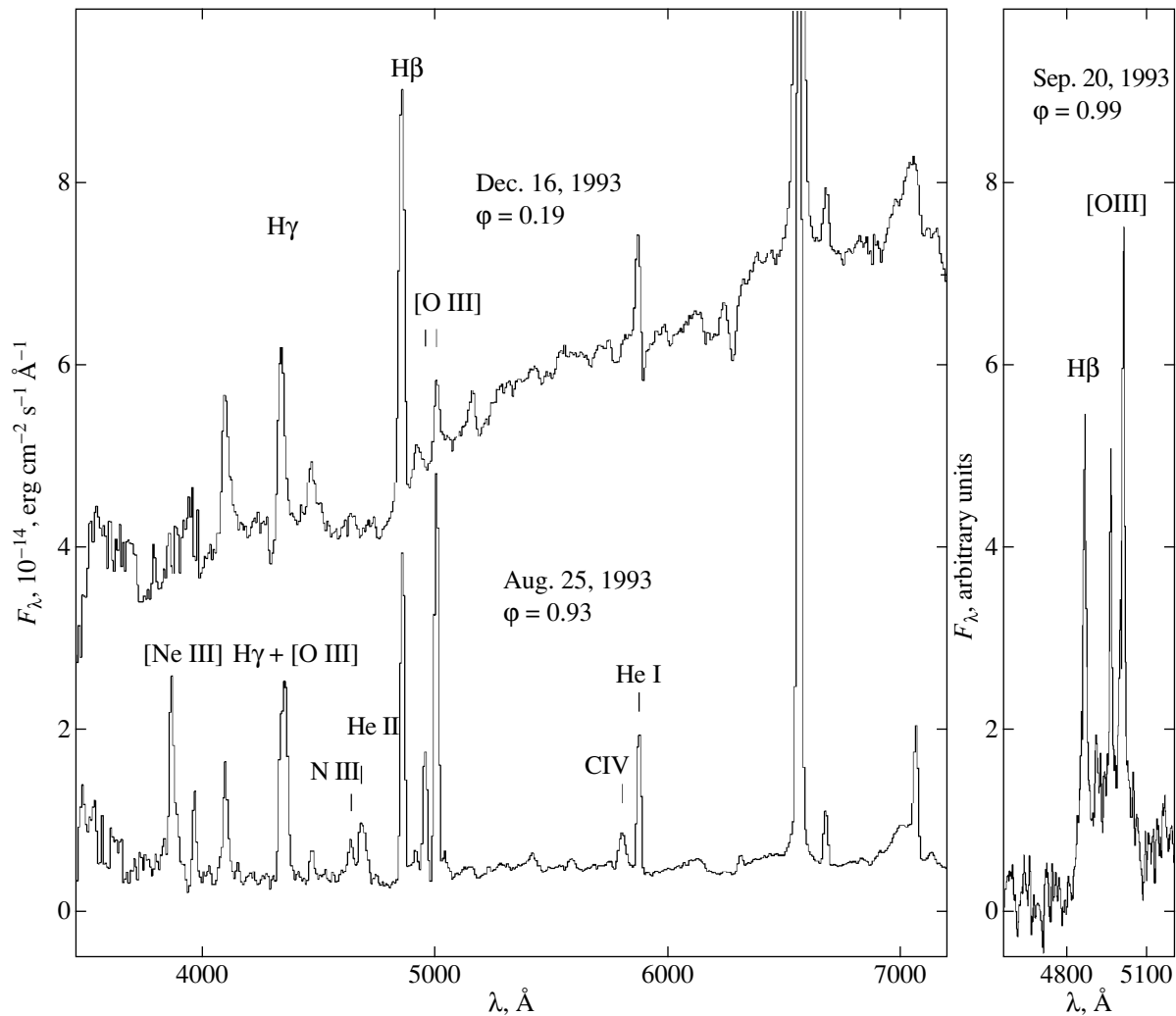


Fig. 4. The spectra of AS 338 during quiescence of its hot component (August 25 and September 20, 1993) and at its maximum optical light during outburst (December 16, 1993). The spectrum, whose portion is shown in the right panel, was obtained during eclipse of the hot component less than 24 days before its outburst. During active state, the line marked as [O III] λ 5007 is actually its blend with He I λ 5016.

ingress occurred in August 1993. However, before its eclipse egress, it again flared up and became as bright as it was in 1985 (Fig. 1). The outburst occurred in the interval August 25–October 14, 1993, while its eclipse egress occurred on October 20, 1993. The photometric evolution of the hot component in 1993 can be clearly traced in Fig. 2, in which the points for this year are indicated by large squares: open squares before its outburst and filled squares after its onset. The arguments that were used to establish that the outburst occurred during its eclipse are given below. We talk about this, because the optical brightness of AS 338 after the outburst actually declined (the first filled square in Fig. 2) because of this.

By the next eclipse in late 1994, the hot component of AS 338 had again faded by $\sim 1^m$ (Fig. 1). After the eclipse in 1995, however, it became as bright as it was in 1983, i.e., during maximum outburst. The activity

cycle restarted, as it were. The fairly smooth photometric evolution of the star within the first years after these two strongest outbursts also looks similar so far.

Thus, characterizing the outburst activity of the hot component of AS 338, we can say that its new cycle began after a short-time return of the hot component to quiescent state, while its maximum outburst occurred after a medium-level pre-outburst. Such a two-step outburst development was also observed, for example, in the classical symbiotic star Z And [10, 11]. Note that, over the fifteen years of our spectroscopic observations

Table 5. Ultraviolet emission-line fluxes from AS 338 (in units of 10^{-14} erg cm^{-2} s^{-1})

Si IV 1400	[N IV] 1485	C IV 1550	He II 1640	[O III] 1665	N IV 1721	N III] 1750	Si III] 1892	C III] 1908
6.4	10.4	48	22	17	3.9	19	12	43

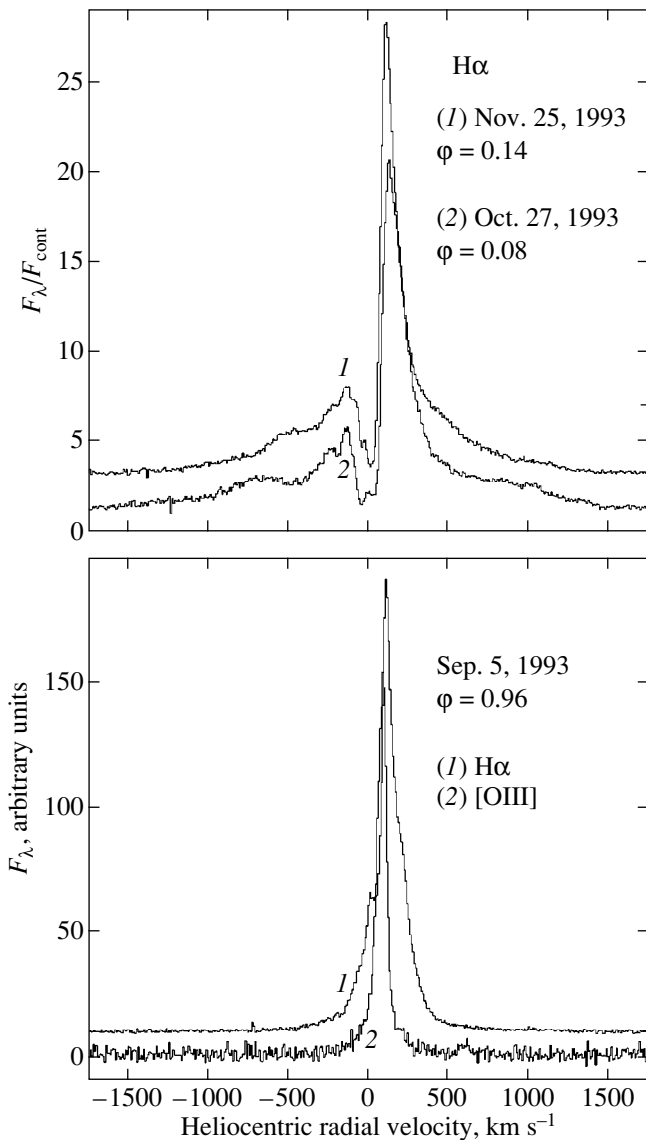


Fig. 5. The $H\alpha$ and $[O\ III]\ \lambda 5007$ profiles during quiescence of the hot component of AS 338 (September 5, 1993) and during its outburst (October 27 and November 25, 1993). In the upper panel, the intensity normalized to continuum is laid off along the y axis. For clarity, curve (1) was displaced along the y axis by 4 units. The September spectrum was taken with an exposure that is too short to determine the continuum level; in this case, the recorded intensity is essentially laid off along the y axis.

of AS 338, we detected the He II $\lambda 4686$ line in its optical spectrum only in June–August 1993. Before that, the last spectroscopic observations of AS 338 were performed in October 1992, and the hot component was still in active state at this time (Table 4). No He II line was detected in the September 1993 spectrum (its portion is shown in the right panel of Fig. 4). Nevertheless, the hot component was still in quiescent state at this time. Its absence may be associated both with the high noise level because of low brightness of AS 338 and with the fact that the hot component at this time was in

eclipse, and the He II line, whose formation region was localized near the hot component, must be fairly weak.

Thus, AS 338 was in a state when its hot component was actually hot by the standards of symbiotic stars, and when, accordingly, its optical brightness was close to a minimum for a relatively short time. If it is assumed to have passed to this state immediately after our spectroscopic observations of AS 338 in October 1992, then we obtain a maximum estimate for the duration of this phase, ~ 1 year. This accounts for a mere $\sim 7\%$ of the entire period of our observations, which is atypical of Z And-type stars exhibiting an inverse dependence in the duration of quiescence and activity phases. In addition, outbursts of the hot component, for example, in the eclipsing variable classical symbiotic star BF Cyg cause glitches in the photometric period of its light variations [12], which has not yet been observed in AS 338 (Fig. 2).

As we see from Fig. 3, the $B-V, U$ diagram seemingly consists of two groups of points, which can be said to concentrate within two horizontal strips vertically displaced by $\Delta(B-V) \approx 0.3$. The points corresponding to active state of the hot component lie in the lower “redder” and longer strip ($\Delta U \approx 3.5$), while the nine points characterizing its quiescent state are located in the upper strip. These states can thus be said to be clearly distinguished by $B-V$, which, in turn, can be used to diagnose the state of the hot component if no spectroscopic observations are available for it.

We see from Fig. 3 that $B-V$ is virtually independent of the U brightness of AS 338 when the hot component is in active state. In this case, it does not matter what caused the U light variations: a change in the state of the hot component itself or its eclipse by the red giant. In any case, if the hot component is in active state, the point in the $B-V, U$ diagram is within a $\sim 0^m.4$ wide horizontal strip and the middle line corresponding to $(B-V) \approx 0.9$. In other words, the $B-V$ color index fluctuates with an amplitude as small as $\sim 0^m.2$ about its mean value of $\sim 0^m.9$, while the U magnitude of AS 338 changes by $\sim 3^m.5$. Note that we also observed such a situation, for example, in Nova Cas 95.

The $B-V$ color index decreases during a transition of the hot component from active state to quiescent one, and the point in the $B-V, U$ diagram moves to the upper strip, irrespective of when this event occurred: during or outside eclipse. Such a transition in the opposite direction occurred during another eclipse of the hot component in the fall of 1993. The two left extreme points in the $B-V, U$ diagram correspond to this event. In Fig. 2, they are indicated by the neighboring squares: open and filled. The corresponding magnitude estimates were obtained on September 25, 1993 ($\phi \approx 0.00$) and October 14, 1993 ($\phi \approx 0.05$). Thus, the transition from quiescent state to active one, i.e., the brightness rise, took no more than 19 days. Actually, however, the observed brightness declined (Fig. 2), because this

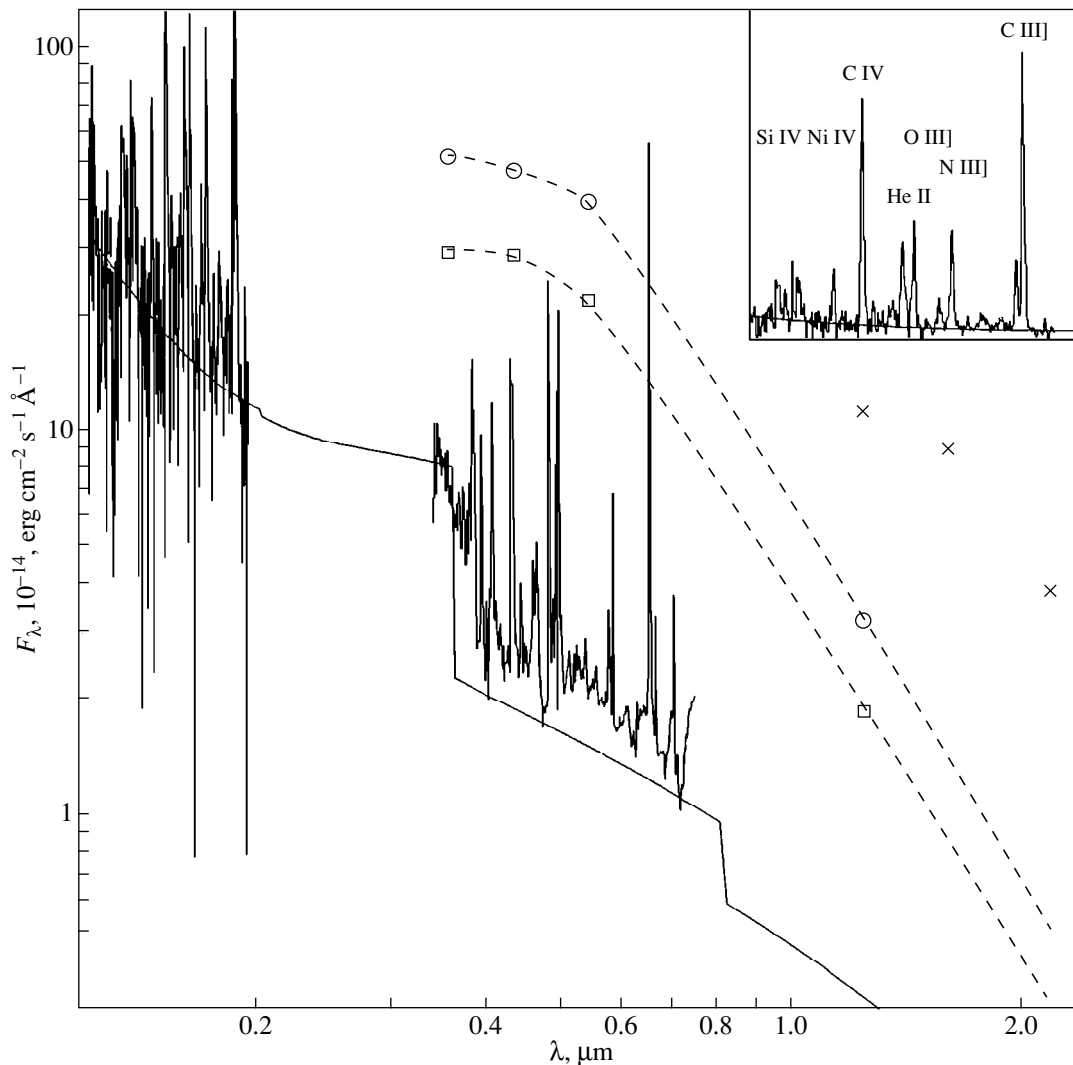


Fig. 6. The spectrum of AS 338 during quiescence of its hot component in June 1993. Its ultraviolet and optical portions were obtained on June 14 from IUE and on June 10 at the Asiago Observatory, respectively. For clarity, the ultraviolet spectrum is shown on a linear scale in the upper right corner. The solid line represents the computed continuum energy distribution of the total radiation from the hot component and the ionized envelope. The open squares and circles indicate the spectral energy distributions of the hot component of AS 338 at its maximum light recorded during its outbursts in 1993 (December 25) and 1995 (May 24), respectively. The optical spectrum of AS 338 in December 1993 is shown in Fig. 4. The crosses denote the mean brightness of the red giant. The energy distributions were corrected for interstellar reddening with $E(B-V) = 0.5$.

event occurred during an eclipse of the hot component, when it was still unseen and only the outer, uneclipsed part of its ionized envelope was observed. It is the brightness of the latter that declined, which may be caused by an appreciable decrease in the temperature of the hot component. After the eclipse egress on October 20, 1993, ($\phi \approx 0.06$), the component was bright. Thus, we may also argue that the eclipse egress in 1993 took no more than six days.

A maximum $(B-V) \leq 1.1$ was observed in AS 338 during the eclipses of the hot component in 1991 and 1992; in the latter case, the reddening effect when the eclipse began was most pronounced. At the same time, there was no reddening at all during the 1998 eclipse (Fig. 1). This effect can be naturally associated with an

increase in the fraction of light from the red giant in the total light from the symbiotic star while its hot component fades appreciably, in our case, as a result of its eclipse. The different magnitude of the effect is explained by the different brightness of the hot component at these times.

We see from Fig. 1 that, during the activity of the hot component, the main variations in $U-B$ occur during its eclipses. When a total eclipse begins, this color index decreases appreciably; i.e., AS 338 becomes bluer in this color, which seems quite natural, because the light from the hot component (similar in energy distribution in this spectral range to late B supergiants) is replaced by the light from the outer, uneclipsed layers of its ionized envelope. We also observed such a phenomenon,

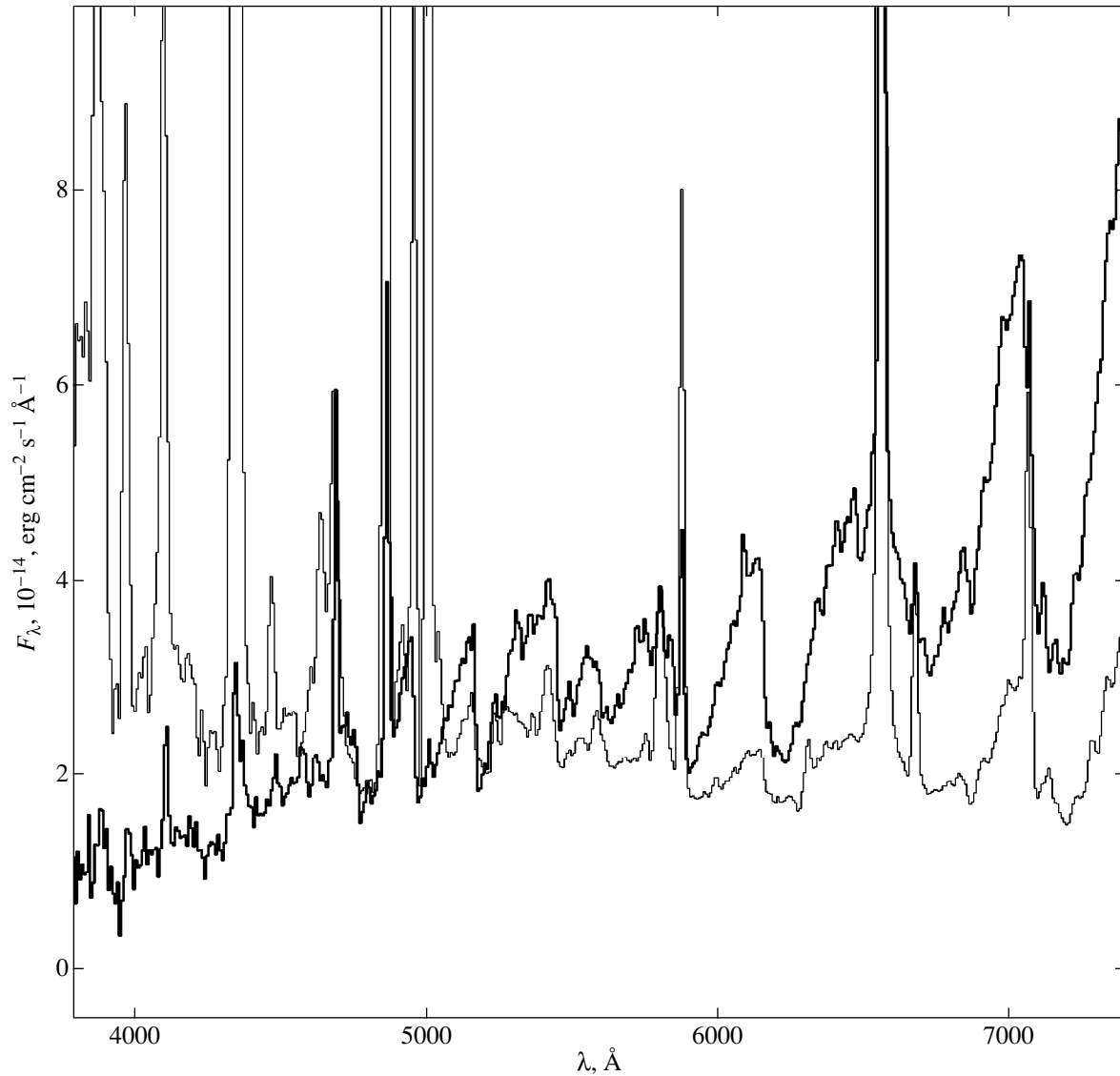


Fig. 7. The spectra of AS 338 (thin line) and YY Her (heavy line) obtained at the Asiago Observatory on July 26, 1993, and August 21, 1997, respectively. They were both corrected for interstellar reddening with $E(B-V) = 0.5$ and 0.2 , respectively.

for example, in Nova Cas 1995, when it passed from the hot-supergiant phase to the nebular phase. In 1986, we took spectra of AS 338 during (August 9, 1986, $\phi \approx 0.01$) and outside (September 29, 1986, $\phi \approx 0.12$) eclipse of the hot component. The two spectra exhibited the H γ , H β , and He I $\lambda 4922$, 5016 emission lines, as well as Fe II and [Fe II] lines. In the latter case, however, they were superimposed on a bright continuum, which was barely noticeable during the eclipse. This also suggests that the hot component of AS 338 is capable of producing a region that is larger in size than the binary system in question even in quiescent state.

When the hot component passes to quiescent state and when its temperature increases significantly, the gas ionized by it becomes the main source of optical radiation, even when it is not eclipsed by the red giant. The $U-B$ color index of AS 338 therefore decreases

during its transition from active state to quiescent one, much as it does during its eclipses in active state (Fig. 1). It should also be noted that, for $U \leq 13^m$, i.e., when the hot component is brightest, there is a tendency for $U-B$ to decrease as its brightness increases: $\Delta(U-B) \propto 0.14U$. In other words, its color temperature in this spectral range increases, while the component itself can be said to become bluer. At the same time, it becomes redder in $B-V$: $\Delta(B-V) \propto 0.03U$.

During a transition from quiescent state to active one, the He II and C IV lines disappear from the stellar spectrum, and the forbidden lines weaken appreciably (Table 4). Note also that, in quiescent state, the equivalent width of He II $\lambda 4686$ measured relative to the continuum near a wavelength of 3600 Å increased from June until August, suggesting an increase in the temperature of the hot component during this period. $W(\text{He II}) \approx$

23, 30, and 45 Å on June 10, July 26, and August 25, 1993, respectively. In active state of the hot component, the observed optical energy distribution undergoes no significant variations with stellar brightness. The component has always been similar in colors to late B supergiants. However, the emission-line fluxes increase appreciably as its brightness declines [4], suggesting an increase in its effective temperature (see below for more details).

THE COOL COMPONENT

Estimates of the interstellar reddening for AS 338 were obtained by different methods: $E(B-V) \approx 0.7$ [3, 4] and $\approx 0.45-0.40$ [13, 14]. The color excess determined from the ratio of fluxes in the He II $\lambda 1640$ and 4684 lines in the June 1993 combined spectrum with allowance for errors in their estimates is $E(B-V) \approx 0.50 \pm 0.05$. We take this value in the subsequent analysis.

The $B-V$ color for red giants is insensitive to spectral type and is $\sim 1^m.55$ [15]. At the same time, its maximum value for AS 338 at $E(B-V) \approx 0.5$ is $\sim 0^m.6$. Thus, even at minimum visible light of the hot component, the red giant contributes only slightly to the B and V light from this symbiotic star. This is clearly seen in Fig. 7, in which the AS 338 spectrum is shown together with the YY Her spectrum. The contrast of TiO bands in the YY Her spectrum is appreciably higher, and the giant's contribution to the light from this symbiotic system produces a certain tilt in the continuum energy distribution.

If the increase in $B-V$ observed during the 1992 eclipse (Fig. 1) is attributed to an increase in the fraction of light from the red giant in the total light from the symbiotic star, then its visual magnitude at that time is $V_g \approx 16.2$. Accordingly, it contributes $\sim 20\%$ to the visual brightness of AS 338 during the 1992 eclipse of the hot component. The contribution of the red giant in B is even smaller, while in U it is completely unnoticeable. In 1998, the optical brightness of AS 338 was approximately the same as that in 1992, both during and outside eclipse. However, no appreciable reddening of $B-V$ was observed during the 1998 eclipse (Fig. 1). Consequently, the visual brightness of the red giant at this time was lower than that during the 1992 eclipse.

The J, V, K, V , and $(J-K), V$ (where $V \in [11.5, 12.7]$) diagrams constructed from the data of Tables 1 and 3 reveal a clear correlation between the visual and infrared magnitudes of AS 338: $J = 0.20V + 6.38$, $K = 0.11V + 6.21$, $(J-K) = 0.09V + 0.17$. Thus, as the visual brightness increases, the infrared brightness of AS 338 also rises, while the $J-K$ color index decreases. Since the red giant is unseen in the visual light from AS 338 when $V \leq 12.7$, the correlation between $J, K, (J-K)$, and V implies that the hot component at maximum light contributes appreciably to the infrared emission from AS 338, reducing the $J-K$ color index. If the infrared

brightness of AS 338 is plotted against orbital phase (J, ϕ and K, ϕ), then the minimum and maximum of $J-K$ occurs at phase $\phi \approx 0$, i.e., during eclipse of the hot component. This also confirms the above conclusion about an appreciable contribution of the hot component to the infrared emission from AS 338.

Using the above J, V and K, V relations, we can estimate the magnitudes for the source of excess infrared emission, i.e., the hot component. For example, when its visual magnitude is $V_h \approx 11.5$, we have $J_h \approx 10.4$, $K_h \approx 9.9$, and $(J-K)_h \approx 0.5$. The $(J-K)_h$ color index, whose value corrected for interstellar reddening is $\sim 0^m.3$, assures us that the estimated excess emission cannot be associated with photometric variability of the red giant, whose $J-K$ color index must exceed 1^m .

The infrared magnitudes of AS 338 during eclipse of the hot component, which can be taken as the magnitudes of the red giant, were estimated from the J, ϕ and K, ϕ relations to be, respectively, $J_g \approx 9.05$ and $K_g \approx 7.70$, and, accordingly, $(J-K)_g \approx 1.35$. Substituting this value of J_g in the $(J-K), J$ relation yields $(J-K)_g \approx 1.29$. The color index corrected for interstellar reddening is $(J-K)_{0,g} \approx 1.1$, and the red giant is classified as M3 or M5-M6, if compared with the colors of red giants of the Local Group [15, 16] or the Galactic bulge [17].

At the same time, with the visual magnitude of the red giant estimated for the 1992 eclipse, the color index is $(V-J)_{0,g} \approx 6.1$, which corresponds to a spectral type later than M6. Note also that Allen [18] classified the red giant of AS 338 by the intensity of the CO $\lambda 2.3\text{-}\mu\text{m}$ band as M6, while Munari [4] classified it by the August 1990 stellar spectrum in the range $7000-11000$ Å as M5. Figure 6 shows the infrared spectral energy distribution for the red giant of AS 338. Its bolometric flux at $E(B-V) = 0.5$ is $F_{g, \text{bol}} \approx 2.1 \times 10^{-9}$ erg cm $^{-2}$ s $^{-1}$.

THE HOT COMPONENT AND THE CIRCUMSTELLAR ENVELOPE

Figure 6 shows spectral energy distributions for the hot component during the quiescent state in June 1993 and during the outbursts in December 1993 and May 1995. The V magnitude of AS 338 in 1995 was ≈ 11.5 . We therefore used its J and K magnitude estimates obtained in the preceding section to construct the infrared spectral energy distribution of the hot component at that time. Our optical and infrared observations of Nova Cas 1995 show that the V, J , and K magnitudes of the star during the hot-supergiant phase changed in such a way that $\Delta J \propto 1.1\Delta V$ and $\Delta K \propto \Delta V$. We used these relations to estimate the magnitude of the hot component during its outburst in 1993, when $V \approx 12.15$.

In the quiescent state in which AS 338 was in 1993, its optical spectrum exhibited the He II $\lambda 4686$ line (Figs. 4, 6, and 7) that was absent in the stellar spectrum in 1991-1992. However, whereas in 1992 the star was optically bright, and, consequently, the absence of

He II $\lambda 4686$ in its spectrum appeared quite natural, in 1991 its U magnitude was approximately the same as that in 1993 (Fig. 1). Nevertheless, He II $\lambda 4686$ was unobservable, although the H I and He I lines were appreciably more intense than, say, in 1989 [4]. Thus, the temperature of the hot component is not uniquely related to its violet brightness. Note that, below, while speaking about the colors of AS 338, we keep in mind that they refer to the energy distribution corrected for interstellar reddening with $E(B-V) = 0.5$.

The continuum energy distribution and simultaneously the He II $\lambda 1640, 4686$ fluxes in the June combined spectrum (Fig. 6) can be faithfully reproduced in the standard model for a symbiotic star: hot subdwarf + ionized envelope + red giant [19]. In accordance with its high temperature $T_h \approx 8.8(\pm 0.1) \times 10^4$ K, the hot subdwarf was taken as a blackbody source of radiation. The circumstellar envelope completely absorbed L_c photons and had a temperature of 1.7×10^4 K. We did not add the red giant's radiation to the energy distribution of the hot radiation source (hot subdwarf + ionized envelope) shown in Fig. 6, because we did not set the goal of accurately fitting the entire combined June spectrum, and because the contribution of the red giant was virtually unnoticeable at short optical wavelengths. We were interested in the following question: Can the hot radiation source be described in terms of the standard model: hot subdwarf + ionized envelope completely absorbing L_c photons. The answer proved to be affirmative (Fig. 6). In this case, the bolometric flux from the hot component is $F_{h, \text{bol}} \approx 2.1 \times 10^{-9}$ erg cm $^{-2}$ s $^{-1}$ and, accordingly, $L_{h, \text{bol}}/L_{c, \text{bol}} \approx 1$. Note that, in general, $L_{h, \text{bol}}/L_{g, \text{bol}} \leq 1$ for classical symbiotic stars during their quiescence [20–22]. Adding the red giant's radiation would slightly raise the computed energy distribution; the rise would increase with wavelength.

The equivalent width of He II $\lambda 4686$ [$W(\text{He II})$] is a very sensitive indicator of the hot-component temperature (T_h) and depends only slightly on the electron temperature of the ionized envelope (T_e). For example, $W(\text{He II}) \propto T_h^{5.4}$ at $T_h \approx 8 \times 10^4$ K. At the same time, if T_e changed from 1.5×10^4 to 2×10^4 K, it would decrease by a factor of ~ 1.3 . Thus, the difference in the temperature estimates for the hot component is 5% when passing from one presumed electron temperature to another.

If L_c photons are completely absorbed in the circumstellar envelope, and if the hot-component temperature is sufficiently high, say, $> 5 \times 10^4$ K, when it can be represented as a blackbody source of radiation to sufficient accuracy, the spectral flux $F(3600) = F_h(3600) + F_{\text{gas}}(3600)$ is a reliable indicator of the bolometric flux from the hot component $F_{h, \text{bol}}$. The $F_{h, \text{bol}}/F(3600)$ ratio depends only slightly both on T_e and on T_h . If T_e changed from 1.5×10^4 to 2×10^4 K, then it would decrease by $\sim 6\%$ at $T_h \approx 8 \times 10^4$ K. At the same time, if T_h changed from 8×10^4 to 10^5 K, it would rise by a mere $\sim 7\%$ at $T_e = 2 \times 10^4$ K.

So, based on $F(3600)$ and $W(\text{He II})$ estimated from the July 27 (Fig. 7) and August 25, 1993 (Fig. 5) spectra, we can say that $T_h \approx 9.4 \times 10^4$ K and $F_{h, \text{bol}} \approx 1.9 \times 10^{-9}$ erg cm $^{-2}$ s $^{-1}$ in the former case and $T_h \approx 10^5$ K and $F_{h, \text{bol}} \approx 1.4 \times 10^{-9}$ erg cm $^{-2}$ s $^{-1}$ in the latter case. Thus, from June until August, the temperature of the hot component increased, while its bolometric luminosity declined. This relationship between the parameters in question is characteristic of classical symbiotic stars [19].

In 1993, the eclipse of the hot component began when it was still in quiescence, i.e., with a high temperature. In this case, the main radiation source of AS 338 in U and B is the ionized envelope. The amplitude of brightness decline in U and B was $\sim 0^m.6$ (Figs. 1 and 2). Consequently, $\sim 40\%$ of the light from the gas envelope was eclipsed together with the hot component. In other words, $\sim 40\%$ of its volume emission measure was concentrated in the immediate vicinity of the hot component, say, within its Roche lobe. This is characteristic of the structure of classical symbiotic stars. The 1986 spectra of AS 338 led Munari [4] to conclude that the H I and He I line intensities decreased by a factor of ~ 2 during eclipse of the hot component. Consequently, during active state of the hot component, approximately half the volume emission measure of the envelope is also eclipsed by the red giant, and approximately half is outside this binary system.

In December 1993, the brightness of the flared hot component of AS 338 reached a maximum (Fig. 1). The corresponding spectral energy distribution is shown in Fig. 6. At this time, its optical and infrared flux was $F_{\text{opt+IR}} \approx 1.2 \times 10^{-9}$ erg cm $^{-2}$ s $^{-1}$. At the hot-supergiant phase, the flux from Nova Cas 1995 at a wavelength of 1600 Å was lower than that at 3600 Å. The fluxes became equal at the nebular phase. During the 1989 outburst of BF Cyg, when its hot component passed to the hot-supergiant phase, the ultraviolet continuum energy distribution was fitted by a curve of blackbody radiation with a temperature of $\sim 1.8 \times 10^4$ K [23]. At the same time, in October 1989, the continuum energy distribution of AS 338 in the wavelength range 1300–3200 Å can be fitted by a curve of blackbody radiation with a temperature of $\sim 1.5 \times 10^4$ K. The corresponding spectroscopic observations were carried out aboard IUE. In 1989, the star was optically appreciably fainter than in December 1993, and the contrast of emission lines was higher against the continuum background. To estimate the total ultraviolet flux, we can therefore assume that the energy distribution in this spectral range in December 1993 can be described by a curve of blackbody radiation with a temperature $\leq 1.5 \times 10^4$ K.

At a temperature of $\sim 1.5 \times 10^4$ K, the total ultraviolet flux from AS 338 in December 1993 is estimated to be $F_{\text{UV}} \approx 1.2 \times 10^{-9}$ erg cm $^{-2}$ s $^{-1}$. Note that, if the spectral flux in the entire ultraviolet range is equal to its value at 3600 Å, then $F_{\text{UV}} \approx 0.8 \times 10^{-9}$ erg cm $^{-2}$ s $^{-1}$. Such changes in the estimate of F_{UV} do not affect sig-

nificantly the total optical and ultraviolet flux from the hot component of AS 338. When using the first estimate of F_{UV} , we obtain $F_{UV+opt+IR} \approx 2.4 \times 10^{-9}$ erg cm⁻² s⁻¹. However, it does not include the L α flux.

During the transition of AS 338 from quiescent state to active one, which occurred during the eclipse of the hot component in 1993, the star's U brightness declined by a mere $\sim 0^m.1$. Thus, the continuum flux from the ionized part of the gas envelope uneclipsed by the red giant did not change appreciably during the outburst of the hot component. Consequently, we may assume that the flux of L_c photons emitted by the hot component did not change appreciably either; at least it could not decrease. If the outburst of the hot component were accompanied by an increase in the mass-loss rate, then the flux of L_c photons would increase to maintain the outer envelope layers in ionized state. Assuming its value to be constant, the correction to the total flux from the hot component of AS 338 in December 1993 due to the L α flux is $\sim 0.7 \times 10^{-9}$ erg cm⁻² s⁻¹, and the final estimate of its bolometric flux is $F_{h, bol} \approx 3.1 \times 10^{-9}$ erg cm⁻² s⁻¹. Thus, the bolometric flux from the hot component during its 1993 outburst increased by a factor of ≤ 2.2 compared to its minimum value recorded in the quiescent state of the hot component in August 1993.

In 1995, AS 338 underwent a recurrent, stronger outburst (Fig. 1). At this time, it was $\sim 0^m.9$ brighter in U than during the 1993 outburst, although the optical energy distributions were similar during these outbursts (Fig. 6). We can thus say that the bolometric flux from the hot component during the 1995 outburst increased by a factor of ≤ 5 compared to its value in the quiescent state of the hot component in August 1993. Note that a modest change in the bolometric flux from the hot component was observed during the 1989 outburst of BF Cyg [23] and during outbursts of Z And [11]. At the same time, the bolometric flux from the classical symbiotic star YY Her during its outburst in 1993 increased by a factor of ~ 10 [24].

So, during the 1993 outburst, when the hot component passed from the hot-subdwarf phase to the hot-supergiant phase, its bolometric luminosity increased by a factor of ≤ 2.2 . At the same time, the temperature of the hot subdwarf was $T_h \approx 10^5$ K, while the color temperature of the hot supergiant in the ultraviolet did not exceed 1.5×10^4 K. It was ~ 7200 K in the optical range. If the hot component in active state were assumed to be generally similar to a hot supergiant with an effective temperature of $\sim 1.5 \times 10^4$ K, then the flux of L_c photons ionizing the envelope would drop by a factor of ≥ 30 during its transition to this state from the hot-subdwarf phase, which is accompanied by an increase in the bolometric luminosity by only a factor of ≤ 2.2 .

Accordingly, the sizes of the H II region would have decreased significantly, and, since approximately half the volume emission measure of the gas envelope is eclipsed by the red giant, it would have become smaller

in size than the red giant. In other words, it would have undergone a total eclipse. Accordingly, during the 1993 eclipse, when the outburst of the hot component occurred, the optical brightness of AS 338 would have declined to the level of its red giant. This was not observed even in V and during all the remaining eclipses when the hot component was in active state. This implies that the H II region always extends beyond this binary system. Accordingly, the H I and He I emission lines were detected in the AS 338 spectrum that we obtained during the 1986 eclipse.

Note that the effect of incomplete obscuration of the light from the circumstellar envelope was also observed during the eclipse of the hot component of BF Cyg which occurred shortly after its 1989 outburst, although an effective temperature of $\sim 1.2 \times 10^4$ K was assigned to it at this time [12]. During the 1975 outburst of CI Cyg, its hot component was classified by the optical spectrum as an F5 supergiant with an effective temperature of ~ 7600 K [25]. However, when its eclipse ingress occurred and when the continuum weakened appreciably, the H I and He I emission lines appeared in the CI Cyg spectrum.

Given that approximately half the volume emission measure of the gas envelope around AS 338 is eclipsed by the red giant, the ratio of U fluxes from the gas envelope and the hot component during the 1993 outburst, when its eclipse egress occurred in October, is $F_{gas}(3600)/F_h(3600) \approx 0.25$. This corresponds to a temperature of $\sim 3 \times 10^4$ K for a blackbody source of radiation. Thus, the above discussion leads us to conclude that the hot component of AS 338 in active state cannot be considered as a spherically symmetric radiation source, although it is similar to a hot supergiant in spectral energy distribution. This can also explain the fact that, as the star's optical brightness declines, the emission-line fluxes increase considerably, i.e., the flux from the ionized envelope increases significantly, although the optical energy distribution undergoes no appreciable changes.

Of course, they are not closely similar even in colors. For example, in December 1993, the hot component of AS 338 can formally be classified by $(U-B)_0 \approx -0.44$ and $(B-V)_0 \approx 0.33$ as a supergiant of spectral type A0-B9 and F5, respectively. At the same time, these colors correspond to a blackbody source of radiation with a temperature of ~ 7200 K. These peculiar features in the spectral energy distribution of the hot component of AS 338 are also typical of the hot components of other classical symbiotic stars, which pass during their outbursts to the hot-supergiant phase, and of slow novae. Thus, when we talk about their outward similarity to supergiants, we keep in mind that the color temperature of the hot components of symbiotic stars lies in the range of effective temperatures for hot supergiants.

In quiescent state of the hot component of AS 338, the stellar spectrum exhibits intense forbidden [O III], [Ne III], and [N II] lines (Figs. 4, 6, 7). At the same

time, these lines are generally either absent or very weak in the spectra of classical symbiotic stars. As an example of such a symbiotic star, Fig. 7 shows the spectrum of YY Her that was obtained, as that of AS 338, with the 1.8-m Asiago telescope. Among the well studied classical symbiotic stars in the northern sky, such as AG Dra, AX Per, CI Cyg, Z And, YY Her, and BF Cyg, only the latter has intense forbidden lines in its spectrum. Their absence or low contrast against the continuum background suggests that the mass of the O^{++} , Ne^{++} , and N^+ ionization regions, on which the forbidden-line flux depends at electron densities 10^6 – 10^8 cm^{-3} , is fairly small. This may be either because the ionized region does not extend appreciably to the outer tenuous layers of the circumstellar envelope or because the density in these layers drops sharply, say, more sharply than that at a constant mass-loss rate. Note that the flux in continuum and in permitted lines is determined by the volume emission measure of the ionized envelope.

The $H\gamma + [O III] \lambda 4363$ blend (Figs. 4, 6, and 7) was resolved into these lines using two Gaussians. The ratio of the $[O III] \lambda 4363$ and 5007 fluxes in the June 14, July 27, and August 25, 1993 spectra was 0.65, 0.60, and 0.62, respectively. At $T_e = 1.5 \times 10^4$ K, this ratio corresponds to an electron density $n_e \approx 10^7$ cm^{-3} . Using the $[O III] \lambda 5007$ flux in August 1993 and assuming a solar oxygen abundance in the AS 338 envelope, we estimated the mass of the O^{++} ionization region to be $\sim 6 \times 10^{-8} M_\odot$ (D/kpc) 2 . At the same time, the volume emission measure of the ionized envelope was estimated from the spectral flux $F(3600)$ to be $\sim 2.5 \times 10^{58}$ cm^{-3} (D/kpc) 2 .

The $H\alpha$ profile in October–November 1993 is fairly complex (Fig. 5). First, it can be described as a P Cyg profile, with the corresponding very deep absorption having a two-component structure. The radial velocities of the main “red” emission peak and these two absorption components in October 1993 were +131.7, +24.6, and -40.3 $km\ s^{-1}$, respectively. In November, they changed to +113.2, +14.7, and -37.2 $km\ s^{-1}$. Second, the blue line wing exhibits a broad emission feature at a radial velocity of -650 $km\ s^{-1}$ in October and at -550 $km\ s^{-1}$ in November. An emission feature at radial velocities 800 – 1000 $km\ s^{-1}$ can also be seen in the $H\alpha$ red wing. Third, the $H\alpha$ profile has broad wings stretching to velocities of ± 1500 $km\ s^{-1}$. The $H\beta$ and He I $\lambda 5876$ lines also have such broad wings.

Whereas the first two features of the $H\alpha$ profile in the AS 338 spectrum during the outburst of its hot component were also noted, for example, in the $H\alpha$ profile in the spectrum of the flared symbiotic star BF Cyg [12], no broad wings were detected in it in the latter case. In general, they are not typical of the $H\alpha$ profiles for classical symbiotic stars. They appear in $H\alpha$ at a certain stage after the outburst evolution of a classical nova [26]. They were also noted in the peculiar symbiotic star CH Cyg during its outbursts [27].

During the quiescent state of the hot component of AS 338 in September 1993, $H\alpha$ also exhibited a P Cyg profile (Fig. 5). However, the absorption component is not as deep as that during its outburst. In general, however, when comparing the $H\alpha$ and $[O III]$ profiles, we can say that the former was cut off, as it were, in its blue part because of self-absorption of this line. Since the exposure in September was too short to reach the continuum level, it is hard to tell whether $H\alpha$ had such broad wings at this time.

DISCUSSION

Characterizing the eclipses of the hot component of AS 338, we can say that the main brightness rise begins at $\phi \approx 0.05$ and continues during $\Delta\phi \approx 0.01$; i.e., it is rather sharp (Fig. 2). At the same time, we cannot say that a distinct plateau is observed within $\phi \approx \pm 0.05$; i.e., the brightness of AS 338 is constant. Judging by the 1992 eclipse (Fig. 1), the duration of such a plateau is limited by the range $\phi \approx \pm 0.03$. The reasons why the light-curve shape can change within $\phi \approx \pm 0.05$ from eclipse to eclipse are clear. First, the absence of a distinct plateau may be associated with intrinsic light variations in the hot component of AS 338 during eclipses, as was observed, for example, during the 1993 eclipse, when it passed from quiescent state to active one. Second, the plateau duration may change because of changes in the structure of the hot radiation source, by which, as was pointed out above, we mean a combination of the hot component and the ionized envelope. The latter can be schematically broken up into two parts: the part eclipsed together with the hot component and the uneclipsed part. In this model, the sharp brightness rise, which begins at $\phi \approx 0.05$ and continues during $\Delta\phi \approx 0.01$, is attributable to eclipse egress of the hot component, which is the main contributor to the optical light from AS 338 in active state. In active state, however, it also has a different temperature, which appears to increase as its optical brightness decreases. In this case, the contribution of the eclipsed part of the circumstellar envelope increases, and the phase interval of a total eclipse of the hot radiation source narrows accordingly.

For the same reason, the amplitude of the sharp brightness rise within $\Delta\phi \approx 0.01$ may change from eclipse to eclipse. It was largest at the eclipse egress in 1993, when an outburst of the hot component occurred shortly before this event. It was $\sim 2^m.0$, $\sim 2^m.5$, and $\sim 2^m.4$ in U , B , and V , respectively. The rise occurred in ≤ 6 days. In 1998, the brightness rise in the same time interval was $\sim 1^m$ (Figs. 1 and 2).

At the eclipse egress in 1993, the brightness of AS 338 during the rapid rise immediately rose from minimum to maximum. The subsequent relatively small rise may be associated with outburst development. We can thus assume that, if the outburst occurred before the onset of eclipse, then a plateau $\Delta\phi \approx 0.1$ in duration (a total eclipse) would be observed during it.

At the same time, the entire eclipse, from its onset to the end, would continue during $\Delta\phi \approx 0.12$. The apparent red-giant radius estimated from the duration of total eclipse and eclipse egress is $R_{g, \text{app}} \approx 0.3A$, where A is the diameter of the orbit of this binary system, which is assumed to be circular. The hot-component radius is $R_h \approx 0.03A$.

If the red giant fills its Roche lobe, $M_h/M_c \approx 0.5$, and $\Sigma M \approx 1.8M_\odot$, then its radius is $R_g \approx 0.44A$. In this case, the inclination of the binary system to the line of sight is $i \geq 72^\circ$. At $P_{\text{orb}} \approx 434^d$ and $A \approx 290R_\odot$, the red-giant radius is $R_g \approx 130R_\odot$. At an effective temperature of ~ 3400 K, its luminosity is $L_g \approx 2000L_\odot$. In that case, the distance to AS 338 is $D \approx 6$ kpc, and, consequently, the mass of the O^{++} ionization region in August 1993 was $\sim 2 \times 10^{-6}M_\odot$, and the volume emission measure of the envelope was $\sim 10^{60} \text{ cm}^{-3}$. If its half was concentrated within the Roche lobe of the hot component, then the mass of this part of the circumstellar envelope was $\sim 3 \times 10^{-8}M_\odot$.

The minimum luminosity of the hot component in quiescence was $L_h \approx 1400L_\odot$ in August 1993 and $L_h \leq 3000L_\odot$ in December 1993 after its outburst. Immediately after the eclipse egress in October 1993, AS 338 was $\sim 0^m.5$ fainter than in December. Consequently, $L_h \leq 1900L_\odot$ at this time. The effective temperature of the hot component at $R_h \approx 0.03A \approx 9R_\odot$ is $T_{\text{eff}} \leq 1.3 \times 10^4$ K. We took approximately the same temperature for the blackbody source of radiation when estimating the ultraviolet flux from the hot component of AS 338 in December 1993. It should be noted that, based on a similar analysis of an eclipse of the flared hot component in BF Cyg, Skopal *et al.* [12] estimated its effective temperature to be $\sim 1.2 \times 10^4$ K. However, as was already pointed out above, neither during eclipses of the flared hot component in BF Cyg nor during eclipses of the active hot component in AS 338 did the brightness of these stars drop to the level of their red giants even at visual wavelengths; this would inevitably occur, if the hot components were spherically symmetric radiation sources with such a low temperature.

So, the active hot component of AS 338 cannot be considered as a spherically symmetric radiation source. Regions with an appreciably higher temperature than in those we observe must exist in the pseudosphere. These hotter regions produce L_c photons in the quantities required to continuously maintain an extended H II region. The binary system AS 338 is located at a large angle to the line of sight, and its hot component in active state appears fairly cool. If it were observed at a small angle, then the hot component of AS 338 would apparently appear appreciably hotter than it seems. In this case, the estimate of its bolometric flux would also increase. In other words, the previously obtained bolometric flux from the active hot component appears to have been slightly underestimated. It should be noted that the nonspherical structure of the hot component as

a radiation source was detected in the classical symbiotic star YY Her [24]. However, in contrast to the hot component of AS 338, the hot component of YY Her is capable of exciting intense He II lines in the circumstellar envelope even during its strong outbursts.

AS 338 is similar in outburst activity to classical symbiotic stars, i.e., to Z And-type stars. In that case, it has the shortest known orbital period among them. In addition, the transition of AS 338 to active state, which took less than 19 days, is one of the shortest in time. There are also a number of other differences between AS 338 and the well studied classical symbiotic stars. These, in particular, include an inverse dependence in the duration of quiescence and activity phases of the hot component and the presence of very broad wings in the H α , H β , and He I lines.

The nonspherical structure of the hot component of AS 338 as a radiation source, which may be a characteristic feature of the structure of the hot components in classical symbiotic stars, introduces a qualitative difference between them and symbiotic novae. The nature of the outbursts of the hot components in the latter is clear, in contrast to all the remaining groups of symbiotic stars. The outbursts of the hot components in symbiotic novae are associated with a thermonuclear flash of the hydrogen envelope on the surface of a white dwarf. In this case, the hot components as radiation sources remain spherically symmetric. The absence of such symmetry, at least in some classical symbiotic stars, implies the activity of accretion processes in these binary systems, which may be directly related to the activity of their hot components.

ACKNOWLEDGMENTS

This study was supported by the KBN grant no. 2P03D02112 (Polish Research Committee).

REFERENCES

1. P. W. Merrill and C. G. Burwell, *Astrophys. J.* **112**, 72 (1950).
2. D. A. Allen, *Proc. Astron. Soc. Austral.* **5**, 369 (1984).
3. R. Schulte-Ladbeck, *Messenger* **39**, 3 (1985).
4. U. Munari, *Astron. Astrophys.* **257**, 163 (1992).
5. U. Munari, B. F. Yudin, G. Sostero, *et al.*, *IAU Circ. No. 5884* (1993).
6. U. Munari, T. Tomov, B. Yudin, *et al.*, *IAU Circ. No. 6151* (1995).
7. F. Elizalde, F. Jablonski, D. Cieslinski, *et al.*, *IAU Circ. No. 6165* (1995).
8. N. E. Kurochkin, Private Communication (1999).
9. V. F. Esipov, O. G. Taranova, and B. F. Yudin, *Astrofizika* **29**, 285 (1988).
10. T. Fernández-Castro, R. González-Riestra, A. Cassatella, *et al.*, *Astrophys. J.* **442**, 366 (1995).
11. J. Mikolajewska and S. J. Kenyon, *Astron. J.* **112**, 1659 (1996).

12. A. Skopal, L. Vittone, L. Ericco, *et al.*, *Mon. Not. R. Astron. Soc.* **292**, 703 (1997).
13. V. F. Esipov, A. P. Ipatov, and B. F. Yudin, *Astrofizika* **25**, 229 (1986).
14. J. Mikolajewska, A. Acker, and B. Stenholm, *Astron. Astrophys.* **327**, 191 (1997).
15. T. A. Lee, *Astrophys. J.* **162**, 217 (1970).
16. J. Koorneef, *Astron. Astrophys., Suppl. Ser.* **51**, 489 (1983).
17. D. M. Terndrup, J. A. Frogel, and A. E. Whitford, *Astrophys. J.* **357**, 453 (1990).
18. D. A. Allen, *Mon. Not. R. Astron. Soc.* **192**, 521 (1980).
19. A. A. Boyarchuk, *Eruptive Stars* (Nauka, Moscow, 1976), p. 113.
20. A. P. Ipatov and B. F. Yudin, *Astron. Tsirk.*, No. 1471, 4 (1986).
21. F. P. Ipatov and B. F. Yudin, *Astrofizika* **25**, 435 (1986).
22. B. F. Yudin, *Astron. Zh.* **63**, 137 (1986).
23. A. Cassatella, T. Fernández-Castro, R. González-Riestra, *et al.*, *Astron. Astrophys.* **258**, 368 (1992).
24. U. Munari, E. A. Kolotilov, A. A. Popova, *et al.*, *Astron. Zh.* **74**, 898 (1997).
25. T. S. Belyakina, *Izv. Krymsk. Astrofiz. Obs.* **59**, 133 (1979).
26. E. A. Kolotilov, U. Munari, and B. F. Yudin, *Mon. Not. R. Astron. Soc.* **275**, 185 (1995).
27. T. Tomov, D. Kolev, U. Munari, *et al.*, *Mon. Not. R. Astron. Soc.* **278**, 542 (1996).

Translated by V. Astakhov

Doppler–Zeeman Mapping of the Rapidly Rotating Magnetic CP Star HD 37776

V. L. Khokhlova^{1*}, D. V. Vasilchenko², V. V. Stepanov², and I. I. Romanyuk³

¹ *Institute of Astronomy, Russian Academy of Sciences, Pyatnitskaya ul. 48, Moscow, 109017 Russia*

² *Department of Computational Mathematics and Cybernetics, Moscow State University, Moscow, 119899 Russia*

³ *Special Astrophysical Observatory, Russian Academy of Sciences, Nizhniĭ Arkhyz, Stavropol'skiĭ kraĭ, 357147 Russia*

Received June 14, 1999

Abstract—We present the results of our analysis of magnetic-field configuration and abundance anomalies on the surface of the rapidly rotating, chemically peculiar helium-strong variable B2 V star HD 37776 with unresolved Zeeman components of spectral lines. Simultaneous inversion of the observed Stokes I and V profiles, which realizes the method of Doppler–Zeeman mapping [1], has been applied for the first time. Spectroscopic observations were carried out with the Main stellar spectrograph of the 6-m Special Astrophysical Observatory telescope equipped with a Zeeman analyzer and a CCD array, which allowed spectra in right- and left-hand circularly polarized light to be taken simultaneously at a signal-to-noise ratio $S/N \geq 200$ [2]. The profile width of winged spectral lines (reaching 5 Å) is determined by Zeeman line splitting; however, the observed Zeeman components are blurred and unresolved because of the rapid stellar rotation. When solving the inverse problem, we sought for the magnetic-field configuration in the form of a combination of arbitrarily oriented dipole, quadrupole, and octupole placed at the stellar center. The observed Stokes I and V profiles for eight spectral lines of He, O II, Al III, Si III, and Fe III averaged over the visible stellar surface were used as input data. We constructed a model of the magnetic field from the condition of coincidence of magnetic maps obtained from different lines of different chemical elements and from the condition of a minimum profile residual. This model is a combination of centered coaxial dipole and quadrupole with the dominant quadrupole component at $30^\circ < i < 50^\circ$, $\beta = 40^\circ$, and a maximum surface field strength $H_s = 60$ kG. A comparison of our abundance maps with the field configuration shows that the He concentration is at a maximum in the regions of maximum radial field, while the maximum concentrations of O, Al, Si, and Fe coincide with the regions of maximum tangential field. © 2000 MAIK “Nauka/Interperiodica”.

Key words: *magnetic SP stars, Doppler–Zeeman mapping, helium-strong variables, individual stars: HD 37776*

1. INTRODUCTION

Over several decades since Babcock discovered strong global magnetic fields on Ap stars by Zeeman line splitting in circularly polarized stellar spectra, the stellar magnetic-field configuration has been customarily judged by the magnetic curve, i.e., by the dependence of the component of magnetic vector along the line of sight averaged over the visible disk (the so-called effective field) on stellar rotation phase. Dozens of stars studied in this way exhibited nearly sinusoidal magnetic curves with amplitudes corresponding to effective fields from several hundred G to several (in rare cases, more than 10) kG, suggesting that Ap stars had predominantly dipole fields. In some cases, the magnetic curve corresponded to a dipole displaced from the stellar center [3]. However, as the calculations by Hensberge *et al.* [4] showed, this configuration is virtually indistinguishable from a combination of coaxial centered dipole and quadrupole, provided that the quadrupole component is modest compared to the

dipole one. However, we know several stars whose magnetic curves are not sinusoidal and cannot be described by a displaced dipole; i.e., higher order multipoles are significant compared to the dipole. These include HD 32633 [5], HD 37776 [6], and HD 133880 [7]. These stars are the most massive and hottest representatives of the CP stars and possess the strongest magnetic fields.

The presence of magnetic fields is usually accompanied by abundance anomalies nonuniformly distributed over the stellar surface, showing up as rotational variability of line intensities.

Apart from determining the magnetic-field configuration, a comparison of the distribution of surface abundance anomalies with the magnetic-field geometry is of greatest interest in studying and understanding the physics of magnetic CP stars.

Qualitative physical considerations and calculations allowed a number of authors to predict some geometrical characteristics of magnetic CP stars [8–11].

For weak magnetic fields, the distribution of chemical anomalies can be determined from spectroscopic

* E-mail address for contacts: vlk@khokh.msk.ru

observations by simple Doppler mapping and then compared with the dipole field configuration derived from the observed phase dependence of effective magnetic field B_e . The most accurate results of such a comparison were obtained and presented by Hatzes [12]. However, because of the complex magnetic-field configuration for the above stars, it is not possible to compare the localization of chemical anomalies with the magnetic-field configuration on the basis of an integrated (surface-averaged) spectrum even qualitatively. Such a comparison can be made only by mapping the distribution of chemical anomalies and local magnetic vector over the stellar surface, i.e., by Doppler–Zeeman (D–Z) mapping, which is essentially the solution of the inverse problem—inversion of the observed integrated Stokes profiles into the local ones (at each point on the stellar surface).

The inversion method was first developed and applied by Goncharukii *et al.* [13, 14] and Vasilchenko *et al.* [1].

High-precision observed Stokes I , Q , U , V profiles for spectral lines unblended with extraneous lines of other elements, as well as a model atmosphere, equatorial rotational velocity V_{equ} , and inclination i of the rotation axis to the line of sight, are required as input data for D–Z mapping. In practice, for various reasons, it is difficult to obtain all the above data in full.

Here, our goal is to study the magnetic-field configuration and its relationship to the distribution of chemical anomalies on the surface of the magnetic CP star HD 37776 (mapping the local magnetic vector and elemental abundances) by using the method of I , V inversion [1] for an incomplete set of input data (the lack of Stokes Q and U profiles, the inability to determine i accurately, and a limited number of phases of the available spectra).

The magnetic CP star HD 37776 with a strong quadrupole field is known as a B2p helium-strong variable. The study of circular polarization with a two-channel H β polarimeter by Thompson and Landstreet [6] revealed an alternating effective magnetic field from -1680 to $+2540$ G. While discussing the pattern of magnetic curve, the authors concluded that the quadrupole component was dominant and proposed a model of the magnetic field with an indication of magnetic-pole longitudes.

Subsequently, Bohlender [15] interpreted the B_e curve by invoking the profiles of some other lines and chose the magnetic-field model in the form of a combination of centered coaxial dipole, quadrupole, and octupole. According to his model, the star is seen equator-on ($i = 90^\circ$), while the magnetic axis lies in the equatorial plane (the angle between the magnetic and rotation axes is $\beta = 90^\circ$). Based on IUE spectra for nine stars with enhanced He lines, Shore and Brown [16] analyzed variability of the C IV and Si IV resonance line profiles and noted some peculiar features of HD 37776 that distinguished it from the eight remain-

ing sample stars: an abnormal magnetic-field geometry and the inability to determine whether the field is related to magnetospheric plasma.

A fairly detailed review of the studies of HD 37776 and the corresponding bibliography can be found in [2]. These authors, who have given much attention to the investigation of the magnetic field on HD 37776 over more than ten years, have reached the following conclusion: the surface field of this unique star probably reaches 60 kG and has a predominantly quadrupole configuration; the surface distribution of chemical elements is nonuniform, which results in spectroscopic variability, with the disk-averaged intensities of He and Si lines varying in antiphase.

2. OBSERVATIONAL DATA

Based on photometric observations, Adelman [17] refined the rotation period of HD 37776. He gave the ephemeris

$$\begin{aligned} \text{JD}(B_e^+) &= 2445724.669(\pm 0.02) \\ &+ 1.538675(\pm 0.000005)E. \end{aligned}$$

Our spectra of HD 37776 were obtained with the Main stellar spectrograph of the 6-m Special Astrophysical Observatory telescope using a CCD array and a Zeeman analyzer with 0.3 Å resolution and a signal-to-noise ratio ≥ 200 .

Since the spectral range covered was narrow (100 Å), we observed two spectral regions centered at 4550 and 5875 Å. Julian dates and phases of our spectra are given in Table 1.

The conditions for obtaining the spectra and their initial reduction were described in detail by Romanyuk *et al.* [2]. Subsequently, we adjusted the continuum placement and the wavelength scale at the Institute of Astronomy (Russian Academy of Sciences) by using the DECH software package [18].

We used the Stokes I profiles as the half-sum of right- and left-hand polarized spectra and the Stokes V profiles as their half-difference. Despite the strong magnetic field, the Zeeman components in the I and V profiles are unresolvable because of the rapid stellar rotation.

In the available spectral ranges, we performed line identification in an effort to find unblended lines of various elements. For this purpose, we computed a synthetic spectrum for Kurucz's model [19] with $T_{\text{eff}} = 22\,000$ K, $\log g = 4.5$, and solar chemical composition. This computed synthetic spectrum was also used to adjust the continuum placement. The computations were carried out with the STARS software package [20].

Because of the large profile width, we were able to select only eight lines of He I, Si II, O II, Al III, and Fe III, which were relatively free from blending. These

lines with the atomic data required for the analysis are listed in Table 2.

In addition to the standard notation used in columns 1–5, columns 6 and 7 give radiative and collisional damping constants; column 8, transition-producing levels; and column 9, relative intensities (k) of the multiplet component under consideration (for the He I 5876 line, which belongs to the triplet series and consists of six close components, with each having its own Zeeman pattern of magnetic splitting). The relative intensities (k) were determined under the assumption of LS coupling (see, e.g., [21]). The Lande factors and relative intensities of the Zeeman components computed by Beckers [22] are given for each line in the second row (under the dashed line). The atomic data in Table 2 were taken from [23–26].

3. DOPPLER–ZEEMAN MAPPING OF HD 37776

We used the computational code for I and V inversion [1] supplemented with the possibility of determining arbitrarily oriented multipole field components of higher orders than the quadrupole to map the surface magnetic field and elemental abundances of HD 37776. The implications of this code update are discussed below (in Sect. 4).

Recall that our code is peculiar in that it uses analytic fits to describe the sought-for local profiles of spectral lines [1, 27]. The parameters of the fits do not depend on the coordinate of a point on the stellar surface (i.e., on the local magnetic vector or local abundance), but depend on the atomic parameters of a specific line and the physical parameters of the stellar atmosphere.

3.1. Choosing Physical Atmospheric Parameters for HD 37776 and its Geometrical Parameters

(a) Physical parameters of the atmosphere. Zboril *et al.* [28] spectroscopically estimated T_{eff} and $\log g$ from the Balmer H β , H γ , and H δ profiles by using Kurucz’s standard models for solar metallicity to be $T_{\text{eff}} = 22\,000$ K and $\log g = 4.5$. They also gave an estimate of the radius, $R^* = 4.3R_{\odot}$. Previously, Shore and Brown [16] obtained $T_{\text{eff}} = 22\,500$ and $R^* = 3.7R_{\odot}$.

The continuum limb darkening for a star with these parameters was assumed, according to Wade and Rucinski [29], to follow a linear law with the coefficient $U_1(\theta) = 0.253$.

We made the currently unavoidable assumption that the model atmosphere was independent of the coordinate on the stellar surface. When the local intensity profiles are integrated over the stellar disk, their change from the center to the limb is taken into account by the factor $U_2(\theta)$, which, for each line, depends on its atomic parameters and on the model atmosphere. To determine the function $U_2(\mu)$, where $\mu = \cos\theta$, we com-

Table 1. Julian dates and phases of the spectra

5875 Å region		4550 Å region	
JD 2400000 +	Phase	JD 2400000 +	Phase
50059.408	0.189	50710.492	0.335
50056.521	0.313	50681.558	0.531
50415.371	0.534	50500.251	0.698
50415.417	0.563	50709.550	0.723
49641.600	0.652	50417.487	0.909
50415.625	0.700		
50060.576	0.915		
50060.546	0.929		
50057.488	0.942		

puted the intensity profiles $r(\mu)$ and equivalent widths $W(\mu)$ for various values of μ . The function $W(\mu)$ was fitted by a quadratic dependence

$$W(\mu) = W(1)[1 - a(1 - \mu) - b(1 - \mu)^2]. \quad (1)$$

Figures 1 and 2 show examples of choosing the parameters a and b for the Si III 4552 and O II 4591 lines. The figures demonstrate that a and b do not depend on local abundance.

The microturbulent velocity cannot be determined spectroscopically (using the curve of growth) from our observational data without including the magnetic effect. However, at such a high T_{eff} of the star, its role in comparison with the thermal velocity for light elements is not so important as that for A stars, while the magnetic effects, including magnetic intensification, are taken into account automatically when computing the local profiles.

In our computations, we assumed the microturbulent velocity to be $V_t = 6$ km s $^{-1}$.

(b) Equatorial velocity V_{equ} and inclination i of the rotation axis to the line of sight.

The rotation period was found by Adelman [17] to be $P = 1.538675$ days. The radius $R^* = 4.3R_{\odot}$ and the period allow the equatorial velocity of the star to be estimated: $V_{\text{equ}} = 142$ km s $^{-1}$.

The projected equatorial velocity $V_{\text{equ}} \sin i$ is usually derived from the measured FWHMs of spectral lines. However, this method yields no reliable result for CP stars with strong magnetic fields, because the line width can be determined by splitting into Zeeman components rather than by rotation. In that case, lines which are weakly sensitive to a magnetic field, i.e., those with small Lande factors, should have been used, but, unfortunately, there were no such lines in the available spectral regions.

A crude, visual semi-intuitive estimate obtained from the line profiles in our spectra is $V_{\text{equ}} \sin i =$

Table 2. List of lines and atomic data used in D–Z mapping

No.	Species	Wavelength, Å (mult)	log <i>g</i> f	<i>E_i</i> , eV	log Γ_r	log Γ_c	Transition	<i>k</i>
1	2	3	4	5	6	7	8	9
1	He I	5875.62(4) 5875.989	0.609	20.87			3P–3D 3P0–3D1	0.111
				0(1000) 50(1000)				
		5875.650					3P1–3D1	0.084
				100(1000) 50(500) 150(500)				
		5875.650					3P1–3D2	0.250
				0(400) 33(600) 83(600) 117(300) 150(100)				
		5875.618					3P2–3D1	0.006
				0(400) 100(600) 50(100) 150(300) 250(600)				
		5875.618					3P2–3D2	0.084
				33(200) 67(800) 83(200) 117(300) 150(300) 183(200)				
		5875.618					3P2–3D3	0.466
				0(257) 17(457) 33(286) 100(429) 117(286) 133(171) 150(86) 167(29)				
2	O II	4591.01(15)	0.447	25.66	9.30	–6.70	2D2.5–2F3.5	
				3(429) 9(357) 14(214) 100(375) 106(268) 111(179) 117(107) 123(54) 129(18)				
3	O II	4596.17(15)	0.290	25.66	9.30	–6.7	2D1.5–2F2.5	
				3(600) 9(400) 77(50) 83(150) 89(300) 94(500)				
4	Al III	4512.54(3)	0.600	17.73	8.03	–5.01	2P0.5–2D1.5	
				7(1000) 73(250) 87(750)				
5	Al III	4529.18(3)	0.289	17.73	8.03	–5.63	2P1.5–2D2.5	
				7(600) 20(400) 100(500) 113(300) 127(150) 140(50)				
6	Si III	4552.65(2)	0.181	18.92	9.08	–6.13	3D1.0–3P2.0	
				0(800) 50(600) 100(600) 150(300) 200(100)				
7	Si III	4567.84(2)	–0.039	18.92	9.08	–6.13	3D1.0–3P1.0	
				50(1000) 150(500) 200(500)				
8	Si III	4574.76(2)	–0.509	18.92	9.08	–6.13	3D1.0–3P0.0	
				0(1000) 200(1000)				
9	Fe III	5833.39(114)	0.63	18.43	8.60	–6.70	7S3.0–7P4.0	
				0(381) 25(357) 50(286) 75(167) 100(333) 125(250) 150(179) 175(119) 200(71) 225(36) 250(12)				

77 km s^{–1}, which gives $i = 32^\circ$. We also allude to the fact that the attempts to numerically simulate the C II 6578 and 6582 profiles by Romanyuk *et al.* [30] yielded a similar estimate ($V_{\text{equ}} \sin i = 80$ km s^{–1}), while the attempts to simulate the C IV and Si IV lines near 1500 Å in the IUE spectra of HD 37776 by Shore and Brown [16] yielded $V_{\text{equ}} \sin i = 90$ km s^{–1} and $i = 47^\circ$. When determining the abundances of light elements for HD 37776, Zboril and North [31] used $V_{\text{equ}} \sin i = 75 \pm 7$ km s^{–1}.

The model of HD 37776 chosen by interpreting the phase curve of effective longitudinal magnetic field B_e obtained with an H β polarimeter (in this case, we assume that the nonuniform distribution of the chemical element whose lines were used to carry out the measurements has no effect) is a combination of centered coaxial dipole, quadrupole, and octupole at $i = 90^\circ$ and

$\beta = 90^\circ$ [15]. This value is in sharp disagreement with the above estimates or requires an implausibly small stellar radius.

Thus, we cannot obtain a prior, sufficiently accurate estimate of i and have to vary this value in the course of our mapping.

3.2. Results of the *I, V* Inversion Procedure

3.2.1. Line profiles. The extent to which the Stokes profiles computed from the derived model coincide with the observed profiles is quantitatively characterized by the rms deviation, as inferred from all points of the *I* and *V* profiles for all phases, i.e., by the residual (σ). The residual must correspond to the errors of the observed profile and is commonly considered as a qual-

ity criterion for the solution of the inverse problem of D-Z mapping in one specific line.

However, a small residual does not guarantee the result against the errors introduced into the solution by inaccurate knowledge of the atomic parameters of the line used, by inaccurate specification of the model atmosphere, or simply by the presence of an extraneous blend in the line. It is therefore necessary to use several lines of one element for its abundance mapping and to estimate the actual accuracy of abundance maps from the scatter of the maps obtained. It should be remembered that, if there are regions with an enhanced elemental abundance on the stellar surface (with an enhanced local intensity of the corresponding spectral lines), then the observed integrated polarization profiles carry information about the magnetic field mainly in these regions and yield the result of extrapolation by means of the spherical functions used to fit the magnetic field outside them. A similar situation arises in the case of large gaps in the phases of observations: extrapolation to large distances may result in errors. Clearly, increasing the number of phases used in the solution makes the map more reliable and detailed. However, our numerical experiments on model problems show that the main features of the surface structure are generally restored correctly even for five or six phases uniformly distributed over the period.

In addition to the above inaccuracies, the accuracy of magnetic maps is affected by errors of the abundance maps. The actual accuracy must therefore be estimated from the scatter of values when averaging all the magnetic maps obtained from different lines of different elements.

Since we cannot independently determine the exact value of i , we performed the solution by varying this angle in the range $23^\circ < i < 90^\circ$ and found the residual to be at a minimum for $32^\circ < i < 50^\circ$; the residual at both limits of this range increases appreciably. Within this range, the magnetic configuration to be determined is virtually independent of i . The results of our solution for $i = 32^\circ, 45^\circ$, and 90° are presented in Table 3 and are considered below.

Columns 3, 6, and 9 give longitudes of the vectors of dipole, quadrupole, and octupole moments; columns 4, 7, and 10 give latitudes of these vectors; and columns 5, 8, and 11 give magnitudes of the vectors with an indication of polarity sign. The quantities L and ϕ are the coordinates of the poles of the corresponding multipoles on the stellar surface; and $D, Q,$ and Oct are the moments (in kG). The strength of the corresponding polar field is $(H_p)_D = 2D, (H_p)_Q = 3Q, (H_p)_{Oct} = 4Oct$.

The derived residuals σ are listed in column 12 of Table 3.

For $i = 45^\circ$ and 90° , the solutions were performed for the following two magnetic configurations:

- (1) dipole + quadrupole (D + Q);
- (2) dipole + quadrupole + octupole (D + Q + Oct).

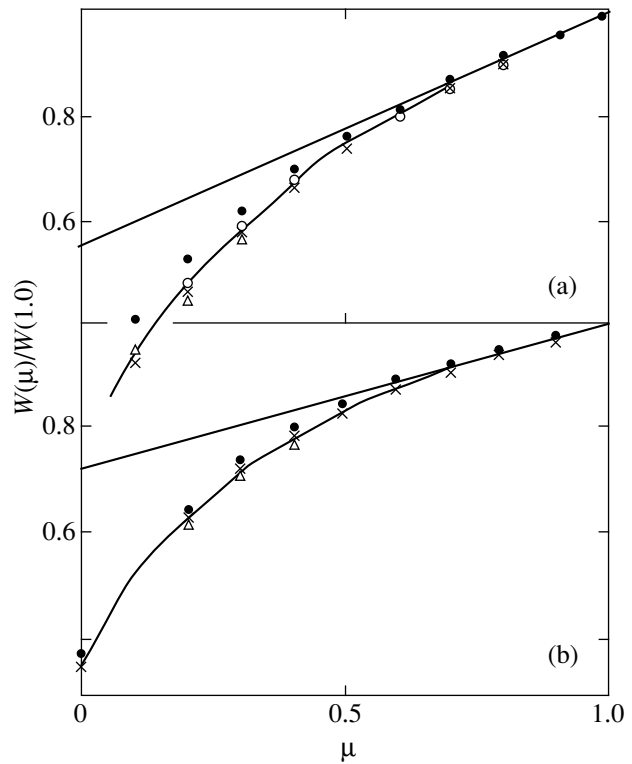


Fig. 1. Computed dependences of line equivalent widths on $\mu = \cos\theta$ for various elemental abundances (AB): (a) the Si III 4552 Å line, the crosses and circles are for AB = 0 and +2, respectively; (b) the O II 4591 Å line, the crosses and circles are for AB = 0 and +3, respectively. The solid lines represent analytic dependences using the quadratic formula (1).

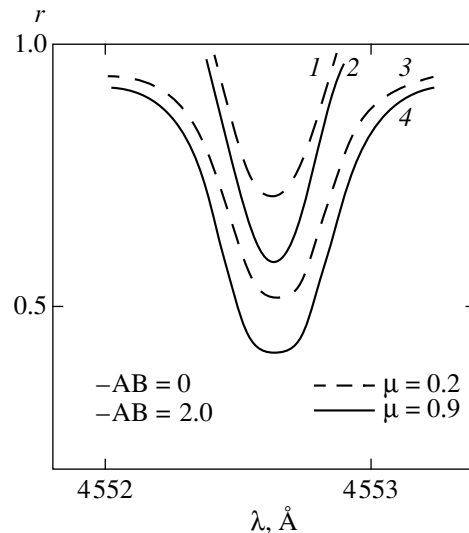


Fig. 2. Computed line profiles for various AB and μ : (1) AB = 0, $\mu = 0.2$; (2) AB = 0, $\mu = 0.8$; (3) AB = +2, $\mu = 0.2$; and (4) AB = +2, $\mu = 0.8$.

For $i = 32^\circ$, we performed the solution for (D + Q) alone. The computations for $i = 90^\circ$ were carried out in an effort to check whether Bohlender's model [15] is suitable for interpreting the observed I and V profiles.

Table 3. Multipole parameters determined in D–Z mapping

Species	λ , Å	L_d°	Φ_d°	D	L_q°	Φ_q°	Q	L_{Oct}°	Φ_{Oct}°	Oct	σ
1	2	3	4	5	6	7	8	9	10	11	12
$i = 32^\circ$, D + Q											
He I	5876	108	25	–14	96	44	30				0.0093
Si III	4552	144	45	–8	125	49	31				0.0043
	4567	132	51	–9	127	49	25				0.0046
	4574	122	42	–9	120	48	33				0.0031
O II	4591	96	30	–28	107	46	46				0.0012
	4596	300	71	–8	123	39	39				0.0024
Al III	4512	88	41	–45	94	51	57				0.0015
Fe III	5833	75	28	–18	83	65	38				0.0023
Mean		109 ± 20	37 ± 8	-17 ± 10	109 ± 14	49 ± 5	38 ± 8				
$i = 45^\circ$, D + Q											
He I	5876	134	2	–5	97	33	13				0.0056
Si III	4552	52	73	–6	135	48	15				0.0043
	4567	75	73	–16	137	60	12				0.0035
	4574	100	26	–22	125	44	29				0.0026
O II	4591	105	23	–43	117	46	55				0.0008
	4596	53	20	–10	138	26	41				0.0021
Al III	4512	80	30	–4	95	48	48				0.0014
Fe III	5833	78	23	–12	81	63	35				0.0020
Mean		85 ± 21	34 ± 20	-19 ± 12	116 ± 18	46 ± 9	31 ± 14				
$i = 45^\circ$, D + Q + Oct											
Si III	4552	240	3	–6	186	36	6	137	50	14	0.0029
	4567	193	82	–11	177	65	5	149	58	11	0.0029
	4574	206	76	–7	274	22	4	136	58	16	0.0019
O II	4591	93	37	–44	116	55	39	147	40	16	0.0007
	4596	53	24	–6	135	20	12	129	45	18	0.0019
Al III	4512	92	18	–26	87	46	45	43	40	9	0.0013
Fe III	5833	95	28	–10	85	67	34	183	20	5	0.0021
$i = 90^\circ$, D + Q											
Si III	4552	200	6	–8	193	36	16				0.0075
	4567	180	60	–6	190	36	12				0.0064
	4574	137	33	–14	154	48	19				0.0028
$i = 90^\circ$, D + Q + Oct											
Si III	4552	220	62	–17	183	60	4	125	72	16	0.0069
	4567	23	30	5	183	47	–6	188	37	14	0.0052
	4574	163	24	–9	45	63	–4	159	60	12	0.0023

Figure 3 shows the observed and computed I and V profiles for the He I 5876 (a), Si III 4552 (c–d), and Fe III 5833 (b) lines, respectively. Note that, in all cases, to ensure the closest coincidence, all the observed profiles must be shifted in wavelength by a value that determines the radial velocity component of the star’s proper motion $V_r = +30 \text{ m s}^{-1}$. A comparison of Figs. 3c and 3d clearly shows that the residual decreases when the octupole component is included in the analysis. Note that the Fe III line is appreciably broader than the lines of other elements because of the large Lande factor (see Table 2).

The coincidence of the observed and computed profiles for all the other lines and configurations can be judged from the residuals in Table 3. Note that minimum residuals are reached for the combination $i = 45^\circ$ and (D + Q + Oct), and that the residuals sharply increase when passing to $i = 90^\circ$.

3.2.2. Magnetic field. An important feature of our computational code is that we do not impose the coaxiality condition on the multipoles of all orders, as was done, for example, by Landstreet [7] and Bohlender [15] when modeling the field.

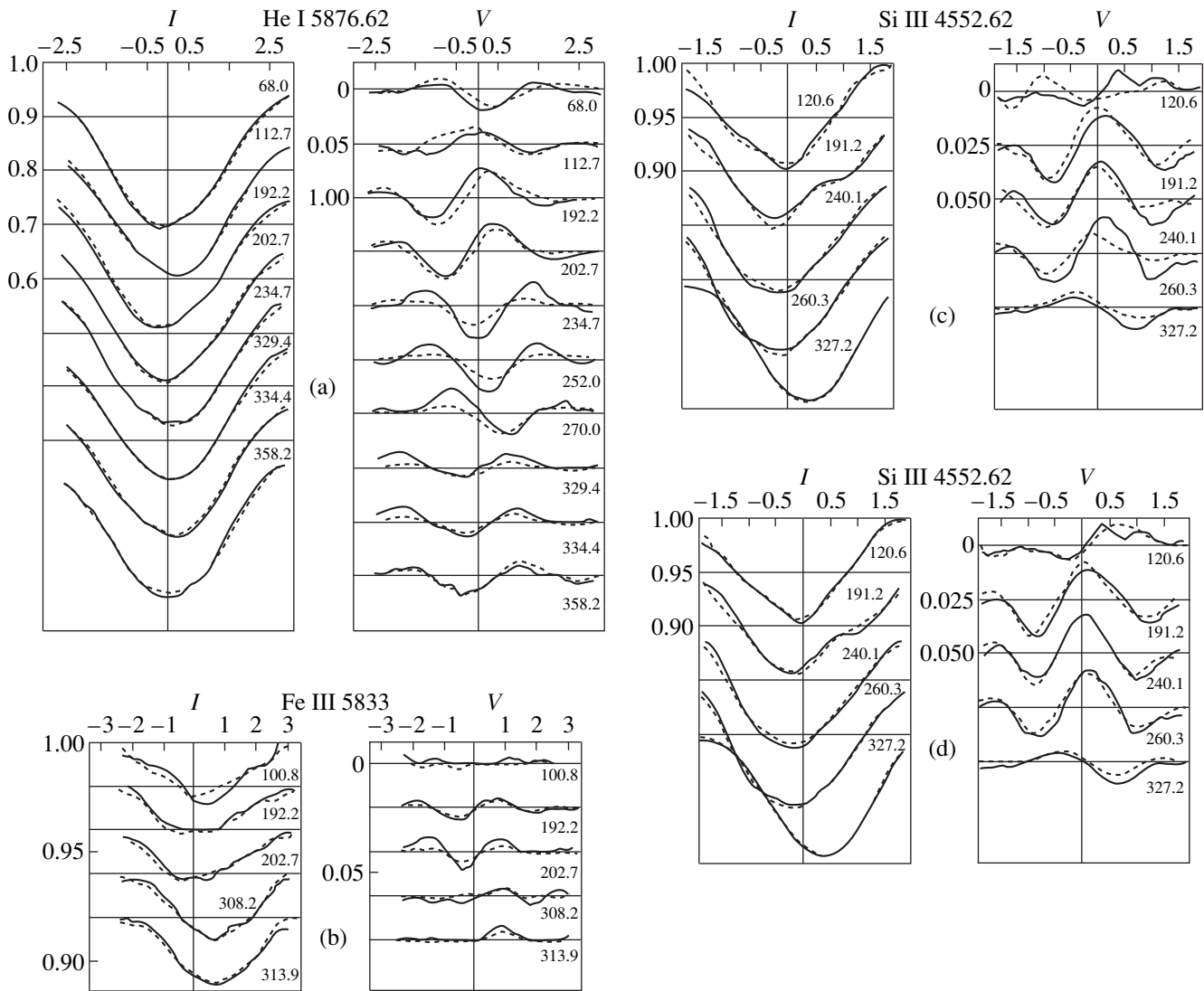


Fig. 3. Observed (solid lines) and computed (dashed lines) Stokes I and V profiles: (a) for He I 5875.62, model (D + Q); (b) for Fe III 5833.65, model (D + Q + Oct); (c) for Si III 4552.62, model (D + Q); and (d) for Si III 4552.62, model (D + Q + Oct).

Bagnulo *et al.* [32] proposed to use a more general expression, which represents an expansion in terms of multipoles of increasing order and arbitrary orientation, to model some of the observed magnetic-field characteristics. Note that, as a rule, it is easy to compute a model (to solve the direct problem) for any number of parameters. At the same time, it is virtually impossible to manually choose a model for an increased number of parameters.

Our computational code allows the magnitude and direction of the vectors of multipole moments to be determined from the observed Stokes profiles when solving the inverse problem. This makes universal the method of analytically describing the model of the star's surface magnetic field using an expansion of the potential in terms of spherical functions, which can in

principle represent any field configuration fairly accurately, and finally determine it from observations.

We used the Si III, O II, Al III, and Fe III profiles to study the magnetic-field geometry HD 37776. The He I line was not used because of the very complex overall Zeeman pattern of this close multiplet; we used the magnetic map obtained from the remaining lines to map the He distribution.

In the solution, we determined the parameters of the magnetic-field model both as a combination of a dipole plus a quadrupole (D + Q) and with the addition of an octupole (D + Q + Oct) of arbitrary orientations placed at the stellar center. The results of our solution are presented in Table 3.

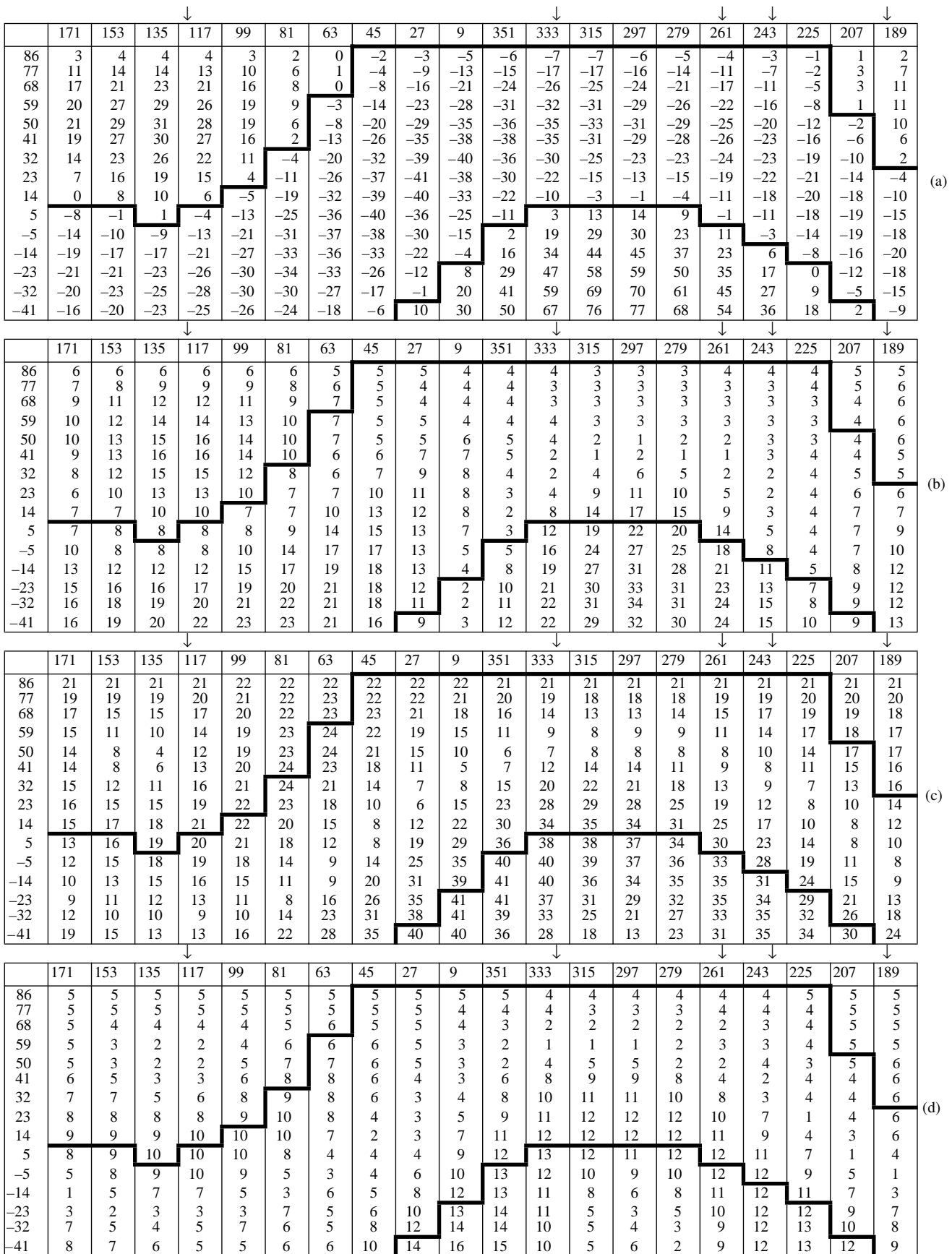


Fig. 4.

Fig. 4. Maps of the normal and tangential components of local magnetic vector averaged over three Si III lines: (a) map of the normal component H_n at $i = 45^\circ$, (D + Q); (b) mean scatter of H_n values when averaging; (c) map of the tangential component H_t at $i = 45^\circ$, (D + Q); (d) mean scatter of H_t values when averaging. The heavy solid lines correspond to zero H_n (the boundaries between the regions of opposite H_n polarity).

Using the derived values of L_d , ϕ_d , D, and L_q , ϕ_q , Q, we can compute the local values of the vector of stellar surface magnetic field (H_s), its normal (H_n) and tangential (H_t) components, as well as the longitudinal (along the line of sight) component H_e . Such magnetic maps can be averaged over several lines or elements and integrated over the visible hemisphere for different phases in order to obtain, for example, the phase curves of effective magnetic field H_e or surface field H_s .

Figures 4a and 4c show the maps of normal (H_n) and tangential (H_t) fields obtained by averaging over three Si III lines, and Figures 4b and 4d show the maps that characterize an arithmetic mean deviation of individual values from the means.

We consider this straightforward way of presenting the results of Doppler-Zeeman mapping to be most useful and informative for the following reasons: the tables may be considered as a map of the entire stellar surface in a rectangular (pseudo-Mercator) projection. They clearly show the grid characterizing the actual resolution of the map. The rectangular projection and the digital representation of the local value of field component (or elemental abundance) in each grid square allow the magnetic configuration and chemical anomalies to be easily compared.

It also allows the results obtained by different authors using different computational codes to be easily compared numerically.

Since the star is arbitrarily assumed to rotate counterclockwise, the phases (the longitudes coinciding with the central meridian at a given time) increase from right to left. The phases of observations are marked by

arrows. The maps show only the part of the star accessible to observation, for which the latitude $\phi > -i$.

The heavy line represents the boundary between regions of opposite polarity, i.e., the line on which $H_n = 0$ and H_t is at a maximum. The scatter of individual values increases in regions with a large positive H_n (at the dipole and quadrupole poles) and near the polarity demarcation line, which appears to be caused by a large gradient and uncertainty in the position of this line on individual maps.

For $i = 45^\circ$, the (D + Q + Oct) field map becomes more complex, and the scatter of the vectors of multipole components increases, although the residual decreases.

Figure 5 shows the $H_n = 0$, lines as constructed from the maps for different elements. As can be seen, the field configuration in all cases is essentially the same. It must represent a kind of an arch corridor above the $H_n = 0$ lines.

Let us now consider our maps of chemical anomalies and their relationship to the magnetic-field geometry.

3.3.3. Maps of chemical anomalies. Figures 6a and 6b show the Si abundance map averaged over three lines and the mean scatter of local abundances, respectively. Three regions of enhanced Si (painted dark), where the abundance is more than 1.8 dex higher than the solar value, are clearly distinguished on the map.

For those grid squares where the local abundance is great (and the local I profiles are strong), the mean scatter of abundances is small, 0.25 dex. Where there is a large Si underabundance, the local profiles are very weak, and the abundance is determined with a large error. For each line, we can estimate the abundance

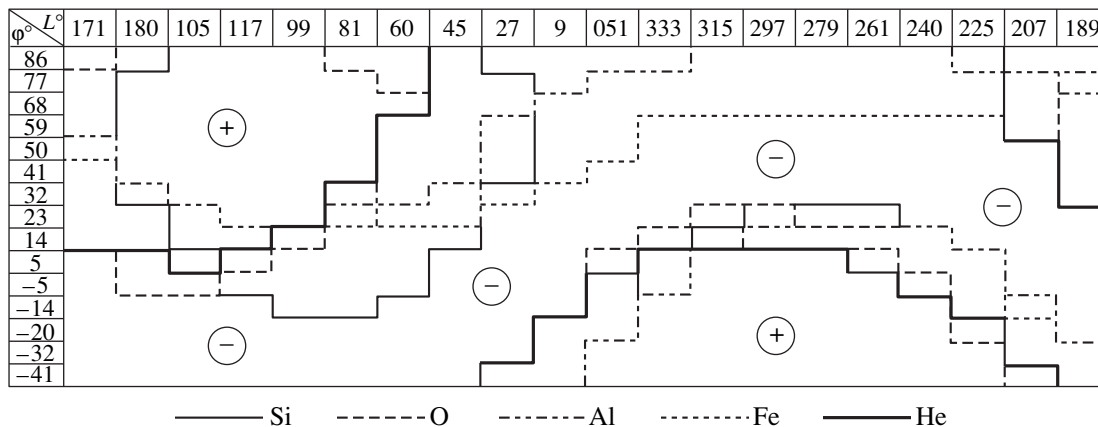


Fig. 5. Boundaries of the regions of opposite polarity ($H_n = 0$ lines) determined from different lines of different elements (averaged maps were used for Si and O).

limit below which the derived underabundance is unreliable.

The second reason for the scatter reaching 1 dex at the boundaries of the high-abundance regions is a shift of the boundaries of these areas on the maps obtained from different lines.

The polarity reversal lines shown on each map allow the chemical anomalies to be immediately compared with the field geometry. The concentration of Si is at a maximum where the magnetic field lines are parallel to the stellar surface.

Figure 6c shows the distribution of oxygen abundance averaged over two lines. Oxygen is underabundant over the entire surface, but the regions of minimum O underabundance coincide with the regions of enhanced Si and lie on the $H_n = 0$ lines. The grid squares on the map where the oxygen underabundance ≤ 3.0 dex are painted dark.

Unfortunately, the number of phases for which we obtained the spectra centered at 4550 \AA is rather small. The number of phases for the longer wavelength region, i.e., for He and Fe mapping, is larger, and we chose the best-quality profiles for ten phases shown in Fig. 3a for He mapping. We also attempted to perform the solution for all the available phases, which yielded a large profile residual, but the magnetic configuration in both cases turned out to be approximately the same.

The numbers in grid squares give the elemental abundances reduced to the solar value. The abundances of all elements prove to be appreciably inhomogeneous over the HD 37776 surface. For Si and He (Figs. 6a and 6d), there are both regions of enhanced and reduced (relative to the solar value) abundances.

O and Fe (Figs. 6c and 6e), as well as Al, are generally underabundant over the entire stellar surface. It should be noted that our estimate of the disk-averaged oxygen abundance obtained (from observed integrated profiles) by the model-atmosphere method and its estimate by Zboril and North [31] are almost an order of magnitude larger than the local abundances on the maps. This is apparently explained by the fact that the magnetic effect (magnetic line strengthening) is properly taken into account during D–Z mapping.

For clarity, the squares with near-maximum abundances are painted dark. For convenience of comparison with the magnetic field, the polarity reversal lines coinciding with a maximum tangential field were plotted on the maps.

An examination of our maps (Fig. 6) shows that the three regions of enhanced (compared to the mean) silicon, oxygen, aluminum, and iron lie along or in the immediate vicinity of the polarity boundaries, i.e., along the lines of maximum tangential field. Interestingly, two regions are located not far from the rotation equator, and one lies virtually at the rotation pole. Helium, which concentrates in two spots near the magnetic poles of opposite sign (Fig. 6d), constitutes an exception.

For clarity, Fig. 7 shows the Si and He maps in spherical projection.

4. DISCUSSION OF RESULTS

Here, we have performed for the first time Doppler–Zeeman mapping of a rapidly rotating, magnetic CP early-type star. We explored the possibility of such mapping for an incomplete set of input observational data. We also studied the potentialities of our modified computational code for I , V , Q , and U inversion, which allowed us to seek a solution for the magnetic field by expanding the field potential in terms of spherical functions. These functions describe the potentials of arbitrarily oriented multipole moments; thus, the field of any configuration can be investigated in principle.

The incompleteness of our observational data is determined, first, by the small number of available phases, second, by the lack of linear-polarization (Q and U) profiles, which is caused by practical (and not fundamental) difficulties of this kind of observations, and, third, by the lack of knowledge of the rotation-axis inclination i . We therefore had to vary i during the solution and to choose its value that yielded consistent results. Note that, for a strong magnetic field, the precise knowledge of i is of greater importance than that for Doppler mapping with no field, because the instantaneous local Stokes profiles depend strongly on i . As the criterion for choosing a solution, we used a minimum residual (Table 3) and a minimum scatter of the coordinates of multipole vectors determined from different lines of different elements (Fig. 8). This allowed us to constrain the inclination, $30^\circ < i < 50^\circ$. Varying i in this range affects the solution only slightly. The inclination i determined in this way is in agreement with the estimates by Shore and Brown [16] and Romanyuk *et al.* [30], but is inconsistent with the geometry of Bohlender’s model [15], which yields $i = 90^\circ$. Bohlender’s model is based on polarization measurements within $\pm 5 \text{ \AA}$ of the H β center. The pos-

Fig. 6. Maps of local abundances ($i = 45^\circ$, $D + Q$). The regions of abundances larger than some value AB_{\max} adopted for each element are shaded: (a) averaged (over three lines) silicon-abundance map with the polarity boundaries from Fig. 4a superimposed, $AB_{\max} = +1.7$; (b) mean scatter of local values computed when averaging, the same regions as in Fig. 6a are shaded; (c) averaged (over two lines) oxygen-abundance map, $AB_{\max} = -3.0$; (d) map of the local helium abundance derived from the He I 5875 line, $AB_{\max} = +1.8$; (e) map of the local iron abundance derived from the Fe III 5833 line, $AB_{\max} = -3.0$.

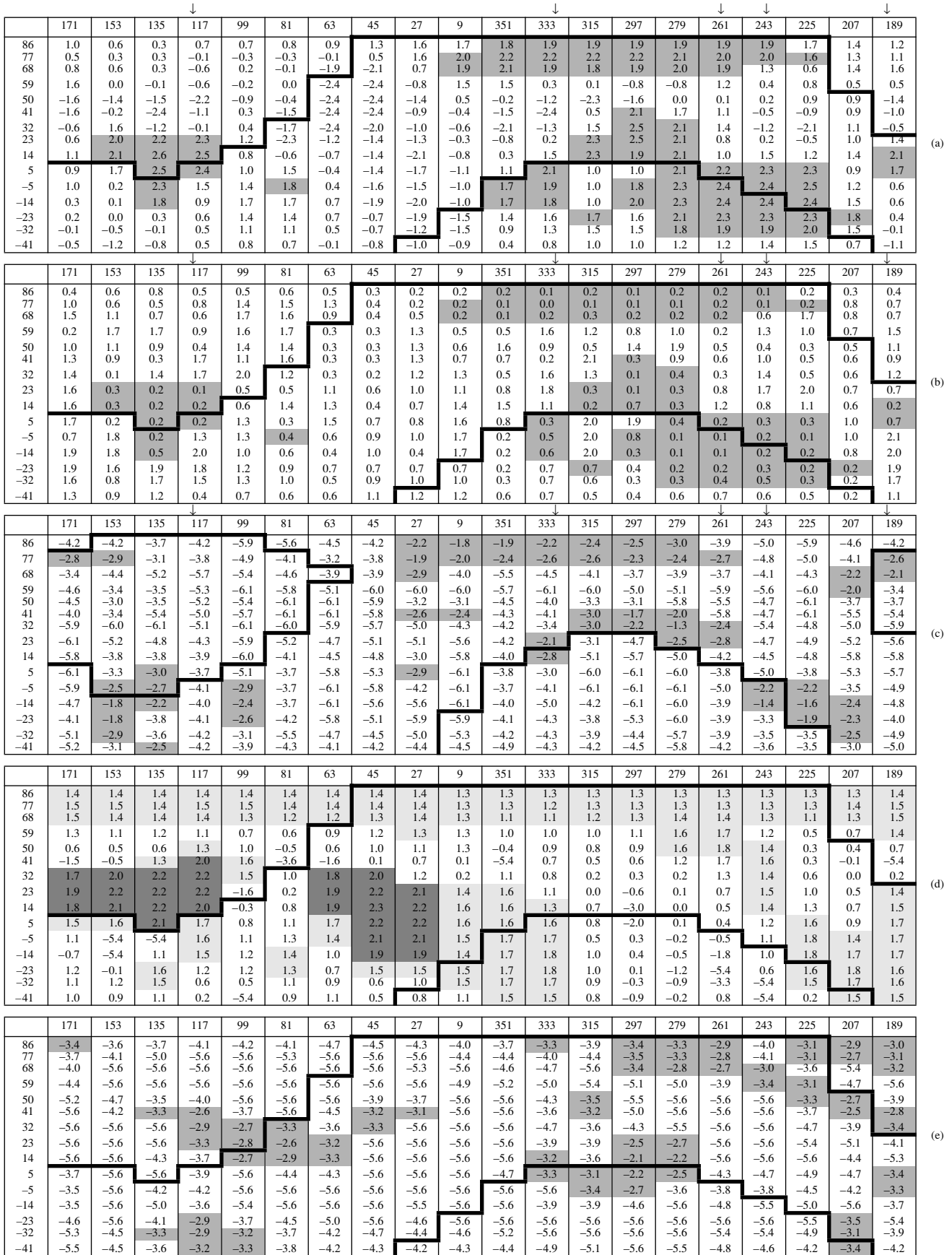


Fig. 6.

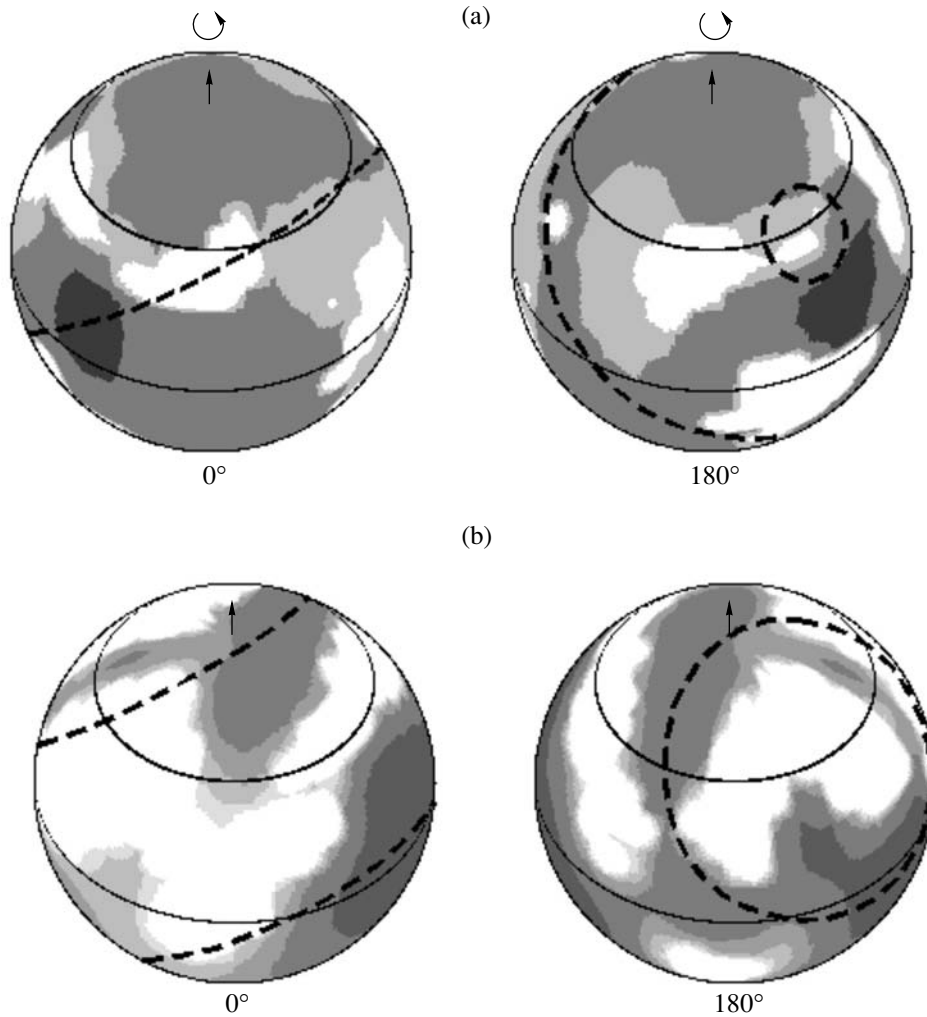


Fig. 7. He and Si abundance maps for HD 37776 in spherical projection at $i = 45^\circ$ for phase 0° and 180° . (a) He distribution; the location of maximum normal field H_n is indicated by dashes. (b) Si distribution; the location of maximum tangential field H_t is indicated by dashes.

sibility that the profiles of the central parts of the hydrogen lines are distorted by interstellar and circumstellar emission cannot be ruled out. Romanyuk *et al.* [30] noted an emission feature in the $H\alpha$ line in HD 37776, while Leone [10] found $H\alpha$ in a similar star (HD 370017) to have a P Cyg profile. The $H\beta$ line may also be distorted. For all our solutions (Table 3), we computed B_e curves, but were unable to obtain a curve similar to that observed by Thompson and Landstreet [6].

If the linear-polarization profiles were available, we could eliminate the uncertainty in i . Ideally, as the model calculations by Piskunov and Khokhlova [33] showed, it would be desirable to have the linear-polarization profiles. However, since the technical difficulties of obtaining them are great, it would be useful to have at least broadband Q and U observations, which were convincingly shown by Leroy *et al.* [11] to be informative. Unfortunately, there are only four B -band measurements of Q and U for HD 37776 in Leroy's cat-

alog [34]. According to the author's comment, the linear polarization is constant and has an interstellar (or circumstellar) origin. However, this may not be the case: three of the four measurements were made at very close phases (0.48, 0.45, and 0.49), while the first measurement (phase 0.87) differs from the three succeeding ones by a value greater than the quoted measurement error. We computed the R_Q and R_U profiles for our models (Fig. 9a) and integrated Q and U (see Fig. 9b) within the line width. As can be seen, these integrated parameters could also be useful in refining the geometry.

An important point of this study is a description of the magnetic potential by using an expansion in terms of spherical functions of multipole moments. In principle, this allows us to study a field of any configuration when solving the inverse problem. Here, we were able to restrict our analysis to the multipole moments of three orders. The criterion for the final choice of a solution was the requirement that the vectors of the

moments determined from different lines of different chemical elements coincide, given the requirement of a minimum residual. When the solutions in Table 3 are considered, it should be borne in mind that, on the average, the accuracy of input information (observed I and V profiles) can hardly exceed $S/N = 200$ because of the errors which are difficult to take into account and estimate (for example, undetected weak blends or errors in the continuum placement). For this reason, the residual in column 12 of Table 3, if it is smaller than 0.005, suggests the possibility of adjusting the parameters of a model that is capable of accurately describing the observed profiles, even if the profiles themselves are not quite accurate, rather than the actual accuracy of the solution. Clearly, introducing a higher order multipole increases this possibility. This can be seen when comparing the solutions for $i = 45^\circ$, (D + Q) and $i = 45^\circ$, (D + Q + Oct). In this case, however, the scatter of the solutions obtained from different lines inevitably increases.

Figure 8 shows the positions of multipole poles on the stellar surface determined from different lines of different elements, according to Table 3. The smallest scatter at a sufficiently small residual was obtained for the field configuration (D + Q) and $i = 32^\circ$ and 45° . When the octupole component is added (D + Q + Oct), the scatter of the vectors of multipole moments increases.

This analysis leads us to conclude that, within the accuracy of our observational data and the data on the star's physical model and its atmosphere, we must restrict ourselves to the solution with the configuration (D + Q) for $30^\circ < i < 50^\circ$. In this case, the moment vectors determined from different lines coincide, and the directions of the vectors of multipoles of different orders also coincide. Thus, we inferred coaxiality of the dipole and the quadrupole from observations and did not confirm the presence of a noticeable, more complex structure.

As we see from Fig. 8, the magnetic axis makes the angle $\beta = 40^\circ$ with the line of sight, which also disagrees with $\beta = 90^\circ$ in Bohlender's model [15].

The absence of a more complex magnetic-field structure and the dominance of a quadrupole component may suggest a nonturbulent mechanism of the field generation in this young star, for example, some global, regular generation process in a protostellar disk. The derived configuration is also consistent with the assumption of a fossil field [35].

A comparison of the maps of chemical anomalies and magnetic field obtained during the solution allows a clear relationship to be established between them. O, Si, and Al are enhanced in the three regions where the magnetic field lines are parallel to the stellar surface, i.e., near the polarity reversal lines ($H_n = 0$). The arch corridors formed by closed field lines lie along these reversal lines. Interestingly, two such enhancement regions lie near the points of intersection of the arch corridors with the rotation equator. Only one element (He)

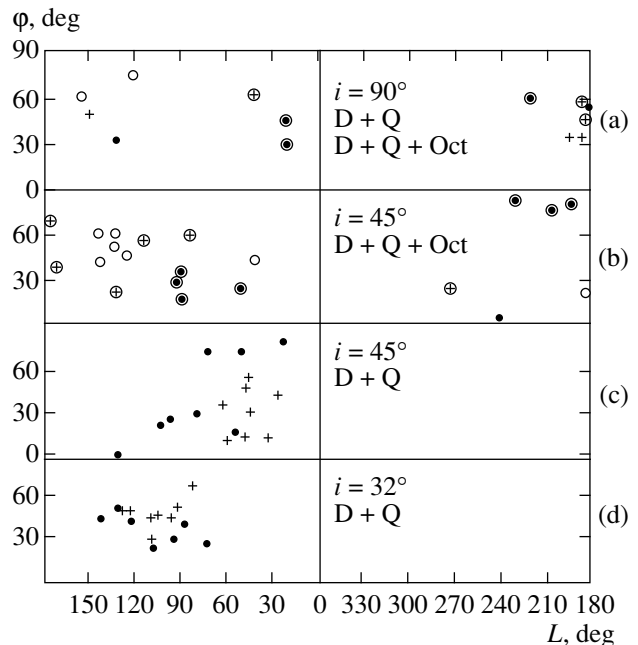


Fig. 8. Coordinates of the vectors of multipole moments obtained from D-Z mapping at various angles i : (a) $i = 90^\circ$; (b) and (c) $i = 45^\circ$; and (d) $i = 32^\circ$. The filled circles are for the dipole moments, the crosses are for the quadrupole moments, and the open circles are for the octupole moments. The circled symbols in Figs. 8a and 8b correspond to the (D + Q + Oct) configuration.

exhibits an enhancement on the stellar surface accessible to observation near the two regions of maximum H_n with opposite polarity. Open field lines appear to emerge from these two regions. The localization of He is consistent with the predictions of Vauclair *et al.* [9]. Other elements supply a direct observational confirmation of the following idea previously proposed by Odell [36] and Leone [10]: the stellar wind freely propagates along open field lines, but accumulates matter near closed field lines, producing a ring on the magnetic equator. Clearly, depending on the interaction of centrifugal force and magnetic pressure, two regions located at the points of intersection of the rotation and magnetic equators can exist instead of a solid belt on the magnetic equator.

This idea was proposed on the basis of an analysis of stars with a predominantly dipole field, and it was corroborated by our D-Z mapping of Babcock's star [27]. Our maps for HD 37776 also confirm the validity of this physical picture for a more complex magnetic configuration. They add a new feature to this picture: there appears to be a third stable region of enhanced elemental abundance in which $H_n = 0$ as well, but it lies at the rotation pole where the centrifugal force is zero.

Our study confirms the futility of attempts to understand the structure of outer layers and the chemical history of CP stars by using the observed magnetic field and elemental abundances averaged over the visible stellar disk. It demonstrates great potentialities of our

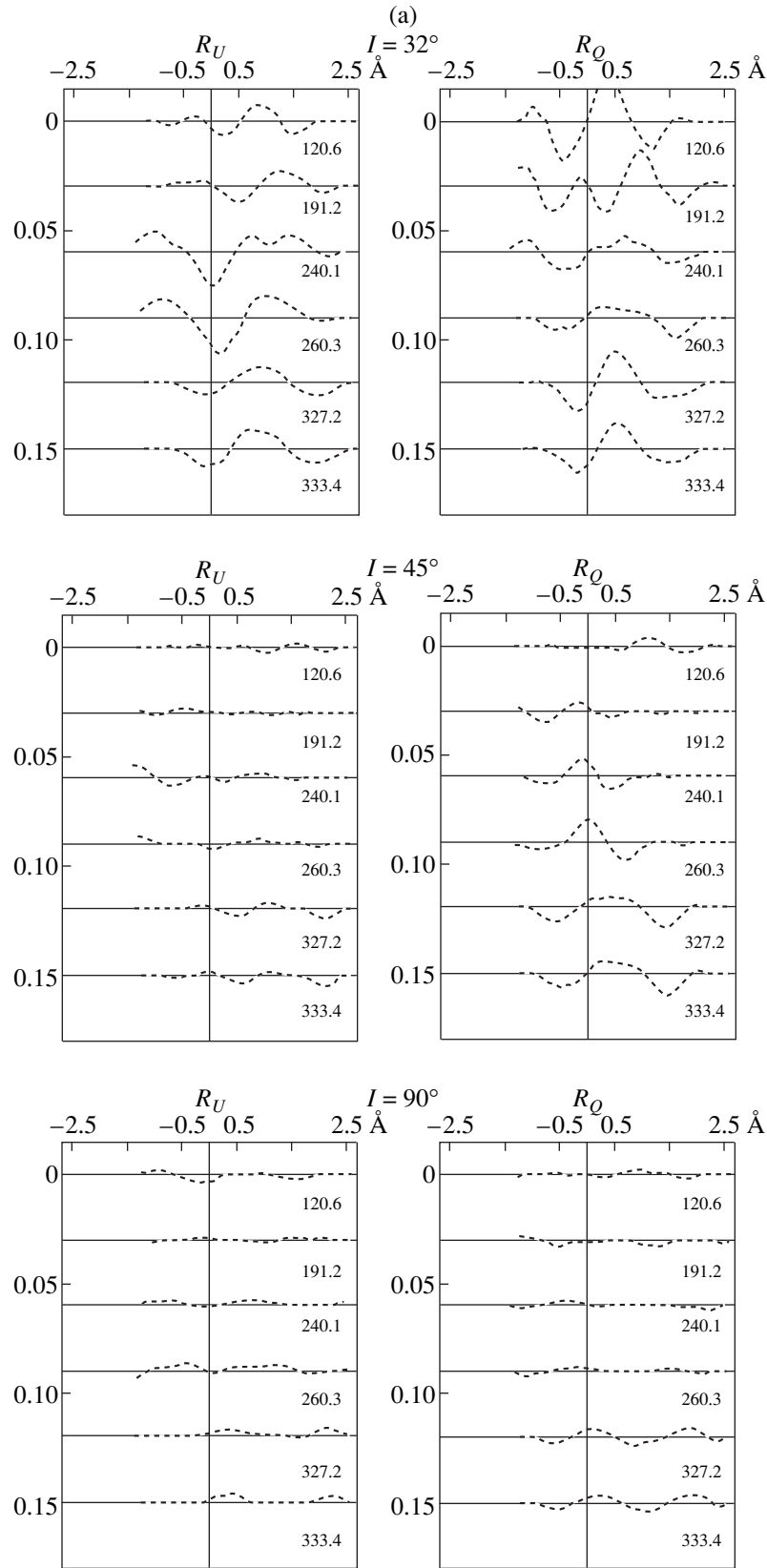


Fig. 9. (a) Computed Stokes R_U and R_Q profiles for the models of the HD 37776 surface at $i = 32^\circ$, 45° , and 90° for the Si III 4567 line; (b) phase dependence of the linear polarization Q and U integrated over λ within the line width ($\pm 1.5 \text{ \AA}$). Curves 1, 2 and 3, 4 indicate this dependence for $i = 45^\circ$ and 90° , respectively.

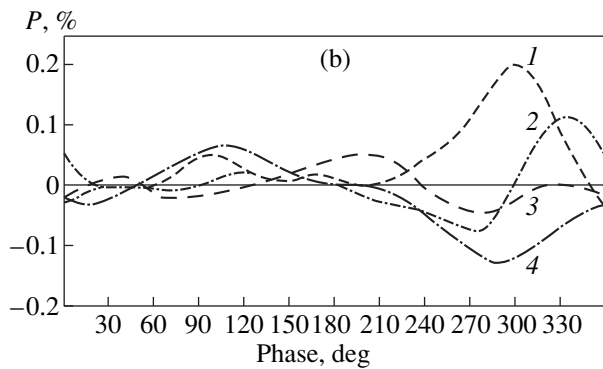


Fig. 9. (Contd.)

method of D-Z mapping. The possibility of a more extensive study of elemental migration in the atmospheres of magnetic CP stars and estimation of the contribution made by these stars to heavy-element enrichment of the interstellar medium opens up, because the stellar wind generated by them has an anomalous chemical composition.

REFERENCES

1. D. V. Vasilchenko, V. V. Stepanov, and V. L. Khokhlova, *Pis'ma Astron. Zh.* **22**, 924 (1996) [*Astron. Lett.* **22**, 827 (1996)].
2. I. I. Romanyuk, V. G. Elkin, D. O. Kudriavtsev, *et al.*, *Bull. Spec. Astrophys. Obs.* **46**, 92 (1999).
3. J. D. Landstreet, *Astrophys. J.* **159**, 1001 (1970).
4. H. Hensberge, W. van Rensbergen, M. Goossens, *et al.*, *Astron. Astrophys.* **75**, 83 (1979).
5. P. Renson, *A Peculiar Newsletter*, Ed. by H. Hensberge and W. van Regimorter (Vrije Univ. Brussel, 1984), No. 8, p. 2.
6. I. B. Thompson and J. D. Landstreet, *Astrophys. J. Lett.* **289**, L9 (1985).
7. J. D. Landstreet, *Astrophys. J. Lett.* **352**, L5 (1990).
8. D. Mihalas, *Astrophys. J.* **184**, 851 (1973).
9. S. Vauclair, N. Dolez, and D. O. Gough, *Astron. Astrophys.* **252**, 618 (1991).
10. F. Leone, *Astron. Astrophys.* **273**, 509 (1993).
11. J. L. Leroy, M. Landolfi, and E. Landi Degl'Innocenti, *Astron. Astrophys.* **311**, 513 (1996).
12. A. P. Hatzes, *Stellar Surface Structure*, Ed. by K. G. Strassmeier and J. L. Linsky (Dordrecht, 1996), p. 305.
13. A. V. Goncharskiĭ, V. V. Stepanov, V. L. Khokhlova, *et al.*, *Pis'ma Astron. Zh.* **3**, 278 (1977) [*Sov. Astron. Lett.* **3**, 147 (1977)].
14. A. V. Goncharskiĭ, V. V. Stepanov, V. L. Khokhlova, and A. G. Yagola, *Astron. Zh.* **59**, 1146 (1982).
15. D. Bohlender, *Pulsation, Rotation and Mass Loss in Early-Type Stars*, IAU Symp. no. 162, Ed. by L. A. Balona, H. F. Henrichs, and J. M. Le Contel (1994), p. 155.
16. S. N. Shore and D. N. Brown, *Astrophys. J.* **365**, 665 (1990).
17. S. J. Adelman, *Astron. Astrophys., Suppl. Ser.* **125**, 65 (1997).
18. G. A. Galazutdinov, Preprint Spets. Astrofiz. Obs., No. 92 (1992).
19. R. L. Kurucz, *CD-ROMs 1-23* (Smithsonian Astrophys. Obs., 1993).
20. V. V. Tsybal, *Odessa Astron. Publ.* **7**, 146 (1994).
21. C. W. Allen, *Astrophysical Quantities* (The Athlone Press, London, 1973), Ch. IV.
22. J. M. Beckers, *A Table of Zeeman Multiplets* (Sacramento Peak Obs., 1969), p. 649.
23. Ch. E. Moore, *A Multiplet Table of Astrophysical Interest, SNRDS-NBS 40* (1972).
24. R. L. Kurucz and T. Peytremann, *A Table of Semiempirical gf-Values, Smithsonian Special Report 362* (1975).
25. W. L. Wiese and G. A. Martin, *NSRDS-NBS 68* (1980).
26. N. E. Piskunov, F. Kupka, T. A. Ryabchikova, *et al.*, *Astron. Astrophys.* **301**, 951 (1995).
27. V. L. Khokhlova, D. V. Vasil'chenko, V. V. Stepanov, *et al.*, *Pis'ma Astron. Zh.* **23**, 532 (1997) [*Astron. Lett.* **23**, 465 (1997)].
28. M. Zboril, P. North, Yu. V. Glagolevskij, *et al.*, *Astron. Astrophys.* **324**, 949 (1997).
29. R. A. Wade and S. M. Rucinski, *Astron. Astrophys., Suppl. Ser.* **60**, 471 (1985).
30. I. I. Romanyuk, V. G. Elkin, G. A. Wade, *et al.*, *Stellar Surface Structure, Poster Proceedings IAU Symp. 176*, Ed. by K. Strassmeier (Vienna, 1995), p. 153.
31. M. Zboril and P. North, *Contrib. Astron. Obs. Skalnaté Pleso* **27**, 371 (1998).
32. S. Bagnulo, M. Landi Degl'Innocenti, and E. Landi Degl'Innocenti, *Astron. Astrophys.* **308**, 115 (1994).
33. N. E. Piskunov and V. L. Khokhlova, *Pis'ma Astron. Zh.* **10**, 187 (1984) [*Sov. Astron. Lett.* **10**, 187 (1984)].
34. J. L. Leroy, *Astron. Astrophys., Suppl. Ser.* **114**, 79 (1995).
35. D. Moss, *Mon. Not. R. Astron. Soc.* **228**, 993 (1987).
36. A. P. Odell, *Proc. IAU Coll. 87*, Ed. by K. Hunger *et al.* (Reidel, Dordrecht, 1986), p. 301.

Translated by V. Astakhov

Mesostructure of the Solar Granulation

H. I. Abdussamatov*

Pulkovo Observatory, Russian Academy of Sciences, Pulkovskoe sh. 65, St. Petersburg, 196140 Russia

Received April 2, 1999

Abstract—Quasi-periodic variations in the thermodynamic and hydrodynamic fine-structure properties of the granulation field along the photospheric surface are estimated quantitatively. The darkest vast intergranular lanes, called the intergranular knots, are the most important indicator of their physical properties. The formulated new definitions of “granule” and “intergranular lane” require a revision of the previous results. The definition of mesogranulation is given, and the method of its detection in the granulation field is described. The following important quantitative results, which established the extent and nature of the physical relationship between the granulation and mesogranulation fields, have been obtained for the first time: (1) the intensity amplitude of granules in mesogranules $(\Delta I(\text{gr})/I_0)_{\text{msgr}} = +10.3\%$ is a factor of 1.4 larger than that of granules in intermesogranular regions $[(\Delta I(\text{gr})/I_0)_{\text{imsgr}} = +7.3\%]$, whereas the intensity amplitude of intergranular lanes in mesogranules $[(\Delta I(\text{igr})/I_0)_{\text{msgr}} = -6.0\%]$ is a factor of 1.4 smaller than that of intergranular lanes in intermesogranular regions $[(\Delta I(\text{igr})/I_0)_{\text{imsgr}} = -8.4\%]$; (2) the mean intensities of photospheric granules and intergranular lanes are $(\Delta I(\text{gr})/I_0)_{\text{phot}} = +9.2\%$ and $(\Delta I(\text{igr})/I_0)_{\text{phot}} = -7.5\%$, respectively; (3) granules cover 59% of the area of mesogranules, 45% of the area of the photosphere, and 31% of the area of intermesogranular regions, while intergranular lanes cover 41, 55, and 69% of these areas, respectively; (4) intergranular knots and bright granules virtually never formed and do not exist in mesogranules and intermesogranular regions, respectively; (5) the amplitudes of intensity fluctuations in mesogranules and intermesogranular regions, as well as the areas occupied by them (49.4 and 50.6%, respectively), essentially level off, $\Delta I(\text{msgr})/I_0 = +3.6\%$ and $\Delta I(\text{imsgr})/I_0 = -3.5\%$, respectively. © 2000 MAIK “Nauka/Interperiodica”.

INTRODUCTION

Quite recently, there has been a consensus that solar granulation and its fine structure represent an independent structure about which we know virtually everything [1–3]. However, recent studies [4–10] have shown that both the structure and nature of the observed granulation are not independent and ambiguous and that it depends on other larger quantized (discrete) photospheric structures associated with the corresponding rising convective plasma flows. However, these relationships, in particular, between the granulation and mesogranulation fields are qualitative. No appreciable quantitative physical relationships have been established between them, nor has it been determined how and to what extent does the mesogranular component distort the inferred granulation parameters. It should be borne in mind that the properties of granulation and mesogranulation are closely related to the formation and concentration of strong magnetic fields on certain areas of the photosphere. The corresponding data are tools of great importance both in understanding the nature and determining the true (“pure”) physical parameters of the granulation and mesogranulation fields. This paper is the first attempt to analyze some of the quantitative parameters of the mesostructure of the solar photospheric granulation.

OBSERVATIONAL DATA

We used high-quality spectrograms with triple dispersion (resolution 0.6 arcsec) obtained at the Pamir high-altitude station of the Pulkovo Astronomical Observatory [11] and the best direct photographs of the photospheric granulation near the solar disk’s center obtained in the stratosphere with a resolution of 0.25 arcsec [12, 13]. A description of reduction technique employed and observational data obtained can be found in our previous papers [5, 7].

RESULTS AND DISCUSSION

We compared the profiles of vertical velocity ($V_{\text{rms}} = 430 \text{ m s}^{-1}$) and continuum intensity fluctuations ($\Delta I_c/I_0 = 4.3\%$) and found a clear correlation between them ($\rho_{\Delta I, V} = -0.6$). In brighter and darker structures of the granulation field, this velocity and its correlation with intensity increase to $V_{\text{rms}} = 530 \text{ m s}^{-1}$ and $\rho_{\Delta I, V} = -0.8$, respectively [5]. What causes such a large increase in vertical velocity and in its correlation with intensity in brighter granules and darker intergranular lanes? The key to solving this question is the presence and determination of the mesogranulation itself in the photospheric granulation field. The correlation between the vertical velocity and intensity of granules is found to increase considerably where hot mesogranules rise. The granules forming here are brighter and larger and have high velocities. They overshoot into higher photo-

* E-mail address for contacts: abduss@gao.spb.su, abduss@gao.spb.ru

spheric layers and have longer lifetimes. At the same time, due to the deceleration of small-scale rising convective cells, the granules in sinking cool intermesogranular regions are weak, small, and have lower vertical velocities and, consequently, not all of them can overshoot into higher photospheric layers. At the same time, intergranular lanes in this region become not only wide, but also fairly extended and darker with high velocities of sinking matter in some places.

Our calculations of the two-dimensional photometric data for the granulation field have yielded for the first time important quantitative results. They show that, on the average, granules ($\Delta I/I_0 > 0$) cover $59 \pm 2\%$, 45% , and 31% of the area of mesogranules, the entire photospheric surface, and intermesogranular regions, while the intergranular lanes ($\Delta I/I_0 < 0$) cover 41 , 55 , and 69% of these areas, respectively. Consequently, (1) the ratio of the fractions of the areas of mesogranules and lanes between them is $S_{\text{msgr}}(\text{gr})/S_{\text{imsgr}}(\text{gr}) \approx 1.9 \pm 0.2$ and (2) the ratio of the fractions of the areas of intermesogranular regions and mesogranules occupied by intergranular lanes is $-S_{\text{imsgr}}(\text{igr})/S_{\text{msgr}}(\text{igr}) \approx 1.7$. We established their even more important property: these ratios sharply increase severalfold with increasing intensity of granules and with decreasing intensity of intergranular lanes (see Fig. 1). Thus, a quantitative analysis of undistorted (stratospheric) photometric data for the photospheric granular field revealed that darker, wide intergranular lanes and brighter granules are virtually not formed and do not exist in mesogranules and intermesogranular regions, respectively. This result is in close agreement with our previous qualitative model for rising mesogranulation convective cells (see Fig. 6 in [5]).

Other important quantitative variations in intensity characteristics of the photospheric granulation field are also noteworthy: the mean amplitude of relative intensity fluctuations in photospheric granules is $(\Delta I(\text{gr})/I_0)_{\text{phot}} = +9.2 \pm 0.2\%$, and the mean intensity amplitude of intergranular lanes is $(\Delta I(\text{igr})/I_0)_{\text{phot}} = -7.5\%$. The mean intensity amplitude of the granules in mesogranules is $(\Delta I(\text{gr})/I_0)_{\text{msgr}} = +10.3\%$, a factor of 1.4 larger than the corresponding amplitude for granules in intermesogranular regions $(\Delta I(\text{gr})/I_0)_{\text{imsgr}} = +7.3\%$; and the mean intensity amplitude of the intergranular lanes in mesogranules $(\Delta I(\text{igr})/I_0)_{\text{msgr}} = -6.0\%$ is smaller by the same factor than the corresponding amplitude of the intergranular lanes in intermesogranular regions $(\Delta I(\text{igr})/I_0)_{\text{imsgr}} = -8.4\%$, i.e.:

$$\frac{(\Delta I_{\text{gr}}/I_0)_{\text{msgr}}}{(\Delta I_{\text{gr}}/I_0)_{\text{imsgr}}} \approx \frac{(\Delta I_{\text{igr}}/I_0)_{\text{imsgr}}}{(\Delta I_{\text{igr}}/I_0)_{\text{msgr}}} \approx 1.4 \pm 0.1.$$

We have thus found experimental evidence for a close physical relationship between the granulation and mesogranulation fields. And this is a factor of the manifestation of deeper mesogranular convective plasma flows in considerable variations of the fine-structure thermodynamic and hydrodynamic properties of the granulation along the photospheric surface. It also

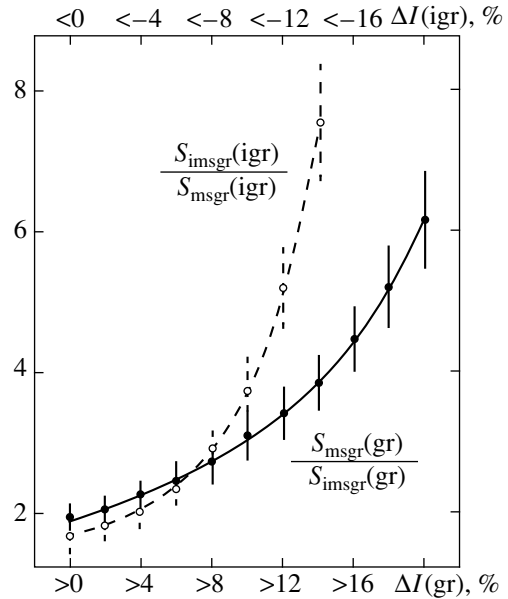


Fig. 1. Ratio of the fractions of areas of mesogranules (S_{msgr}) and intermesogranular regions (S_{imsgr}) occupied by granules versus granule intensity (solid line) and ratio of the areas S_{imsgr} and S_{msgr} occupied by intergranular lanes versus intensity of the latter (dashed line).

determines what the mesogranulation is, and how to detect it in the photospheric granulation field in terms of variations in the physical fine-structure properties of the granulation. In particular, the mesogranular intensity component in the granulation field also manifests itself visually in that virtually all granules (mostly weak and small) located in dark intermesogranular regions are isolated from each other by wide dark intergranular lanes, whereas inside the mesogranules themselves there is a whole family of large bright granules connected by narrow, relatively bright intergranular lanes whose intensity, in some places, exceeds appreciably the mean photospheric intensity ($\Delta I/I_0 > 0$).

The total photospheric areas occupied by granular and intergranular structures abruptly decrease as their relative intensity increases (see the table). As is evident from the table, 33% of the total photospheric area is covered with granular structures with their absolute relative intensity $|\Delta I(\text{gr})/I_0| > 0.1$ and only 10 and 5% of the total area is covered with these structures with their relative intensity exceeding 0.16 and 0.2, respectively. As for the mesogranulation structure, more than 75% and 92% of the photospheric area is covered with mesogranules and intermesogranular regions with $|\Delta I/I_0| < 0.04$ and $|\Delta I/I_0| < 0.06$, respectively. The mean amplitudes of intensity fluctuations in mesogranules and intermesogranular regions, as well as the areas occupied by them (49.4 and 50.6%, respectively) essentially level off:

$$\begin{aligned} \Delta I(\text{msgr})/I_0 &= \Delta I_{\text{gr}(\text{bright})} S_{\text{gr}}/I_0 S_{\text{msgr}} \\ &+ \Delta I_{\text{igr}(\text{dark})} S_{\text{igr}}/I_0 S_{\text{msgr}} \approx 3.6 \pm 0.2\% \end{aligned}$$

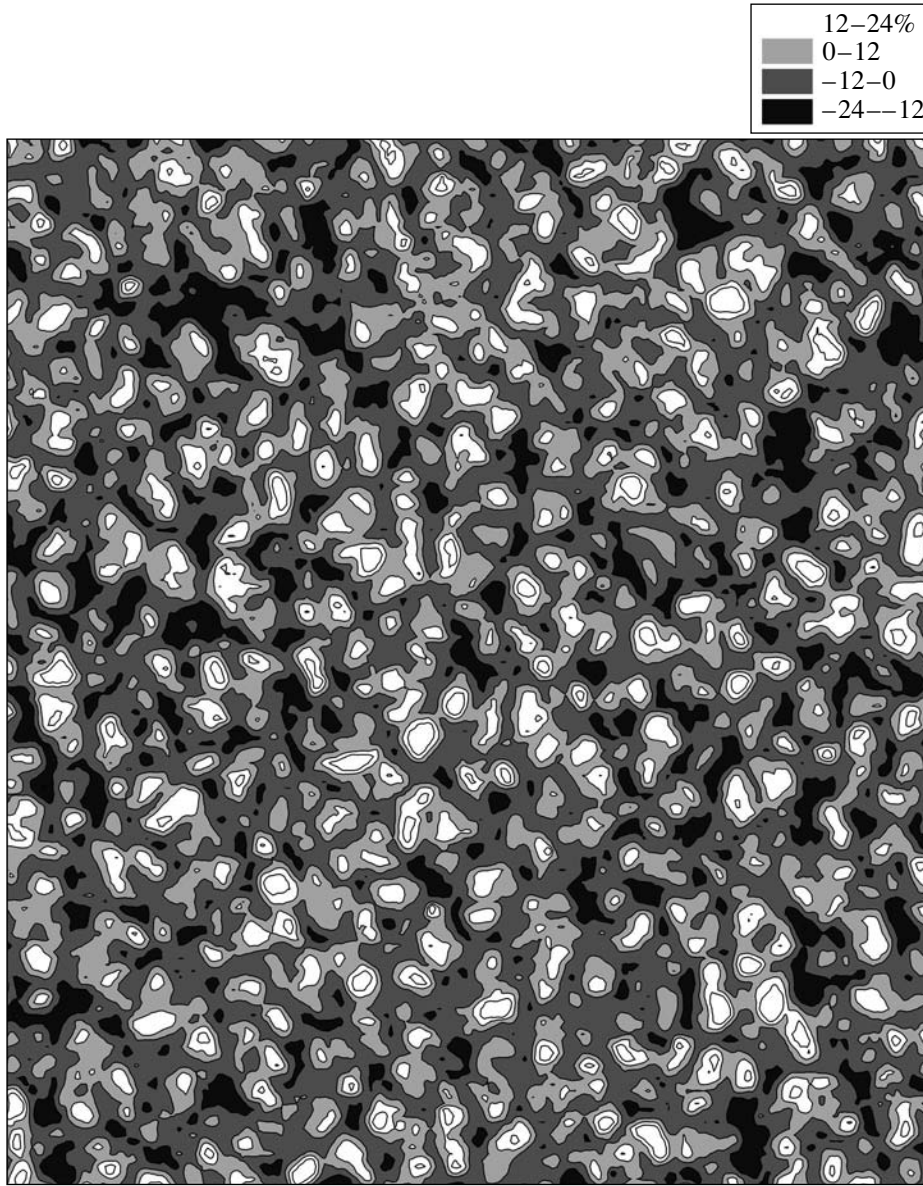


Fig. 2. A photometric map ($\sim 40'' \times 45''$) of $\Delta I/I_0$ intensity isophotes of the granulation field at four intensity levels: above 0 and 12% (bright areas) and below 0 and -12% (dark areas). The darkest extended isolated intergranular lanes are intergranular knots.

and

$$\begin{aligned} \Delta I(\text{imsgr})/I_0 &= \Delta I_{\text{gr}(\text{dark})}S_{\text{gr}}/I_0S_{\text{msgr}} \\ &+ \Delta I_{\text{igr}(\text{dark})}S_{\text{igr}}/I_0S_{\text{msgr}} \approx -3.5\%. \end{aligned}$$

The mean vertical velocities in the mesogranular structures are

$$V_{\text{msgr}} = V_{\text{gr}(\text{bright})}S_{\text{gr}}/S_{\text{msgr}} + V_{\text{igr}(\text{dark})}S_{\text{igr}}/S_{\text{msgr}} < 0$$

and

$$\begin{aligned} V_{\text{imsgr}} &= V_{\text{gr}(\text{bright})}S_{\text{gr}}/S_{\text{imsgr}} \\ &+ V_{\text{igr}(\text{dark})}S_{\text{igr}}/S_{\text{imsgr}} > 0, \end{aligned}$$

and their rms velocity is $V_{\text{rms}} = 130 \text{ m s}^{-1}$ [5].

It should be emphasized here that all narrow, as a rule, weak intergranular lanes disappear virtually everywhere at intensity levels below -10% of the visible granulation field, and only dark, fairly wide and isolated intergranular lanes (Fig. 2), which are called below intergranular knots, remain. An analysis of the available data shows that extended knots of intergranular lanes occupy about half the total area of all intergranular lanes and are the most important indicator of their physical properties determined by mesogranulation structures. These extended knots of intergranular lanes – specific areas of the granulation field – contain most of the cooled granular matter sinking at higher

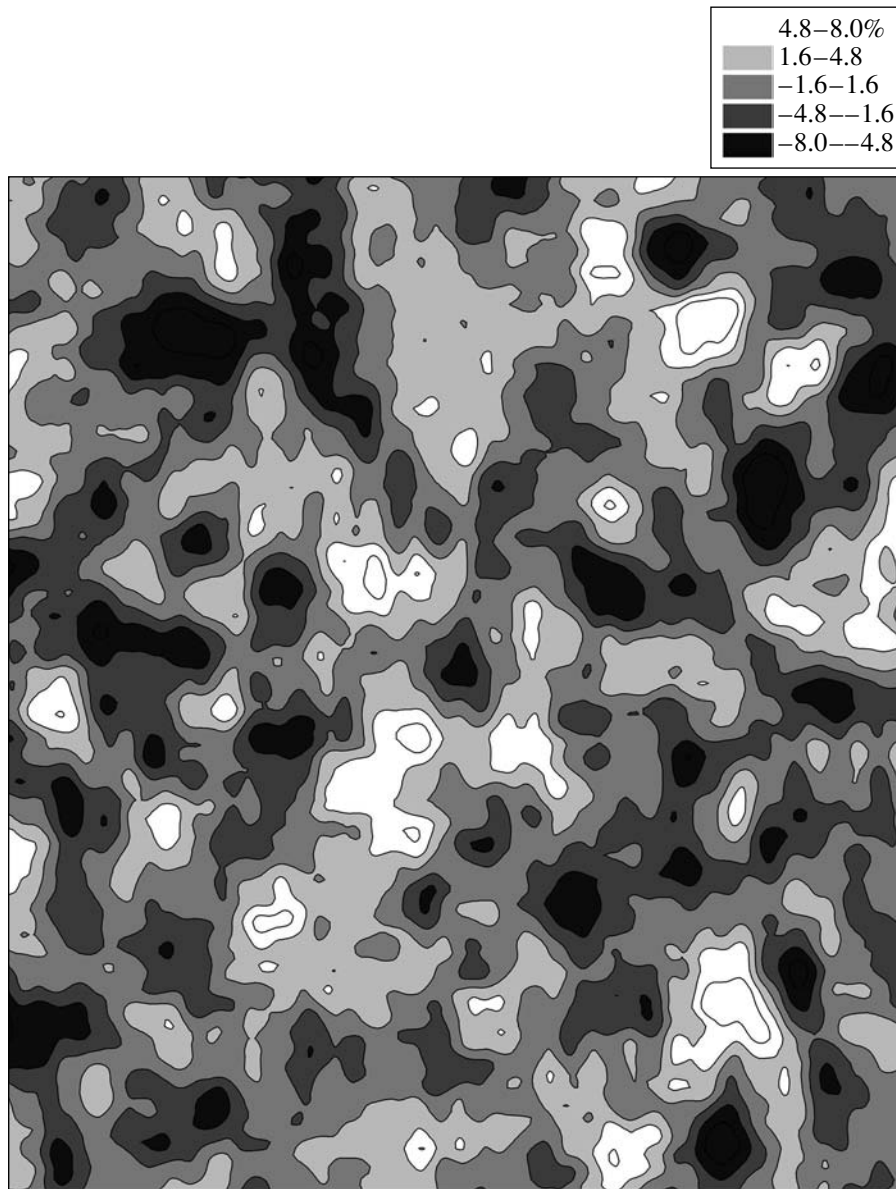


Fig. 3. A photometric map ($\sim 40'' \times 45''$) of $\Delta I/I_0$ intensity isophotes of the mesogranulation field at five intensity levels: from -8 to $+8\%$ at 3.7% intervals where dark areas are intermesogranular lanes.

velocity. At the same time, horizontal mass motion toward mesogranular-cell boundaries dredges finely structured kiloGauss-strong magnetic force tubes up into the intermesogranular lanes, thereby increasing the magnetic flux concentration in the latter. The tubes, which are primary magnetic structural elements of the photosphere, can concentrate in the intermesogranular lanes and merge into a single system of bundles to produce complex magnetic structures of pores and other active structures. It thus follows that intergranular knots as central regions of intermesogranular regions are not just passive responsible for the physical properties of the fine structure of solar granulation (see also [9]). Dark localized intergranular knots are dynamic centers

of this pattern indicating the presence and an appreciable influence of intermesogranular structure.

Photospheric granular and intergranular structures become, on the whole, topologically equivalent at relative intensities $\Delta I/I_0$ above $+10$ and below -10% , respectively. At the above photospheric levels, the granules and intergranular structures (knots) become equally important single-connected isolated formations (see Fig. 2) that occupy approximately equal fractions ($\sim 17\%$) of the photospheric surface. This is due to the fact that granules and intergranular formations observed at the above intensity levels are the central regions (summits) of mesogranules and intermesogranular structures, respectively (Fig. 3). Geometric and

Variation in the fraction of the photospheric area covered with granules and intergranular lanes with relative intensity of these structures

$\Delta I(\text{igr})/I_0$	$S_{\Delta I(\text{igr})}/S_{\text{phot}}$	$S_{\Delta I(\text{igr})}/S_{\text{igr}}$	$\Delta I(\text{gr})/I_0$	$S_{\Delta I(\text{gr})}/S_{\text{phot}}$	$S_{\Delta I(\text{gr})}/S_{\text{gr}}$
<0	0.55	1.00	>0	0.45	1.00
<-0.02	0.48	0.86	>0.02	0.38	0.85
<-0.04	0.40	0.73	>0.04	0.32	0.72
<-0.06	0.32	0.59	>0.06	0.27	0.60
<-0.08	0.24	0.44	>0.08	0.22	0.48
<-0.10	0.16	0.30	>0.10	0.17	0.38
<-0.12	0.10	0.18	>0.12	0.14	0.30
<-0.14	0.055	0.10	>0.14	0.10	0.23
<-0.16	0.026	0.05	>0.16	0.08	0.18
<-0.18	0.011	0.02	>0.18	0.06	0.13
<-0.20	0.004	0.008	>0.20	0.04	0.09
			>0.22	0.03	0.06
			>0.24	0.02	0.04
			>0.26	0.012	0.028
			>0.28	0.008	0.017
			>0.30	0.005	0.010

thermodynamic properties of granular and intergranular structures depend strongly on their horizontal scale and spatial location within the mesogranular structure. This provides further evidence for the major role that mesogranulation plays as the main photospheric structural element [7] in the formation of the observed non-uniform structure of the granulation field. The observed complex nonuniform granulation field is therefore not a simple and primitive formation. It is actually a much more complex photospheric pattern due to the interaction of convective, hydrodynamic, and magnetohydrodynamic forces of various nature and scale in both sub-photospheric convective layers and the photosphere proper.

CONCLUSION

All the observed physical fine-structure parameters of the granulation field are thus appreciably affected by the corresponding mesogranulation component. Consequently, all the previously derived fine-structure parameters of the granulation require a revision, because they refer not to the granulation proper, but to its visible pattern slightly distorted by mesogranulation. Therefore, to study the true physical fine-structure parameters of the granulation proper, we must try to remove the mesogranulation component from the derived parameters of the observed granulation field. With the development of these ideas, the need for refining the definitions of “granule” and “intergranular lane” has arisen, because up until now, all structures brighter than the mean photospheric level ($\Delta I(\text{gr})/I_0 > 0$) and all dark structures ($\Delta I(\text{igr})/I_0 < 0$) have virtually always been classified as granules and intergranular

lanes, respectively. In light of the crucial role of mesogranulation in mesoscale variations of the physical fine-structure properties of the granulation, this formal approach to defining these structures presently does not reflect the true physics of the photospheric layers.

We therefore suggest a new, refined definition of granules and intergranular lanes. Having various shapes, a photospheric granular cell with a typical diameter of 0.2–3'' is a closed (around one or more intensity maxima), isolated (convective) fine-structure element of the undisturbed photosphere with ascending flows of matter. Its intensity $\Delta I_{\text{gr}}/I_0$ exceeds the photometric level $\Delta I/I_0$ of the surrounding space along the entire closed perimeter ($\Delta I_{\text{gr}}/I_0 \geq \Delta I/I_0$). So, the intensity falls below $\Delta I/I_0$ ($\Delta I_{\text{igr}}/I_0 < \Delta I/I_0$) everywhere outside this cell, but this occurs on the open intensity field that is not directly closed at these intergranular ΔI_{igr} levels. Thus, adequately reflecting their name, intergranular lanes represent an extended, continuous photospheric grid with sinking flows of matter and with local intensity minima (intergranular knots) filling the entire space between isolated granular cells.

The photometric intensity $\Delta I/I_0$ is therefore a general local starting level that separates two-dimensional peaks (granules) and dips (intergranular lanes) of the granulation field and the reference level (100%) for their intensity. This starting granulation intensity level ΔI_0 does not always coincide with the mean intensity level of the observed granulation field and fluctuates quasi-periodically about the mean along the photospheric surface mostly in the range -10% to +10%, depending on the spatial localization in the solar mesogranulation structure. Our new, refined definition of granules and intergranular lanes is thus the first attempt to remove the mesogranular component from the observed granulation field and better reflects their physical nature in accordance with the physical processes in the subphotospheric and photospheric layers.

The physical interaction and “superposition” of mesogranular convective plasma flows rising from deeper layers with the families of granular flows that are produced by their breakup at a depth of ~2000 km, give rise to a complex, nonuniform fine structure of the granulation field. In general, giant convective flows rising from the base of the convection zone successively split (break up) as they cross the three particularly unstable convection-zone levels associated with ionizations of helium (twice) and hydrogen. During each splitting of the rising flows at these levels, their secondary flows with the next scale size are additionally formed. The scale sizes of these genetically interrelated convective overshoots penetrating into stable photospheric layers, and, consequently, the corresponding scale sizes of all structural hierarchical photospheric phenomena of giant granules, supergranulation, mesogranulation, and granulation, associated with these four convection regimes, are therefore “nested” in one another. Each succeeding structure is a daughter structure of the

preceding one. Thus, although the formation of the granulation structure is generally determined by the physical processes in the subphotospheric convective layers of hydrogen recombination-ionization, the observed substantial variations of the thermodynamic and hydrodynamic fine-structure properties of the granulation (both in intensity and lifetime and in size and vertical velocity) along the photospheric surface are completely governed by large-scale structures and, first of all and most importantly, by mesogranulation.

ACKNOWLEDGMENTS

This study was supported by the Russian State Science and Technology Program "Astronomy" (project no. 1.5.2.2).

REFERENCES

1. R. J. Bray, R. E. Loughhead, and C. J. Durrant, *The Solar Granulation* (Cambridge Univ., Cambridge, 1984).
2. R. Müller, *Solar and Stellar Granulation*, Ed. by R. J. Rutten and G. Severino (Kluwer Acad., Dordrecht, 1989), p. 101.
3. M. Stix, *The Sun* (Springer, Berlin, 1991).
4. H. I. Abdussamatov, *Solnechnye Dannye*, No. 1, 88 (1991).
5. H. I. Abdussamatov, *Astron. Astrophys.* **272**, 580 (1993).
6. A. M. Title, T. D. Tarbell, K. P. Topka, *et al.*, *Solar and Stellar Granulation*, Ed. by R. J. Rutten and G. Severino (Kluwer Acad., Dordrecht, 1989), p. 225.
7. H. I. Abdussamatov and A. G. Zlatopol'skii, *Pis'ma Astron. Zh.* **23**, 863 (1997) [*Astron. Lett.* **23**, 752 (1997)].
8. J. Hirzberger, M. Vázquez, J. A. Bonet, *et al.*, *Astrophys. J.* **480**, 406 (1997).
9. Th. Roudier, J. M. Malherbe, L. November, *et al.*, *Astron. Astrophys.* **320**, 605 (1997).
10. Th. Roudier, J. M. Malherbe, J. Vigneau, *et al.*, *Astron. Astrophys.* **330**, 1136 (1998).
11. H. I. Abdussamatov, V. S. Korepanov, and I. V. Maklakov, *Solnechnye Dannye*, No. 6, 114 (1989).
12. V. A. Krat, L. Z. Dul'kin, V. N. Karpinskiĭ, *et al.*, *Astron. Tsirk.*, No. 597, 1 (1970).
13. V. A. Krat, V. N. Karpinskiĭ, V. M. Sobolev, *et al.*, *Izv. Glavn. Astron. Obs. Akad. Nauk SSSR*, No. 185, 124 (1970).

Translated by A. Dambis